6-2-2023

EMPIRICAL DISTANCE METRICS RELATIONSHIPS AND UNCERTAINTIES IN SEISMIC HAZARD ASSESSMENT

Melish Kayastha

EMPIRICAL DISTANCE METRICS RELATIONSHIPS AND UNCERTAINTIES IN SEISMIC HAZARD ASSESSMENT

by

Melish Kayastha

A Dissertation

Submitted in Partial Fulfillment of the

Requirements for the Degree of

Doctor of Philosophy

Major: Civil Engineering

The University of Memphis

May 2023

DEDICATION

I would love to dedicate this Ph.D. dissertation to my parents, Mohan Prasad Kayastha and Merina Pradhan, and the rest of my family, who compassionately supported me from overseas throughout my studies abroad.

ACKNOWLEDGEMENT

I am sincerely grateful to my supervisor Dr. Shahram Pezeshk for his invaluable guidance and continuous support during my Ph.D. study at the University of Memphis. His insightful advice and great experience encouraged me in all aspects of my academic life. My gratitude extends to the Department of Civil Engineering for their funding support, the Herff College of engineering for the Herff Fellowship, and the Division of Research and Innovation for the RISE Fellowship.

I would also like to warmly appreciate the committee members Dr. Behrooz Tavakoli, Dr. Charles Camp, Dr. Chris Cramer, and Dr. Roger Meier, who accepted to participate in the committee and for their valuable time and advice.

ABSTRACT

The seismic hazard of an area is determined based on the ground motion observed at that site. The intensity of the ground motion can be predicted using ground motion models (GMMs). GMMs typically use distance metrics such as the Joyner-Boore distance (R_{JB}) and the Rupture distance (R_{RUP}). However, apart from R_{JB} and R_{RUP}, probabilistic seismic hazard analysis (PSHA) also utilizes point-source-based distances like the Epicentral distance (R_{EPI}) and the Hypocentral distance (R_{HYP}). These distance metrics are used for point sources when the fault geometry is unknown or is ignored. We need to determine the relationship between the distance metrics to obtain an accurate seismic hazard of an area. In this study, we develop empirical relationships between R_{JB} and various other distance metrics. This avoids computationally intensive tasks such as computing finite-fault-based distances for different fault geometries of a virtual rupture plane for each point source. The empirical equations provide the relation between R_{JB} and the target distance metric (R_{target}) based on the magnitude of the earthquake and the dip angle of the fault. In addition, we also require the depth to the top of the rupture to calculate R_{HYP}. We discuss the steps to include the variability due to the conversion of the distance metrics in the PSHA. We have compared the results of this study with other published studies for distance conversion. A simple PSHA study of a circular area of 100 km using Pezeshk et al. (2011) and Boore et al. (2014) as the GMMs determined an increase in hazard using the proposed empirical equations and their uncertainties. The equations developed in this study can be directly applied in PSHA and are independent of the GMMs used for seismic hazard calculations. The equations can also be used for different fault geometries with a range of dip angles varying from 10° to 90°, for magnitudes 5.0 to 8.0, and for distances up to 200 km. We have focused on the Central and Eastern US.

TABLE OF CONTENTS

Content Page

List of Tables

Table 5.3 Coefficients for calculation of $\sigma_{[RHYP|RJB,M,\delta,Z_{TOR}]}$ at different dip angles for a given Magnitude (M), depth to the top of the rupture (ZTOR), and Joyner-Boore distance (RJB) (azimuth angle (θ) and hypocenter location are randomized).

List of Figures

equations. The boundary represents the hazard calculated at mean ± 1 sd distance. The dashed line represents the hazard obtained from NSHMP-haz software.

Figure 6.5 Hazard curves at Site 2 (top) and Site 4 (bottom) for Peak Ground Acceleration (PGA) and activity rate of 1 in 500 years for Dip-Slip fault with dip angle 50°. The solid line represents the hazard calculated using the mean distance obtained from the proposed empirical equations. The boundary represents the hazard calculated at mean ± 1 sd distance. The dashed line represents the hazard obtained from NSHMP-haz software.

Figure 6.6 Annual hazard curves for a circular seismic source with a radius of 100 km based on R_{RUP}-based GMM (Pezeshk et al., 2011) (top) and R_{JB}-based GMM (Boore et al., 2014) (bottom) using distance conversion equations developed in this study (KPT23). Annual hazard curves without distance conversion and those based on Thomson and Worden (2018) (TW18) and Scherbaum et al (2004) (SSC04) are also shown for reference.

Abbreviations

ACR	Active Continental Region
AR	Aspect Ratio
BSSA14	Boore et al. (2014)
CEUS	Central and Eastern United States
DM	Damage Measure
DSHA	Deterministic Seismic Hazard Analysis/Assessment
DV	Decision Variable
EDP	Engineering Demand Parameter
EPRI	Earthquake Power Research Institute
GMM	Ground Motion Models
IM	Intensity Measure
KPT23	This study
L	Length (km)
M	Magnitude
NSHMP	National Seismic Hazard Mapping Project
PEER	Pacific Earthquake Engineering Research
PGA	Peak Ground Acceleration (g)
PSHA	Probabilistic Seismic Hazard Analysis/Assessment
PZT11	Pezeshk et al. (2011)
RA	Rupture Area
REPI	Epicentral distance (km)

RHYP	Hypocentral distance (km)
RJB	Joyner-Boore distance (km)
RRUP	Rupture distance (km)
SA	Spectral Acceleration (g)
SCR	Stable Continental Region
SSC04	Scherbaum et al. (2004)
TW18	Thompson and Worden (2018)
USGS	United States Geological Survey
W	Width (km)
Z	Depth (km)
ZTOR	Depth to top of the fault rupture (km)
ϵ	Epsilon
δ	dip angle (degrees)
θ	Azimuth (degrees)

Chapter 1 Introduction

1.1 Background

Seismic hazard analysis is the quantitative analysis of the effects of earthquakes and ground shaking at a site of interest. It is an essential parameter for engineers to design structures that can withstand an earthquake in seismically active regions. The seismic hazard analysis is a complex multi-disciplinary process. It involves geology and seismology, particularly knowledge about the propagation of seismic waves, location of known faults, historical seismicity, and fault-rupture processes. It involves mathematics to understand the probability and statistics. It also involves earthquake engineering to determine the response of the structures and estimate the structural damage.

Pacific Earthquake Engineering Research (PEER) described a formal process to compute the probability distribution for the seismic risk of an area (Cornell and Krawinkler, 2000; Deierlein, 2004). The PEER seismic risk assessment framework provides a quantitative evaluation of the seismic risk of an area by modeling the interaction between several random variables. Mathematically,

$$\lambda_{DV} = \int\int\int G(DV|DM)dG(DM|EDP)dG(EDP|IM)d\lambda_{IM} \tag{1.1}$$

where DV is the decision variable, DM is the damage measure, EDP is the engineering demand parameter, and IM is the intensity measure. λ_{DV} and λ_{IM} are the rate of exceedance of chosen DV and IM, respectively. Due to the one-step Markovian assumption, the variables depend on only one other variable. This assumption simplifies the overall computation. G(DV|DM) provides the probability of exceedance of the decision variable for a given damage measure. There are several

steps taken to determine the seismic risk of an area. The seismic hazard of the area is determined in the first phase. A set of ground motions that can accurately reflect the hazard identified in the first phase are used to estimate the EDP distribution based on a particular IM. In the third phase, fragility functions are employed to determine the probability distribution for a DM at a given EDP value. Finally, the probability of exceedance of DV at a given DM is determined using loss functions. Hence, inaccuracies in calculating seismic hazard would be detrimental to precisely determining the seismic risk of an area.

The seismic hazard analysis can be conducted in two ways: Deterministic seismic hazard analysis (DSHA) and probabilistic seismic hazard analysis (PSHA). In DSHA, the seismic hazard can be described using single-valued discrete events and models. A controlling earthquake is chosen from different earthquake sources based on the earthquake potential of each source. Different models are then used to determine the effect of the earthquake. The effect is usually described by the ground motion experienced at the site of interest, so the models are referred to as ground motion models (GMM). GMMs have been developed for different regions, such as Toro et al. (1997) and Pezeshk et al. (2011) for the central and eastern United States (CEUS). Probabilistic seismic hazard assessment (Cornell, 1968; Kramer, 1996; McGuire, 2004) incorporates the effects of all the earthquakes capable of affecting the site of interest using multi-varied continuous events and models. It provides the probability distribution of the ground motion intensity calculated based on the GMMs. It also incorporates various uncertainties which may be aleatory or epistemic in nature. Aleatory uncertainties are uncertainties due to the earthquake event, such as the location and the time of rupture. Epistemic uncertainties are due to a lack of information or knowledge about the

earthquake process. It can be reduced when more information becomes available about the earthquake event.

In simpler terms, the probability distribution can be described as:

$$P(IM > x) = \sum_{i=1}^{N} \alpha_i \int_{m_{min}}^{m_{max}} \int_{r_{min}}^{r_{max}} P(IM > x|m,r)P(M = m)P(R = r)dmdr \qquad (1.2)$$

where 'IM' is the intensity measure, 'm' is the magnitude of the earthquake, 'r' is the distance from the source to the site, and 'α_i' is the mean rate of occurrence of earthquakes between m_{min} and m_{max}. $P(IM > x|m,r)$ is the probability that an earthquake with a magnitude 'm' and distance 'r' will exceed the ground motion 'z'. $P(M = m)$ and $P(R = r)$ are the probability distributions for magnitude and distance, respectively. It is important to use consistent distance metrics when describing the source-to-site distances in seismic hazard analysis to calculate accurate seismic hazards at the site of interest.

1.2 Motivation

With the growth of population, many populated cities are currently located close to the fault. As a result, there is an increased focus on estimating accurate seismic hazards close to the fault. The current research activities have mainly focused on the rupture directivity effects, which cause a pulse in the velocity time history at close distances (Somerville et al., 1997; Bray and Rodriguez-marek, 2004; Shahi and Baker, 2013; Spudich et al., 2013; Watson-lamprey, 2018; Tarbali et al., 2019). The rupture directivity increases the demand on the structures at close distances and is an important area of study to determine accurate seismic hazards at close distances. However, studying the variation between different distance metrics is also important.

The different distance metrics used to identify the distance from the source to the site of interest converge at large distances. So, accurate seismic hazard calculations can be done without converting from one distance metric to another in such cases. However, the different distance metrics may have significantly different values at close distances, especially at higher magnitudes. As a result, there may be significant variation in the calculated seismic hazard without using appropriate distance metrics. So, the seismic hazard may be limited to specific distance metrics, which would significantly hamper the use case for PSHA. Hence, converting from one distance metric to another may be necessary to accurately determine an area's seismic hazard in conducting PSHA.

1.3 Objectives

This research aims to address the issues discussed in section 1.2 as far as possible. The following objectives are sought in this research:

- Develop a dataset of different distance metrics representing their corresponding values for each other for different earthquake events and fault geometries to build a complete database to convert from one distance to another.
- Propose empirical equations that can accurately represent the dataset without significant variations. Also, the parameters used to convert the distance metrics should be in use in current methodologies to determine the seismic hazard.
- Formulate methods to capture the uncertainty due to the conversion from one distance metric to another. The uncertainty is vital to determine the accurate seismic hazard in PSHA.
- Provide quantitative estimation of the variation in the seismic hazard due to distance

conversion.

1.4 Organization of this Dissertation

The dissertation is comprised of seven chapters. Chapter 1 provided a background and discussed the motivation and the objectives of this study. Chapter 2 is the literature review and provides detailed background on the different methodologies to handle the use of different distance metrics in seismic hazard calculations. Chapter 3 explores the parameters required to accurately describe the earthquake events and the rupture faults. It also provides methods to determine the values for different distance metrics based on these parameters. Chapter 4 utilizes the dataset developed in Chapter 3 to develop empirical equations to convert between different distance metrics. Chapter 5 provides the empirical equations to include the variability due to distance conversion in seismic hazard calculations. Chapter 6 presents the application of the equations proposed in Chapter 4 and Chapter 5. Finally, Chapter 7 concludes the results of this study and provides some recommendations for future research. The dissertation expands on the work published in Kayastha et al. (2023b).

Chapter 2 Literature Review

2.1 Introduction

Researchers use different distance metrics to determine the source-to-site distance metrics during an earthquake. The most used distance metrics are the Joyner-Boore distance (R_{JB}), the Rupture distance (R_{RUP}), the Epicentral distance (R_{EPI}), and the Hypocentral distance (R_{HYP}). R_{JB} measures the closest distance to the surface projection of the fault, R_{RUP} measures the closest distance to the ruptured fault, R_{EPI} measures the distance to the epicenter of an earthquake, and R_{HYP} measures the distance to the hypocenter of an earthquake. R_{JB} and R_{RUP} are classified as fault-based distances, while R_{EPI} and R_{HYP} are classified as point-based distances. Many researchers have used point-based distance metrics to develop their GMMs. However, issues with large magnitudes at close distances for such models resulted in unreliable seismic hazard calculations. Hence, GMMs usually use either R_{JB} or R_{RUP} to determine the ground motions in an area. However, the seismicity of some areas cannot be associated with known faults. In such cases, PSHA uses point source models to describe the seismic hazard, as such models can be used for gridded seismicity (Tavakoli et al., 2018).

In PSHA, different GMMs with different distance metrics may be included in different branches of a logic tree. Certain assumptions can be made to estimate the value of the required distance metric in such cases. However, such assumptions and the corresponding distance conversions may increase the uncertainties. Moreover, uncertainties in distance conversions may cause the uncertainties of the GMM to be magnitude and distance-dependent, even if the uncertainties of the GMMs did not have those dependencies in the original equations. Monelli et al. (2014) found differences of as much as 54% in a PSHA sensitivity study when using point-based and fault-based

distances. This resulted in a considerable underestimation of the hazard, especially for large earthquakes. Tavakoli et al. (2018) also demonstrated that effective R_{EPI} developed higher seismic hazards than R_{JB}. Thompson and Worden (2018) also showed significant variation between mean rupture distance and point-source distances, even for small-magnitude earthquake events. There are a few methods to avoid this problem which we have discussed in the next section.

2.2 Approaches to use different distance metrics in seismic hazard analysis

2.2.1 Approach 1: Conversion between distance metrics

One approach to utilize multiple source-to-site distances would be to convert from one distance metric to another. Scherbaum et al. (2004) used R_{JB} as the primary distance metric to obtain R_{EPI}, R_{HYP}, R_{RUP}, and the distance to the seismogenic part of the rupture plane. They simulated various earthquake events based on the magnitude, dip angle, and location of the hypocenter on the fault. They used Wells and Coppersmith (1994) as the magnitude-scaling relationship to determine the length and the width of the fault. For the depth distribution, they developed a truncated normal distribution model with different mean and standard deviation values based on the style of the faulting. They also ignored events deeper than 20 km for strike-slip faults and 25 km for dip-slip faults. The simulation was conducted for different cases: strike-slip, dip-slip, and a general case where the style of faulting is unknown. Different dip angle ranges were assumed for different cases. The dip angles were varied from 40° to 90° for the general case, 40° to 70° for shallow dipping faults, and 80° to 90° for strike-slip faults. A residual function based on the gamma distribution was used to describe other distance metrics based on magnitude and R_{JB}. The residual function, the difference between the target distance metric and reference distance metric (R_{JB}), is always positive as the R_{JB} is always less than or equal to other target distance metrics. The

polynomial functions are applicable for shallow intercontinental earthquake events for R_{JB} from 0 to 100 km and moment magnitudes between 5.0 and 7.5. They also provided coefficients to calculate the standard deviation, which can be used to account for the variability of the GMM due to distance conversion. Though the variability of the GMMs may not be magnitude or distance dependent in their original form, the equations provided in Scherbaum et al. (2004) provide a method to account for this variability reliably for all GMMs. They also compared these relationships with manually derived distance metric estimates for Landers, Imperial Valley, and Chi-Chi earthquakes.

EPRI (2004) developed four GMMs for the central and eastern United States, three GMMs based on R_{JB}, and one GMM based on R_{RUP}. They also provided a method to convert from R_{EPI} to R_{JB} and R_{RUP} for each of their GMMs. The ruptured area was modeled based on the Somerville et al. (2001) relation to obtain the distance conversion equations. The hypocenter depth distribution was modeled using Silva et al. (2002). A length-to-width aspect ratio of 3 for the strike-slip fault and 2 for the dip-slip fault were used. A dip angle of 40° was assumed for the dip-slip fault. EPRI (2004) also constrained the maximum depth to 25 km. R_{EPI} was chosen as the primary distance metric to obtain R_{JB} and R_{RUP}. They provided separate coefficients for centered ruptures and random ruptures. They determined that random ruptures estimated slightly smaller distance correction compared to centered ruptures. EPRI (2004) also provided equations to calculate the additional aleatory variability to determine the total variability in PSHA for each GMM. They can be directly used in PSHA for the respective GMMs. However, they cannot be used for other GMMs not included in EPRI (2004).

2.2.2 Approach 2: Development of GMMs for different distance metrics

As another approach, Bommer and Akkar (2012) suggested that two different sets of coefficients for point-source-based models and finite-source-based models should be developed for GMMs. However, few researchers have provided coefficients for point-source and finite-source-based distances for their GMMs. Akkar et al. (2014) provided the coefficients for both point-based and fault-based distances for their GMM for Europe and the Middle East. They determined low variation in the sigma models for GMM based on R_{EPI} and R_{JB}. However, that may have resulted from an incomplete dataset, with a sparseness of data for large earthquake events at small distances. So, they proposed a method to determine the true sigma of the R_{EPI} model based on the R_{JB} model for a dense grid of observation points. They used Scherbaum et al. (2004) to calculate the values.

Bommer et al. (2016) simulated many R_{EPI} and R_{JB} combinations based on a range of fault orientations and fault dimensions to determine the variability in their ground motion model for induced seismicity. They used Wells and Coppersmith (1994) to determine the rupture length, as no appropriate magnitude scaling relationship was available for induced seismicity. As a result, the dimensions may not be applicable for induced earthquakes at shallow depths. The same process could be repeated for other magnitude scaling relationships to obtain accurate sigma values for those regions. They assumed a single observation site and simulated the epicentral location for many points in a circular seismic zone. This provides a large dataset of epicenter locations for different fault rupture dimensions and geometry for different magnitude earthquake events. They calculated a range of R_{JB} values for a given R_{EPI} and then used Akkar et al. (2014) to determine the median values for spectral acceleration. Finally, they calculated the variability due to R_{EPI} and

its respective R_{JB} values. They modeled sigma as a Gaussian distribution. This approach can be directly applied without converting the distances by including the sigma in the total GMM variability for PSHA calculations. However, the equation for variability cannot be used for other GMMs.

2.2.3 Approach 3: Simulation for different distance metrics

The third approach would be to simulate pseudo-ruptures for each scenario based on dimensions obtained using different magnitude scaling relationships such as Wells and Coppersmith (1994), Somerville (2014), or others. Kaklamanos et al. (2011) developed the relationship between R_{JB} and R_{RUP} based on the geometrical properties of the fault. For a given dip angle (δ), down-dip rupture width (W), depth to the top of rupture (Z_{TOR}) and $R_{JB,}$ they provided the relation to determine the R_{RUP} for different source-to-size azimuths (α). They have also suggested different relationships for δ, W, and Z_{TOR} if these values are unknown. They compared their results to those obtained by Scherbaum et al. (2004) and found them to be slightly different.

Thompson and Worden (2018) derived mean R_{JB} and R_{RUP} constrained on R_{EPI}, magnitude, and azimuth. They also provided adjustment factors for GMM standard deviations to include the uncertainty due to the conversion of different distances. For simulation, they used different distance conversion equations provided in Somerville (2014) for the stable continental region (SCR), Hanks and Bakun (2008) for the active continental region (ACR), and Wells and Coppersmith (1994) for both cases. A length-to-width aspect ratio of 1 for SCR and 1.7 for ACR was assumed. They have assumed different ranges for the dip angle based on the style of faulting and the magnitude scaling relationship used. The seismological depth is assumed to be 20 km for ACR and 15 km for SCR. At a given R_{EPI} and magnitude, they determined the target distance

metrics (R_{JB} or R_{RUP}) by integrating at different azimuths, dimensions of the fault (length and width), dip angles, and epsilons. Epsilon (ϵ) is the standard normal random variable used to incorporate the variability in the estimation of the fault dimensions determined based on the magnitude scaling relationship used. They observed the mean R_{JB} decreased as the dip angle decreased due to increase in the width projection. The ratio of the mean R_{JB} to R_{EPI} varied from 0 at small distances to 1 at larger distances while the ratio of the mean R_{RUP} to R_{EPI} is greater than 1 at smaller distances and approaches 1 at very large distances. The variation of R_{RUP} at small R_{EPI} is controlled by the distribution of depth to top of rupture (Z_{TOR}). At shorter distances, the variance for R_{JB} is smaller for large magnitude earthquake events while the variance is greater at shorter distances for smaller magnitudes for R_{RUP}. They also determined that the choice of aspect ratio did not significantly impact the estimation of distances.

Tavakoli et al. (2018) proposed an analytical distance conversion method to convert R_{JB} to R_{EPI}, $R_{HYP,}$ or R_{RUP} based on the geometry of the fault and the distribution of the hypocenter. The distance obtained can be combined with other seismological constraints, such as geometric spreading and attenuation parameters, to obtain effective distances which can demonstrate the effect of extended fault sources at small distances. They also provide separate equations to estimate the distances for strike-slip and dip-slip faults. Similar to Thompson and Worden (2018), they integrate the values along the fault dimensions (length and width), azimuths, and depth of the fault to determine the target distance (R_{EPI} and R_{HYP}) for a given R_{JB}, magnitude, and dip angle of the fault. Based on these distances, they calculate the effective distance that can reasonably simulate the average ground motions for large earthquakes. Effective distances are based on equivalent point source modeling. In equivalent point source modeling, the rupture originated from a virtual

point at an effective distance from the site such that there is no saturation effect at close distances. They calculate the effective distances to account for the geometrical spreading and attenuation using the Boore (2009) approach such that the effective point can generate a similar energy intensity level to those generated from all the sub-faults at the observation site. The method developed by them can be employed for different magnitudes, distances, and site-specific conditions to obtain an accurate conversion between different distance metrics for the specific region. A method to account for the uncertainty has also been discussed. This approach reduces the uncertainty considerably compared to other distance conversion methods, as the uncertainty at a particular azimuth is zero. As the method is generic, it can be applied to different cases of earthquake rupture, large, small, or even induced earthquakes. The resultant distance conversion is insensitive to frequency, so the same values can be applied to the GMM for different frequency values.

2.2.4 Current approach

In current PSHA methodologies for the United States Geological Survey (USGS), Petersen et al. (2010) assume the seismic energy is released from the epicenter rather than the crust of the ruptured fault. They use R_{EPI} as the reference distance to calculate R_{JB} for a vertical strike-slip fault for different azimuths ranging from 0° to 360°. They assume the epicenter is at the center of the fault, and they used Wells and Coppersmith (1994) for the magnitude scaling relationship. They use a virtual fault model, where the vertical faults are simulated at random orientations, and the site is fixed about the center of the fault. However, for a fixed epicentral distance, the station can be relocated for a given azimuth based on the location of the epicenter, as shown in Figure 2.1. To avoid this, the location of the epicenter is always assumed to be at the center of the fault. However,

many researchers, such as Mai et al. (2005), have shown that the location of the epicenter may have a distribution along the fault. Also, EPRI (2004) demonstrated that the centered epicenter approach provided slightly higher distance adjustments than a random epicenter distribution. So, the USGS method may not represent the actual distance adjustment required, particularly for dip-slip faults.

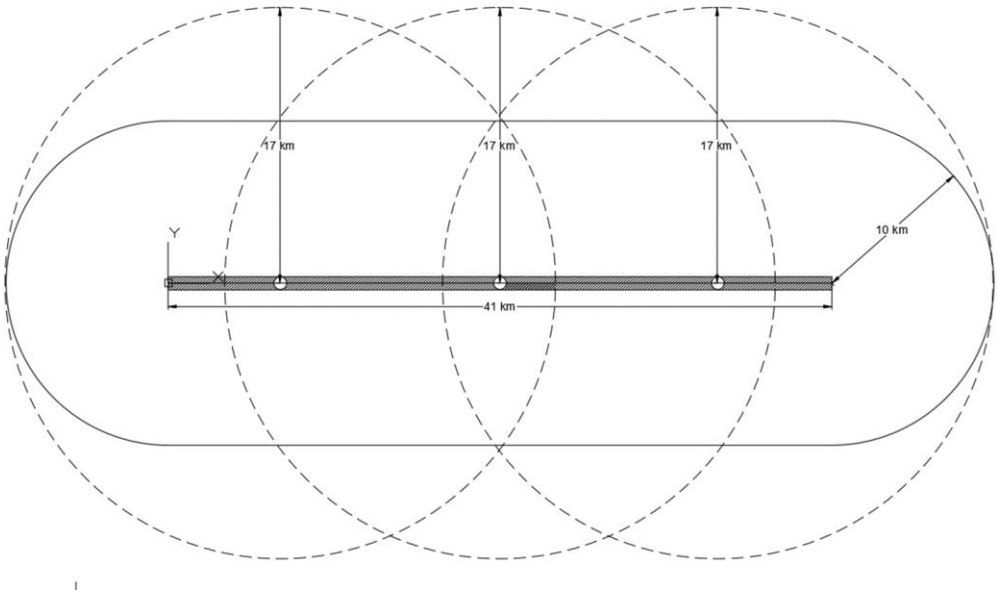

Figure 2.1 Demonstration of the variation of the location of the observation sites for a fixed R_{EPI} based on the location of the epicenter. The observation sites have a fixed position for a fixed R_{JB} and azimuth.

2.3 Research gaps

- The distance conversion equations developed by EPRI (2004) depend on the GMMs and frequency.
- Scherbaum et al. (2004) do not consider the effect of hanging walls and footwalls.
- Kaklamanos et al. (2011) do not include a conversion method between point-source distance metrics and extended fault distance metrics.

- Calculating seismic hazards is a computationally intensive process. The method developed by Thompson and Worden (2018) and Tavakoli et al. (2018), which involves integration at different possible virtual faults or virtual sites, may not be practical for large datasets.
- The current USGS approach is only practical for vertical strike-slip faults and may not be suitable for dip-slip faults.

Chapter 3 Estimation of Distance metrics

3.1 Introduction

Based on the seismic source and the GMMs used, researchers can use different distance metrics to calculate the distance from the earthquake event to an area of interest. The most used distance metrics are Joyner-Boore distance (R_{JB}), Rupture distance (R_{RUP}), Epicentral distance (R_{EPI}), and Hypocentral distance (R_{HYP}). Apart from these distances, some researchers also use R_X and R_Y. R_X is the closest perpendicular distance from the site to the projection of the top edge of the ruptured fault. Beyond the limits of the strike of the fault, it is calculated perpendicular to the extension of the projection of the top edge of the fault along the strike. This distance metric is used in GMMs such as Abrahamson and Silva (2008), Chiou and Youngs (2008), and Campbell and Bozorgnia (2014) to quantify hanging wall effects. Unlike other distance metrics, which always have positive values, R_X can be positive or negative – positive for sites on the hanging wall side of the fault and negative for sites on the footwall side of the fault (Kaklamanos et al., 2011). R_Y is the closest parallel distance from the site to the projection of the ruptured fault. Both R_X and R_Y can be classified under fault-based distances. Figure 3.1 shows the different distance metrics discussed in this study.

To develop relationships between the different distance metrics, we need to develop a database that encompasses the values of these distance metrics at different magnitudes, faulting conditions, location of the hypocenter, and other factors. While databases are available for these purposes based on the recorded earthquakes, these are not exhaustive. Since most recorded earthquakes are for small magnitudes and at large distances, there may be a bias in the relationship developed using such databases. To avoid bias, we decided to develop the relationship between different distance

metrics based on the geometry of the fault. This approach provides us with the relationship between different distance metrics for a given magnitude, hypocenter location, azimuth, and the style of faulting. To develop the geometrical relationship, we use R_{JB} as the reference distance. Other variables include the magnitude of the earthquake (M), the dip angle of the fault (δ), and the azimuth angle from the center of the fault to the site of interest (θ). Based on these parameters, we establish the geometrical relationship to other distance parameters referred to as target distance metrics (R_{target}), such as R_{RUP}, R_{EPI}, and $R_{HYP.}$ The relations and their derivation haven been discussed in this chapter.

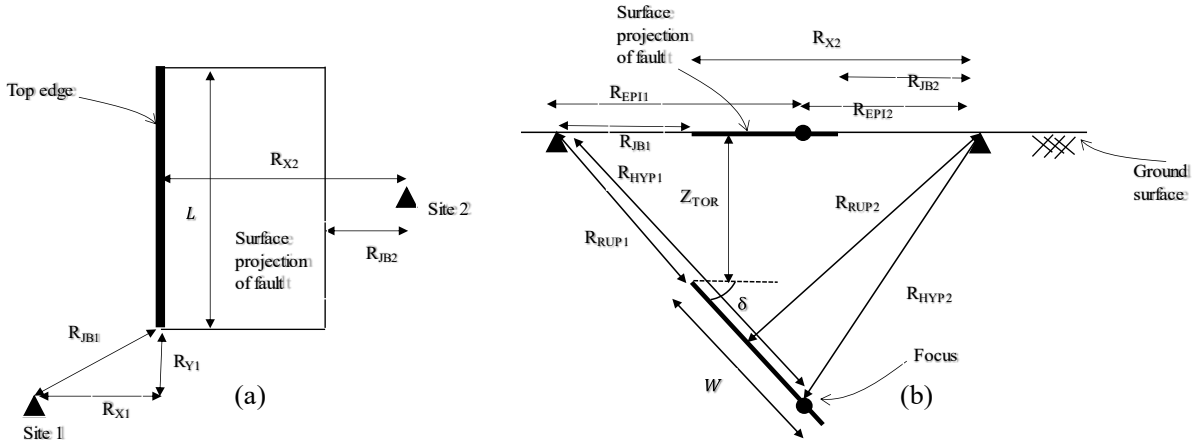

Figure 3.1 (a) Illustration of the plan view of the fault. The rectangle is the surface projection of the fault, with the bold line as the surface projection of the top edge of the fault. The triangles are locations of possible sites or stations with their respective distance metrics. Site 1 is located at the footwall of the fault and has a negative value for $R_{X,}$ while Site 2 is located at the hanging wall side of the fault and has a positive R_X value. R_Y is 0 for Site 2. (b) Illustration of the vertical cross-section of a fault. Also shown are various distance metrics R_X, $R_{JB,}$ R_{RUP}, R_{EPI}, and R_{HYP} measured from the site (shown by a triangle) to the fault.

3.2 Equation for distance metrics based on the geometry of the fault

3.2.1 Equation for R_X and R_Y

The equation for R_X is dependent on the geometrical properties of the fault, such as the length (L), width (W) and dip angle (δ), reference distance (R_{JB}), and the azimuth (θ) of the site from the center of the ruptured fault. We derive the equation for R_X for vertical strike-slip fault ($\delta = 90°$) and dip-slip fault ($\delta \neq 90°$).

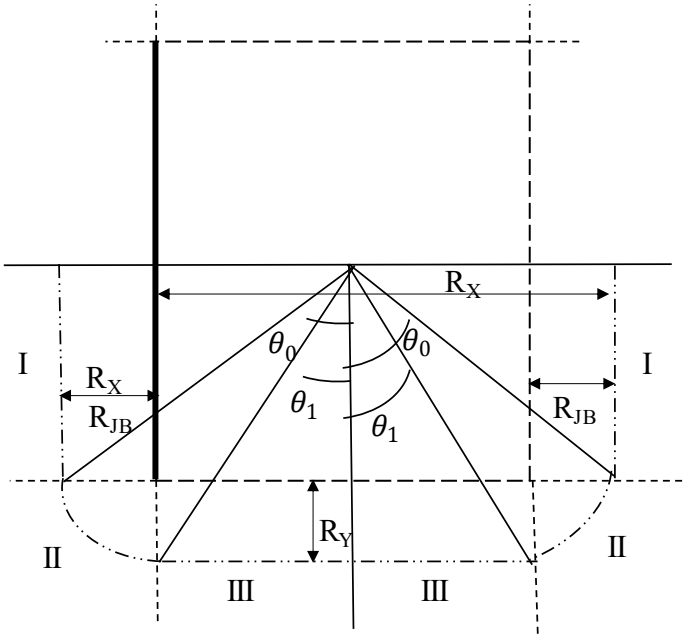

Figure 3.2 Illustration of the plan view of dip-slip fault, which shows R_{JB}, R_X, and R_Y for different cases based on azimuth angle ($\boldsymbol{\theta}$).

Due to the symmetry of the fault, we can derive the equations for R_X for six cases (Kayastha et al., 2022), as shown in Figure 3.2. The six cases can be reduced to three cases, as shown in Figure 3.3, if we only consider positive values of the azimuth angle (θ). θ_0 and θ_1 are shown in Figure 3.2 and the equations are listed in Equation 3.9.

Case-I: $0 \leq |\theta| < \theta_1$

when $\theta \in \left(0, \frac{\pi}{2}\right)$,

$$\tan(\theta) = \frac{P}{\frac{L}{2} + R_{JB}} \Rightarrow P = \tan(\theta)\left(\frac{L}{2} + R_{JB}\right)$$

$$y' = \frac{W\cos(\delta)}{2} - P = \frac{W\cos(\delta)}{2} - \tan(\theta)\left(\frac{L}{2} + R_{JB}\right)$$

$$R_X = W\cos(\delta) - y' = W\cos(\delta) - \frac{W\cos(\delta)}{2} + \tan(\theta)\left(\frac{L}{2} + R_{JB}\right)$$

$$< R_X >_\theta = \frac{W\cos(\delta)}{2} + \tan(\theta)\left(\frac{L}{2} + R_{JB}\right) \quad (3.1)$$

when $\theta \in \left(-\frac{\pi}{2}, 0\right)$,

$$\tan(\theta) = \frac{P}{\frac{L}{2} + R_{JB}} \Rightarrow P = \tan(\theta)\left(\frac{L}{2} + R_{JB}\right)$$

$$R_X = \frac{W\cos(\delta)}{2} - P$$

$$< R_X >_\theta = \frac{W\cos(\delta)}{2} - \tan(\theta)\left(\frac{L}{2} + R_{JB}\right) \quad (3.2)$$

Case-II: $\theta_1 \leq |\theta| \leq \theta_0$

when $\theta \in \left(0, \frac{\pi}{2}\right)$,

$$R_X = \frac{W\cos(\delta)}{2} + R_{cref}\sin(\theta)$$

$$< R_X >_\theta = \frac{W\cos(\delta)}{2} + R_{cref}\sin(\theta) \quad (3.3)$$

when $\theta \in \left(-\frac{\pi}{2}, 0\right)$,

$$R_X = \frac{W\cos(\delta)}{2} - R_{cref}\sin(\theta)$$

$$< R_X >_\theta = \frac{W\cos(\delta)}{2} - R_{cref}\sin(\theta) \quad (3.4)$$

Case-III: $\theta_0 \leq |\theta| \leq 90$

when $\theta \in \left(0, \frac{\pi}{2}\right)$,

$$R_X = W\cos(\delta) + R_{JB}$$

$$< R_X >_\theta = W\cos(\delta) + R_{JB} \quad (3.5)$$

when $\theta \in \left(-\frac{\pi}{2}, 0\right)$,

$$R_X = R_{JB}$$

$$< R_X >_\theta = < R_X >_\theta = R_{JB} \quad (3.6)$$

where R_{cref} is the epicentral distance calculated from the site of interest to the center of the fault rupture projected on the surface. The equation for R_{cref} was provided by Tavakoli et al. (2018) and is listed below.

For vertical strike-slip faults,

$$R_{cref} = \begin{cases} \sqrt{\left(\frac{L}{2}\right)^2 + R_{JB}^2 - 2 * \left(\frac{L}{2}\right) * R_{JB} * \cos\left[180 - \left(\theta + \sin^{-1}\left(\frac{\sin(\theta) * \frac{L}{2}}{R_{JB}}\right)\right)\right]} & \text{if } 0 \le \theta < \theta_0 \\ \frac{R_{JB}}{\sin(\theta)} & \text{if } \theta_0 \le \theta < 90 \end{cases} \quad (3.7)$$

For dip-slip fault,

$$R_{Cref} = \begin{cases} \frac{R_{JB} + \frac{L}{2}}{\cos(\theta)} & 0 \le \theta < \theta_1 \\ \sqrt{R_{JB}^2 + \left(\frac{W\cos(\delta)}{2}\right)^2 + \left(\frac{L}{2}\right)^2 - 2\sqrt{\left(\frac{W\cos(\delta)}{2}\right)^2 + \left(\frac{L}{2}\right)^2} R_{JB}\cos(\gamma)} & \theta_1 \le \theta < \theta_0 \\ \frac{\left(\frac{W\cos(\delta)}{2}\right) + R_{JB}}{\sin(\theta)} & \theta_0 \le \theta < 90 \end{cases} \quad (3.8)$$

in which,

$$\theta_0 = \tan^{-1}\left[\frac{\frac{W\cos(\delta)}{2} + R_{JB}}{\frac{L}{2}}\right]$$

$$\theta_1 = \tan^{-1}\left[\frac{\frac{W\cos(\delta)}{2}}{R_{JB} + \frac{L}{2}}\right] \quad (3.9)$$

$$\gamma = 180 - \left(\sin^{-1}\left[\frac{\sin(|\theta - \alpha|)\sqrt{\left(\frac{W\cos(\delta)}{2}\right)^2 + \left(\frac{L}{2}\right)^2}}{R_{JB}}\right] + |\theta - \alpha|\right)$$

$$\alpha = \tan^{-1}\left[\frac{y}{\frac{L}{2}}\right]$$

The equations for R_X have been summarized in Table 3.1 for different cases based on the azimuth angle (θ), which is the angle from the center of the fault to the site (Kayastha et al., 2022).

Similarly, we can determine the equations to calculate R_Y, which are presented in equation (3.10).

$$R_Y = \begin{cases} 0 & |\theta| \geq \theta_0 \\ R_{cRef}\cos(|\theta|) - 0.5L & \theta_1 \leq |\theta| < \theta_0 \\ R_{JB} & |\theta| < \theta_1 \end{cases} \quad (3.10)$$

Table 3.*1* Equation to calculate R_X based on R_{JB}, length (L) and width (W) of the fault, dip angle ($\boldsymbol{\delta}$), and azimuth angle ($\boldsymbol{\theta}$).

Azimuth angle	Case	Equation
$\theta \in \left(0, \frac{\pi}{2}\right)$	$0 \leq \lvert\theta\rvert < \theta_1$	$0.5W\cos(\delta) + \tan(\theta) * \left(0.5L + R_{JB}\right)$
$\theta \in \left(-\frac{\pi}{2}, 0\right)$		$0.5W\cos(\delta) - \tan(\lvert\theta\rvert) * \left(0.5L + R_{JB}\right)$
$\theta \in \left(0, \frac{\pi}{2}\right)$	$\theta_1 \leq \lvert\theta\rvert < \theta_0$	$0.5W\cos(\delta) + R_{cRef}\sin(\theta)$
$\theta \in \left(-\frac{\pi}{2}, 0\right)$		$-0.5W\cos(\delta) + R_{cRef}\sin(\lvert\theta\rvert)$
$\theta \in \left(0, \frac{\pi}{2}\right)$	$\lvert\theta\rvert \geq \theta_0$	$W\cos(\delta) + R_{JB}$
$\theta \in \left(-\frac{\pi}{2}, 0\right)$		R_{JB}

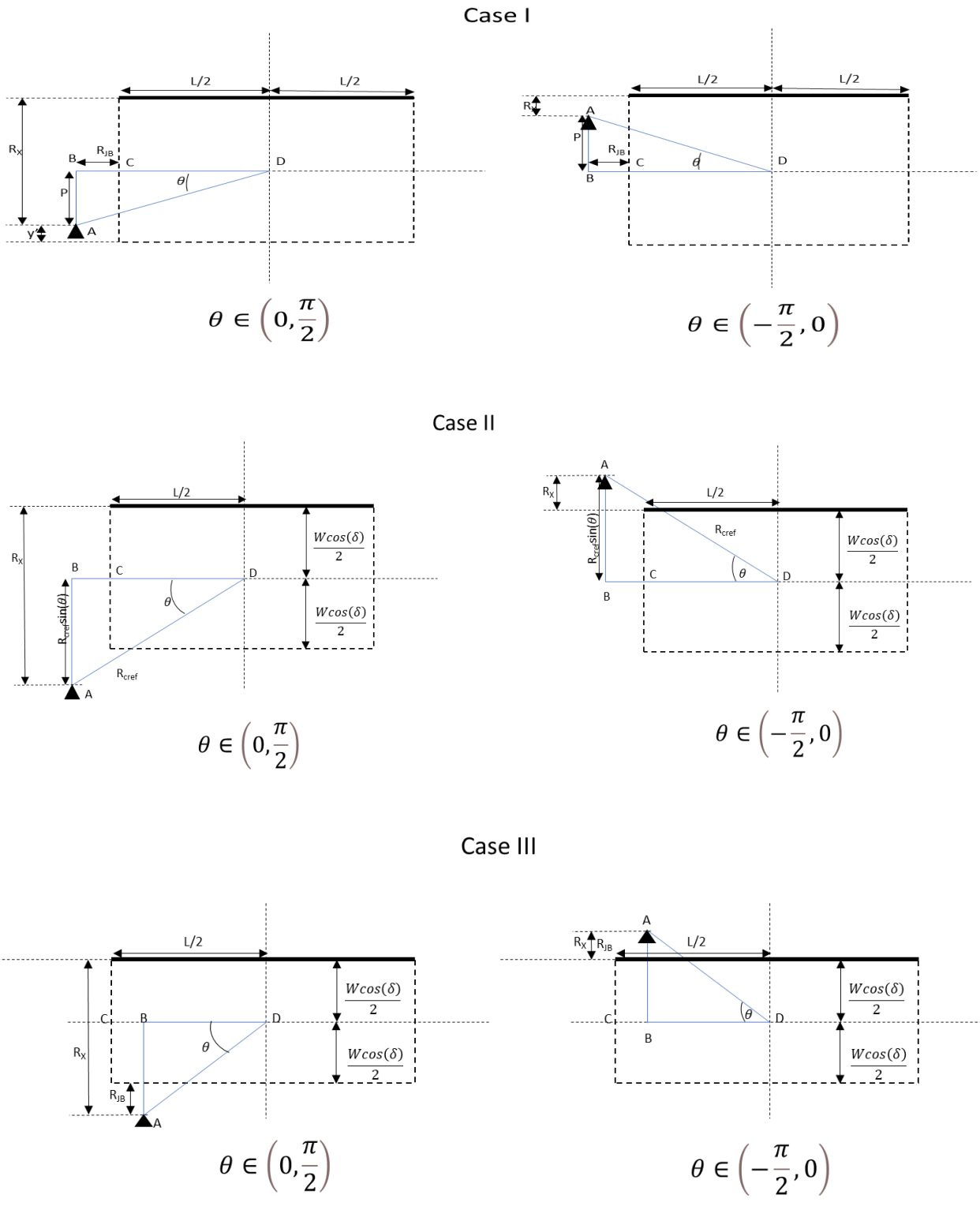

Figure 3.3 Detailed diagram for the derivation of R_X for different cases.

3.2.2 Equation for R_{RUP}

The equations to determine R_{RUP} has been provided by Kaklamanos et al. (2011) and are listed below.

For strike-slip fault,

$$< R_{RUP} >_{\theta} = \sqrt{< R_X >_{\theta}^2 + Z_{TOR}^2 + < R_Y >_{\theta}^2} \tag{3.11}$$

For dip-slip fault,

Case-I: For footwall

$$< R_{RUP} >_{\theta} = \sqrt{< R_X >_{\theta}^2 + Z_{TOR}^2 + < R_Y >_{\theta}^2} \tag{3.12}$$

Case-II: $R_X < R_{S1}$

As shown in Figure 3.4,

$$\tan(\delta) = \frac{R_{S1}}{Z_{TOR}} \Rightarrow R_{S1} = Z_{TOR} \tan(\delta)$$

$$R'_{RUP} = \sqrt{R_X^2 + Z_{TOR}^2}$$

$$< R_{RUP} >_{\theta} = \sqrt{< R_X >_{\theta}^2 + Z_{TOR}^2 + < R_Y >_{\theta}^2} \tag{3.13}$$

Case-III: $R_{S1} \leq R_X \leq R_{S2}$

$$\tan(\delta) = \frac{Z_{TOR}}{R_{X1}} \Rightarrow R_{X1} = \frac{Z_{TOR}}{\tan(\delta)}$$

$$\sin(\delta) = \frac{R_{RUP}}{R_{X1} + R_X}$$

$$\Rightarrow R_{RUP} = (R_{X1} + R_X)\sin(\delta)$$

$$= (R_{X1}\sin(\delta) + R_X \sin(\delta))$$

$$= \left(\frac{Z_{TOR}}{\tan(\delta)}\sin(\delta) + R_X \sin(\delta)\right)$$

$$R'_{RUP} = R_X \sin(\delta) + Z_{TOR}\cos(\delta)$$

$$< R_{RUP} >_\theta = \sqrt{[< R_X >_\theta \sin(\delta) + Z_{TOR}\cos(\delta)]^2 + < R_Y >_\theta^2} \quad (3.14)$$

Case-IV: $R_X > R_{S2}$

$$\cos(\delta) = \frac{W}{R_{X1}} \Rightarrow R_{X1} = \frac{W}{\cos(\delta)} = Wsec(\delta)$$

$$\tan(\delta) = \frac{R_{X2}}{Z_{TOR}} \Rightarrow R_{X2} = Z_{TOR}\tan(\delta)$$

$$R_{S2} = R_{X1} + R_{X2} = Wsec(\delta) + Z_{TOR}\tan(\delta)$$

$$R_{X3} = R_X - Wcos(\delta)$$

$$R'_{RUP} = \sqrt{\left(Z_{TOR} + Wsin(\delta)\right)^2 + R_{X3}^2} = \sqrt{\left(Z_{TOR} + Wsin(\delta)\right)^2 + \left(R_X - Wcos(\delta)\right)^2}$$

$$< R_{RUP} >_\theta = \sqrt{\left(Z_{TOR} + Wsin(\delta)\right)^2 + \left(< R_X >_\theta - Wcos(\delta)\right)^2 + < R_Y >_\theta^2} \quad (3.15)$$

The equations can be summarized as follows:

$$R_{RUP} = \begin{cases} \sqrt{< R_X >_\theta^2 + Z_{TOR}^2 + < R_Y >_\theta^2} & R_X < R_{S1} \\ \sqrt{[< R_X >_\theta \sin(\delta) + Z_{TOR}\cos(\delta)]^2 + < R_Y >_\theta^2} & R_{S1} \le R_X \le R_{S2} \\ \sqrt{\left(Z_{TOR} + Wsin(\delta)\right)^2 + \left(< R_X >_\theta - Wcos(\delta)\right)^2 + < R_Y >_\theta^2} & R_X > R_{S2} \end{cases} \quad (3.16)$$

where R_X and R_Y can be calculated using the equations discussed previously. Z_{TOR} is the depth to the top of the rupture. Using the equations, we can determine the R_{RUP} at different magnitudes and dip angles.

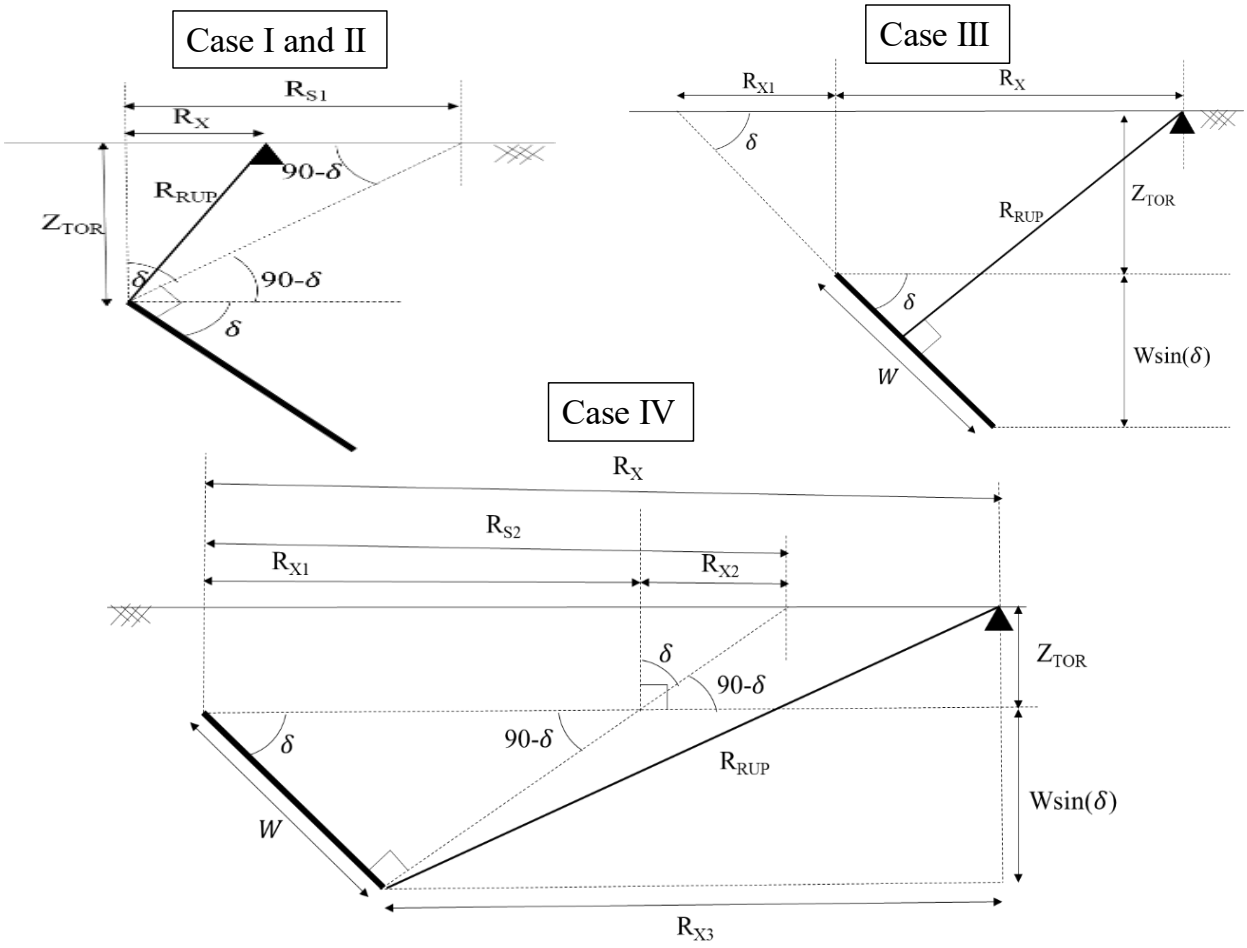

Figure 3.4 Detailed diagram for the derivation of R_{RUP} for different cases.

3.2.3 Equation for R_{EPI} and R_{HYP}

As shown in Figure 3.5, we can calculate R_{EPI} and R_{HYP} based on the geometry of the fault and the location of the focus (Kayastha et al., 2022). The location of the focus is specified by variables (x,y,z), where x is measured along the length from the center of the fault, y is measured along the width from one end of the fault, and z is measured from the ground surface. The calculation for R_C is discussed in the next section.

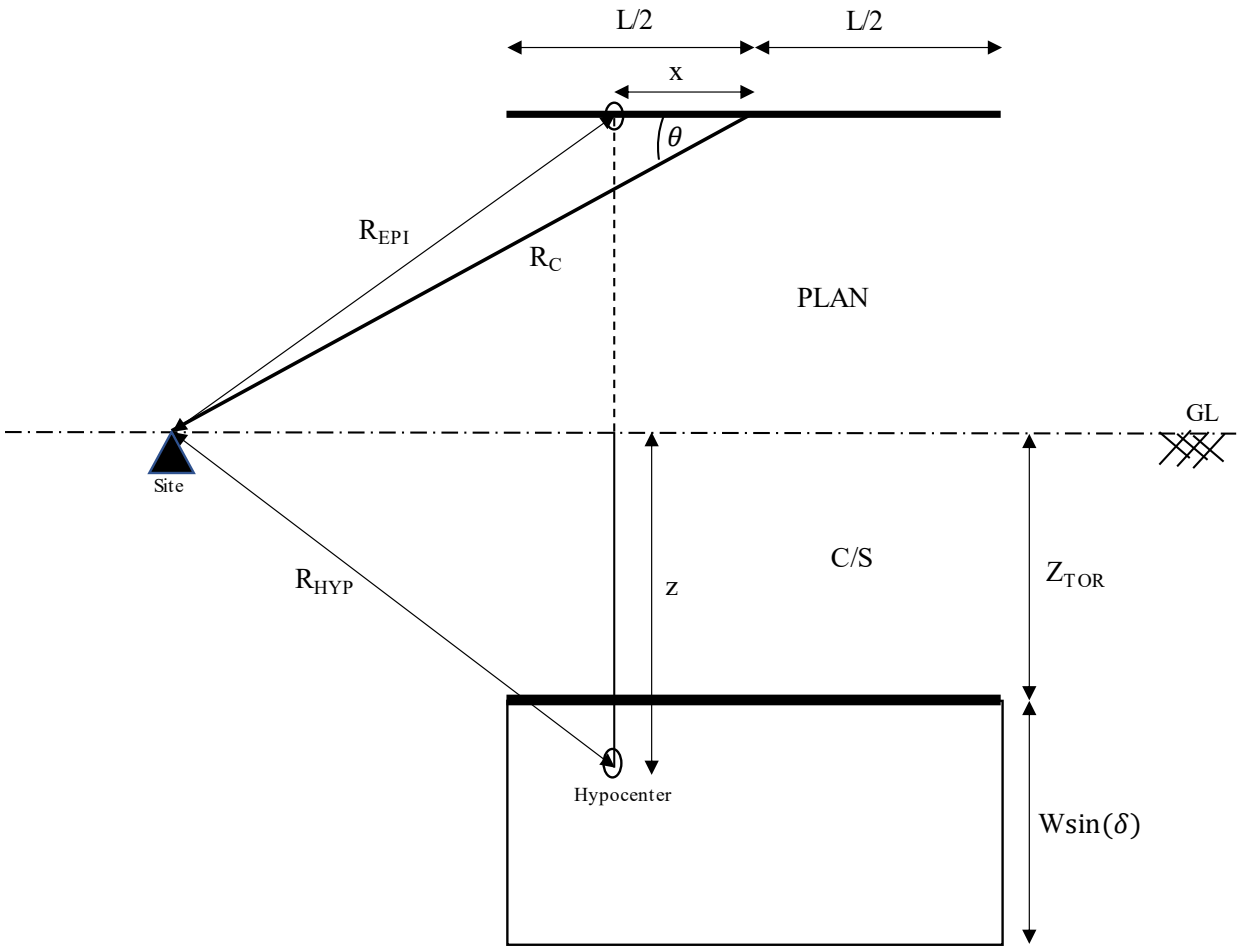

Figure 3.5 Detailed diagram for the derivation of R_{EPI} and R_{HYP} for a vertical strike-slip fault. The figure above the dotted lines shows the plan or the top-view of the fault with length (L). 'x' is the distance from the center of the fault to the assumed epicenter along the length of the fault. Since it is a vertical strike-slip fault, the width of the fault (W) and the location of the epicenter along the width (y) is not considered. '$\boldsymbol{\theta}$' is the azimuth angle from the center of the fault to the site. The figure below the dotted lines shows the cross-section of the fault with 'z' as the depth from the ground surface to the hypocenter.

In Figure 3.5, using cosine law,

$$R_{EPI}^2 = R_C^2 + x^2 \pm 2|x|R_C\cos(\theta')$$

$$R_{EPI} = \sqrt{R_C^2 + x^2 \pm 2|x|R_C\cos(\theta')} \tag{3.17}$$

Similarly,

$$R_{HYP}^2 = R_{EPI}^2 + z^2$$

$$R_{HYP} = \sqrt{R_{EPI}^2 + z^2}$$

$$R_{HYP} = \sqrt{R_c^2 + x^2 \pm 2|x|R_C \cos(\theta') + z^2} \tag{3.18}$$

For strike-slip fault, $\theta' = \theta$.

3.2.3.1 Strike-slip fault

For the strike-slip fault, the width of the fault does not affect the estimation of R_{EPI} and R_{HYP}. To determine R_{EPI} and R_{HYP}, we define the term R_C as shown in Figure 3.6. R_C is the distance from the site to the center of the fault. So, if the epicenter is located in the center of the fault, $R_{EPI} = R_C$. The equation for R_C has been divided into two cases based on the azimuth of the fault to the site. The hinge azimuth (θ_0), where the two cases have been separated, is based on the azimuth of the fault where R_Y has a non-zero value. When $\theta < \theta_0$, R_Y has a non-zero value while $R_Y = 0$ when $\theta \geq \theta_0$.

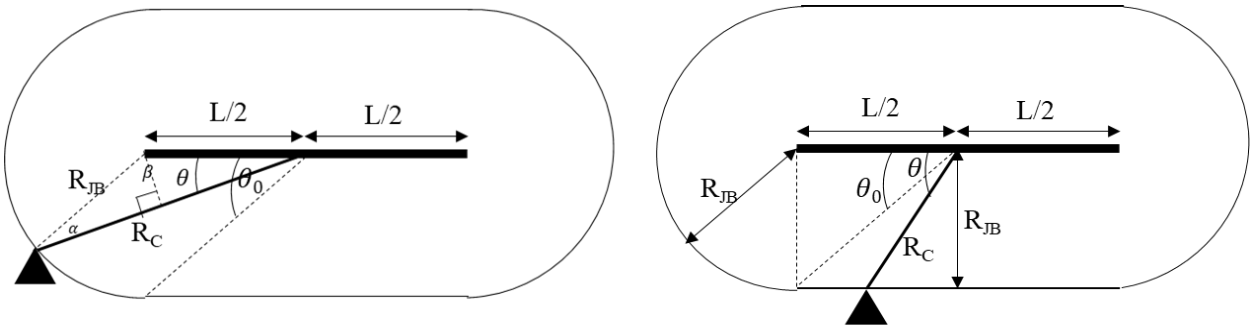

$\boldsymbol{0 \leq \theta < \theta_0}$ $\qquad$ $\boldsymbol{\theta_0 \leq \theta < 90}$

Figure 3.6 Detailed diagram for the derivation of R_C for different cases for vertical strike-slip fault.

If $\theta_0 \leq \theta < 90$

$$\sin(\theta) = \frac{R_{JB}}{R_C}$$

$$R_C = \frac{R_{JB}}{\sin(\theta)} \tag{3.19}$$

If $0 \leq \theta < \theta_0$

$$\sin(\theta) = \frac{P}{\frac{L}{2}} \quad \Rightarrow \quad P = \frac{L}{2} * \sin(\theta)$$

$$\sin(\alpha) = \frac{P}{R_{JB}} = \frac{\frac{L}{2} * \sin(\theta)}{R_{JB}} \quad \Rightarrow \quad \alpha = \sin^{-1}\left(\frac{\sin(\theta) * \frac{L}{2}}{R_{JB}}\right)$$

$$\beta = 180 - (\theta + \alpha) = 180 - \left[\theta + \sin^{-1}\left(\frac{\sin(\theta) * \frac{L}{2}}{R_{JB}}\right)\right]$$

Using cosine law in ABC,

$$R_C^2 = \left(\frac{L}{2}\right)^2 + R_{JB}^2 - 2 * \frac{L}{2} * R_{JB} * \cos(\beta)$$

$$R_C = \sqrt{\left(\frac{L}{2}\right)^2 + R_{JB}^2 - 2 * \left(\frac{L}{2}\right) * R_{JB} * \cos\left(180 - (\theta + \alpha) = 180 - \left[\theta + \sin^{-1}\left(\frac{\sin(\theta) * \frac{L}{2}}{R_{JB}}\right)\right]\right)} \qquad (3.20)$$

3.2.3.2 Dip-slip fault

For dip-slip faults, both the length and the width of the faults are required to determine the values for R_{EPI} and R_{HYP} as shown in Figure 3.7. So, the equations are different than for strike-slip fault.

If $0 \leq \theta < \theta_1$

$$\tan(\theta) = \frac{P}{R_{JB} + \frac{L}{2}} \quad \Rightarrow \quad P = \left(\frac{L}{2} + R_{JB}\right)\tan(\theta)$$

$$P' = y - y' = y - \left(\frac{W\cos(\delta)}{2} - P\right) = y - \left(\frac{W\cos(\delta)}{2} - \tan(\theta)\left(\frac{L}{2} + R_{JB}\right)\right)$$

$$\tan(\theta') = \frac{P'}{\frac{L}{2} + R_{JB}} = \frac{y - \left(\frac{W\cos(\delta)}{2} - \tan(\theta)\left(\frac{L}{2} + R_{JB}\right)\right)}{\frac{L}{2} + R_{JB}}$$

$$\cos(\theta') = \frac{R_{JB} + \frac{l}{2}}{R_C}$$

$$R_C = \frac{R_{JB} + \frac{L}{2}}{\cos(\theta')} \tag{3.21}$$

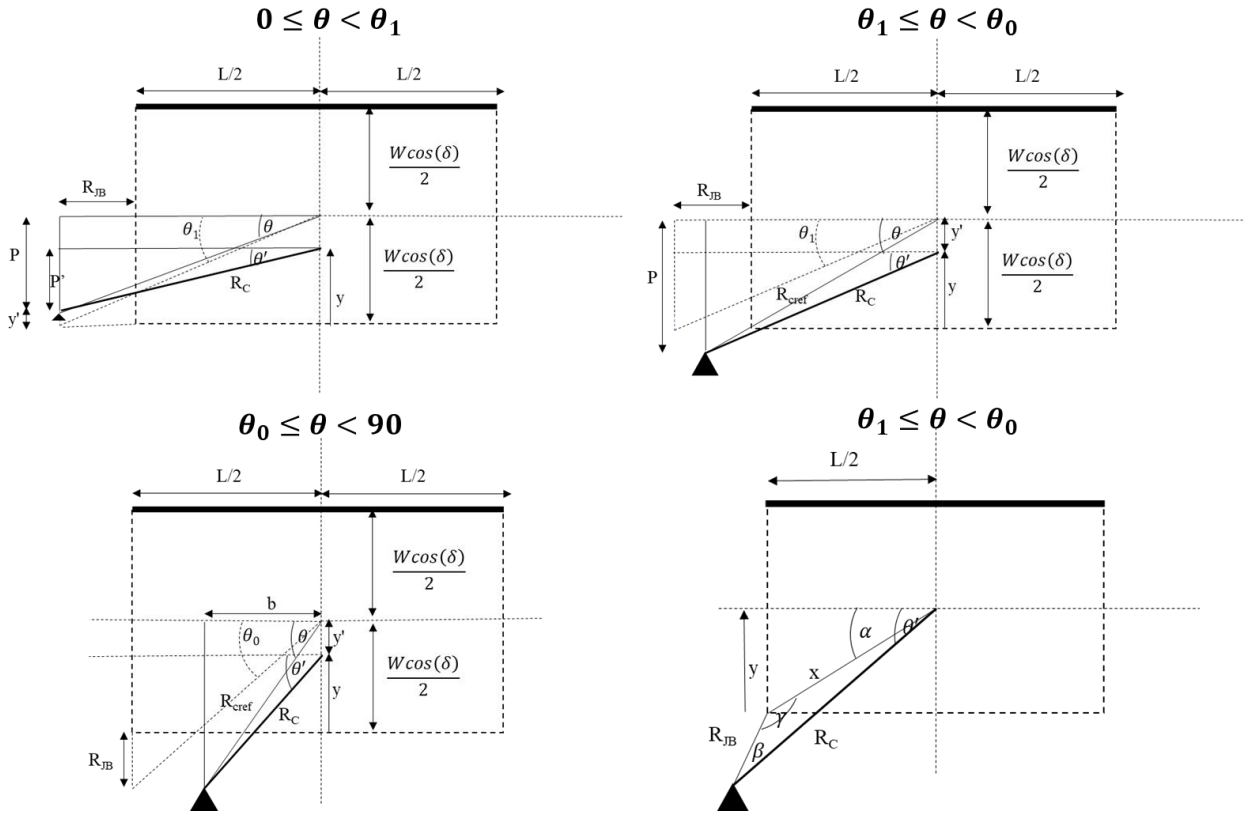

Figure 3.7 Detailed diagram for the derivation of R_C for different cases for dip-slip fault.

If $\theta_1 \le \theta < \theta_0$

$$\sin(\theta) = \frac{P}{R_{Cref}} \Rightarrow P = R_{Cref}\sin(\theta)$$

$$y' = \frac{Wcos(\delta)}{2} - y$$

$$\tan(\theta') = \frac{P - y'}{R_{Cref}\cos(\theta)} = \frac{R_{Cref}\sin(\theta) - \left(\frac{Wcos(\delta)}{2} - y\right)}{R_{Cref}\cos(\theta)}$$

$$\tan(\alpha) = \frac{y}{\frac{L}{2}} \quad \Rightarrow \quad \alpha = \tan^{-1}\left(\frac{y}{\frac{L}{2}}\right)$$

In ABC, using sine law,

$$\frac{\sin(\beta)}{x} = \frac{\sin(\theta' - \alpha)}{R_{JB}}$$

$$x = \sqrt{y^2 + \left(\frac{L}{2}\right)^2}$$

$$\sin(\beta) = \frac{\sin(\theta' - \alpha)}{R_{JB}} * x = \frac{\sin(\theta' - \alpha)\sqrt{y^2 + \left(\frac{L}{2}\right)^2}}{R_{JB}}$$

$$\gamma = 180 - \beta - (\theta' - \alpha) = 180 - \sin^{-1}\left(\frac{\sin(\theta' - \alpha)\sqrt{y^2 + \left(\frac{L}{2}\right)^2}}{R_{JB}}\right) - (\theta' - \alpha)$$

Using cosine law,

$$R_C^2 = R_{JB}^2 + x^2 - 2xR_{JB}\cos(\gamma)$$

$$R_C = \sqrt{R_{JB}^2 + y^2 + \left(\frac{L}{2}\right)^2 - 2\sqrt{y^2 + \left(\frac{L}{2}\right)^2}\, R_{JB}\cos(\gamma)} \tag{3.22}$$

If $\theta_0 \leq \theta < 90$

$$\tan(\theta) = \frac{\frac{Wcos(\delta)}{2} + R_{JB}}{b} \quad \Rightarrow \; b = \frac{\left(\frac{Wcos(\delta)}{2} + R_{JB}\right)}{\tan(\theta)}$$

$$\tan(\theta') = \frac{y + R_{JB}}{b} = \frac{y + R_{JB}}{\frac{\left(\frac{Wcos(\delta)}{2} + R_{JB}\right)}{\tan(\theta)}} = \tan(\theta)\left(\frac{y + R_{JB}}{\frac{Wcos(\delta)}{2} + R_{JB}}\right)$$

$$\sin(\theta') = \frac{y + R_{JB}}{R_C}$$

$$R_C = \frac{y + R_{JB}}{\sin(\theta')} \tag{3.23}$$

In summary,

For strike-slip fault,

$$R_c = \begin{cases} \sqrt{\left(\frac{L}{2}\right)^2 + R_{JB}^2 - 2 * \left(\frac{L}{2}\right) * R_{JB} * \cos\left(180 - (\theta + \alpha) = 180 - \left[\theta + \sin^{-1}\left(\frac{\sin(\theta) * \frac{L}{2}}{R_{JB}}\right)\right]\right)} & 0 \le \theta < \theta_0 \\ \frac{R_{JB}}{\sin(\theta)} & \theta_0 \le \theta < 90 \end{cases} \tag{3.24}$$

For dip-slip fault,

$$R_C = \begin{cases} \frac{R_{JB} + \frac{L}{2}}{\cos(\theta')} & 0 \le \theta < \theta_1 \\ \sqrt{R_{JB}^2 + y^2 + \left(\frac{L}{2}\right)^2 - 2\sqrt{y^2 + \left(\frac{L}{2}\right)^2}\, R_{JB}\cos(\gamma)} & \theta_1 \le \theta < \theta_0 \\ \frac{y + R_{JB}}{\sin(\theta')} & \theta_0 \le \theta < 90 \end{cases} \tag{3.25}$$

For dip-slip faults, change $\boldsymbol{y = Wcos(\delta) - y}$, if $\boldsymbol{\theta < 0}°$ i.e., the site lies in the top half of the projection of the fault (The derivation is shown for conditions when site lies below the half of the fault projection).

3.3 Fault model assumptions

The data for this study is developed based on the centroid-centered virtual site model. In this approach, the fault is fixed, and the virtual site moves around the fault. The location of the azimuth is dependent on the azimuth of the site from the centroid of the ruptured fault. The virtual sites are located at a constant R_{JB} from the fault. For a constant R_{JB}, a range of values for other distance metrics (R_{RUP}, R_{EPI}, R_{HYP}) can be obtained based on the magnitude, dip angle, and azimuth of the

fault. R_{JB} is chosen as the reference distance because there is only one possible station for a known fault at a given azimuth. For R_{EPI}, the location of the station at a given azimuth can vary based on the location of the epicenter of the fault. The mean value of the reference distance metric is obtained to develop the statistical relationship between the different distance metrics. For computational efficiency, instead of solving for the integral, we have discretized the fault along the length, width, and depth of the fault, with an azimuth increment of 1° for the virtual site. The length and width are discretized such that the reference sites are densely spaced closer to the fault and sparsely spaced away from the fault.

Different fault ruptures have been considered based on the size of the rupture, the geometry of the rupture plane, and the location of the hypocenter. The geometry of the rupture plane is modeled as a rectangular plane with length (L), width (W), dip angle (δ), and depth to the top of the rupture (Z_{TOR}), as shown in Figure 3.1. The size of the rupture, based on magnitude, is used to model the length and width of the fault. We have focused on the Central and Eastern US region. So, we used the equation provided in Somerville (2014), developed for the CEUS region, to calculate the ruptured area (RA) of the rupture plane for different magnitudes. We use a fixed length-to-width aspect ratio of 1. The hypocentral depth values are based on Scherbaum et al. (2004). If the calculated rupture plane is extended above the surface, the width of the fault is adjusted such that the top of the fault lies on the surface. The width is restricted to the seismogenic zone, assumed at a depth of 15 km (Shaw and Wesnousky, 2008). Modification of Z_{TOR} also changes the dimensions for the width of the fault (assuming a fixed hypocentral depth). Consequently, the length is increased to maintain a constant ruptured area for a given M. The data is generated for M values between 5 to 8, dip angles from 10° to 90°, and R_{JB} values up to 200 km. The azimuth value is

varied from 0° to 360°. We determine the target distances, such as R_{EPI}, R_{HYP}, and $R_{RUP,}$ for each geometrical scenario using the equations discussed previously.

This approach provides us with a range of target distance values for a given R_{JB} value. The target distances depend on R_{JB}, length (L), width (W), and dip (δ) of the rupture plane, the azimuth angle (α), the hypocentral depth, depth to the top of the rupture (Z_{TOR}), and the style of faulting (strike-slip or dip-slip). Regression analysis based on the non-linear least squares method is performed on the obtained data to develop empirical relations for R_{RUP} and R_{EPI} based on the R_{JB}, magnitude of the fault and dip angle, and R_{HYP} based on R_{JB}, M, δ, and Z_{TOR}.

3.3.1 Equation for mean and variance of Rupture distance

The mean R_{RUP} can be calculated as follows:

$$E[R_{RUP}|R_{JB}, M, \delta] = \int_{-3}^{3}\int_{0}^{2\pi} R_{RUP}(\theta,\epsilon)p(\theta)p(\epsilon)d\theta d\epsilon \tag{3.26}$$

where, $R_{RUP}(\theta,\epsilon)$ is the rupture distance from the fault to the site at a given azimuth (θ). $'\epsilon'$ is used to incorporate the uncertainties in the scaling relationship used to determine 'L' and 'W' from the magnitude of the fault. We have used ±3 standard deviations, assuming a standard normal distribution for our calculation. Since R_{RUP} is a fault-based distance metric, we do not need to discretize the fault. Instead, we calculate R_{RUP} values at different azimuth values from the fault for a given R_{JB}, dip angle, and magnitude.

Instead of defining a complex function to express the distribution of θ, we used a small spacing for θ, which provided results with acceptable accuracy without hampering the computational efficiency (Campbell and Gupta, 2018). For our calculation, we have used a spacing of 1° with

uniform distribution ($P(\theta) = 1/2\pi$). For 'ϵ', we used a spacing of 1.0. We have calculated the mean values at different dip angles from 10° to 90° with a spacing of 10°.

Similarly, to calculate the variance of R_{RUP}, we can use the following equation:

$$\sigma^2_{[R_{RUP}|R_{JB},M,\delta]} = \int_{-3}^{3}\int_{0}^{2\pi} \left[R_{RUP}(\theta,\epsilon) - E\left[R_{RUP}\middle|R_{JB},M,\delta\right]\right]^2 p(\theta)p(\epsilon)d\theta d\epsilon \quad (3.27)$$

3.3.2 Equation for mean and variance of Epicentral distance

The mean R_{EPI} can be determined for a given R_{JB}, δ, and magnitude as follows:

$$E[R_{EPI}|R_{JB},M,\delta] = \int_{-3}^{3}\int_{0}^{2\pi}\int_{0}^{Wcos(\delta)}\int_{-0.5L}^{0.5L} R_{EPI}(x,y,\theta,\epsilon)p(x)p(y)p(\theta)p(\epsilon)dxdyd\theta d\epsilon \quad (3.28)$$

where, $R_{EPI}(x,y,\theta,\epsilon)$ is the distance from the epicenter (x, y) of the fault to the site located at an azimuth angle (θ) from the fault, and 'ϵ' has been defined previously. Using this equation, we can obtain R_{EPI} from the fault to the site at different R_{JB} and θ. For the calculation, we determine the mean value of R_{EPI} at all possible $\theta \in (0°, 360°)$ for a given R_{JB}, magnitude, and dip angle. 'x' and 'y' are the variables along the length and the width of the fault. We can use different distribution functions to define the spacing that can describe the characteristics of the fault rupture. We have used Mai et al. (2005) for our calculations to determine the hypocenter distribution along the strike and down-dip direction. After integration along the length and width of the fault, all possible locations of the epicenter can be considered.

The equation for the variance of R_{EPI} can be calculated as:

$$\sigma^2_{[R_{EPI}|R_{JB},M,\delta]} = \int_{-3}^{3}\int_{0}^{2\pi}\int_{0}^{W\cos(\delta)}\int_{-0.5L}^{0.5L}\left[R_{EPI}(x,y,\theta,\epsilon) - E\left[R_{EPI}\middle|R_{JB},M,\delta\right]\right]^2 * p(x)p(y)p(\theta)p(\epsilon)dxdyd\theta d\epsilon \quad (3.29)$$

3.3.3 Equation for mean and variance of Hypocentral distance

Most of the parameters required for R_{HYP} are already specified in equation (3.28). In addition, we also have the depth term 'z', which varies from the depth to the bottom of the rupture $\left(Z_{TOR} + W\sin(\delta)\right)$ to the depth to the top of the rupture (Z_{TOR}). The hypocentral depth is determined by Scherbaum et al. (2004).

The mean R_{HYP} can be calculated as follows:

$$E[R_{HYP}|R_{JB},M,\delta] = \int_{-3}^{3}\int_{0}^{2\pi}\int_{Z_{TOR}}^{Z_{TOR}+W\sin(\delta)}\int_{0}^{W\cos(\delta)}\int_{-0.5L}^{0.5L} R_{HYP}(x,y,z,\theta,\epsilon)p(x) * p(y)p(z)p(\theta)p(\epsilon)dxdydzd\theta d\epsilon \quad (3.30)$$

The equation for the variance of R_{HYP} can be presented as:

$$\sigma^2_{[R_{HYP}|R_{JB},M,\delta]} = \int_{-3}^{3}\int_{0}^{2\pi}\int_{Z_{TOR}}^{Z_{TOR}+W\sin(\delta)}\int_{0}^{W\cos(\delta)}\int_{-0.5L}^{0.5L}\left[R_{HYP}(x,y,z,\theta,\epsilon) - E\left[R_{HYP}\middle|R_{JB},M,\delta\right]\right]^2 * p(x)p(y)p(z)p(\theta)p(\epsilon)dxdydzd\theta d\epsilon \quad (3.31)$$

3.4 Discussions

3.4.1 Distribution of the distances

Figure 3.8 and Figure 3.9 show the histogram plots for the difference between R_{RUP} and R_{JB} at different magnitudes and a R_{JB} of 10 km for a dip-slip fault with a dip angle of $50°$ and a vertical strike-slip fault, respectively. The difference can be modeled as a gamma distribution (shown as

the solid line) to determine the mean and the standard deviation of the target distance metric (Kayastha et al., 2021). For M 5, we can observe that the residuals for the dip-slip fault are mostly distributed between 2 km and 6 km. Below 2 km, the frequency distribution of the residuals is nearly zero. Since the fault is assumed to be deeper from the surface for smaller magnitudes, the depth of the ruptured fault is rarely zero. Due to the depth term, the frequency distribution of the residuals of R_{RUP} with R_{JB} is also rarely zero for smaller magnitudes. This is not observed at large distances (>100 km). As the magnitude increases, the fault is assumed to be closer to the surface. Hence, the frequency of the residuals below 2 km also increases. For the dip-slip fault, the increase in magnitude also increases the maximum residual value from 6 km at M 5.0 to 12 km at M 7.5. So, the residuals are concentrated between a few values for smaller magnitudes, and the range increases for larger magnitudes. Since only the length of the fault is used to determine the R_{RUP} for the vertical strike-slip fault, such variations are not observed, and the residuals range from 0 to 4 km for all magnitudes.

Figure 3.10 and Figure 3.11 show the histogram plots for the difference between R_{EPI} and R_{JB} at different magnitudes and a R_{JB} of 10 km for a dip-slip fault with a dip angle of 50° and a vertical strike-slip fault, respectively. We can similarly model the gamma distribution as shown by the solid lines. We can observe significant variation in the range for the residuals of R_{EPI} as the magnitude increases. Similar to residuals of R_{RUP}, the residuals of R_{EPI} are concentrated between a few values for smaller magnitudes, and the distribution is more spread out at larger magnitudes.

We have also plotted histograms for the residuals of R_{HYP} at different magnitudes at a R_{JB} of 10 km for a dip-slip fault with a dip angle of 50° and a vertical strike-slip fault as shown in Figure 3.12 and Figure 3.13, respectively. Instead of taking the difference between R_{HYP} and R_{JB} to

calculate the residuals, we have taken the difference of R_{HYP} with the square root of R_{JB} and Z_{TOR}. This is because the depth of the earthquake event is an important parameter for the R_{HYP}, especially at smaller distances and for larger magnitudes. The effect of depth is less pronounced at large distances. Based on the histogram plots, we can observe that the peak distribution of the residuals increases with increasing magnitude. The peak of the residuals is nearly 1 km for M 5.0 and 15 km for M 7.5 earthquake event. Similar to the residual plots for other target distances, the range is concentrated between a few values for smaller magnitudes, and the range increases as magnitude increases.

Similar distributions can be developed for each target distance metric at different R_{JB}, M, and δ. The mean and the standard deviation can be calculated for each distribution to obtain a dataset containing the target distance metrics and the reference parameters such as magnitude, Joyner-Boore distance, the dip angle of the fault, and depth to the top of the rupture. Based on an appropriate empirical form, we can conduct a non-linear regression analysis on the dataset. Alternatively, we can also implement different machine-learning algorithms to appropriately select relevant parameters to determine a parsimonious model that can determine the target distance metrics.

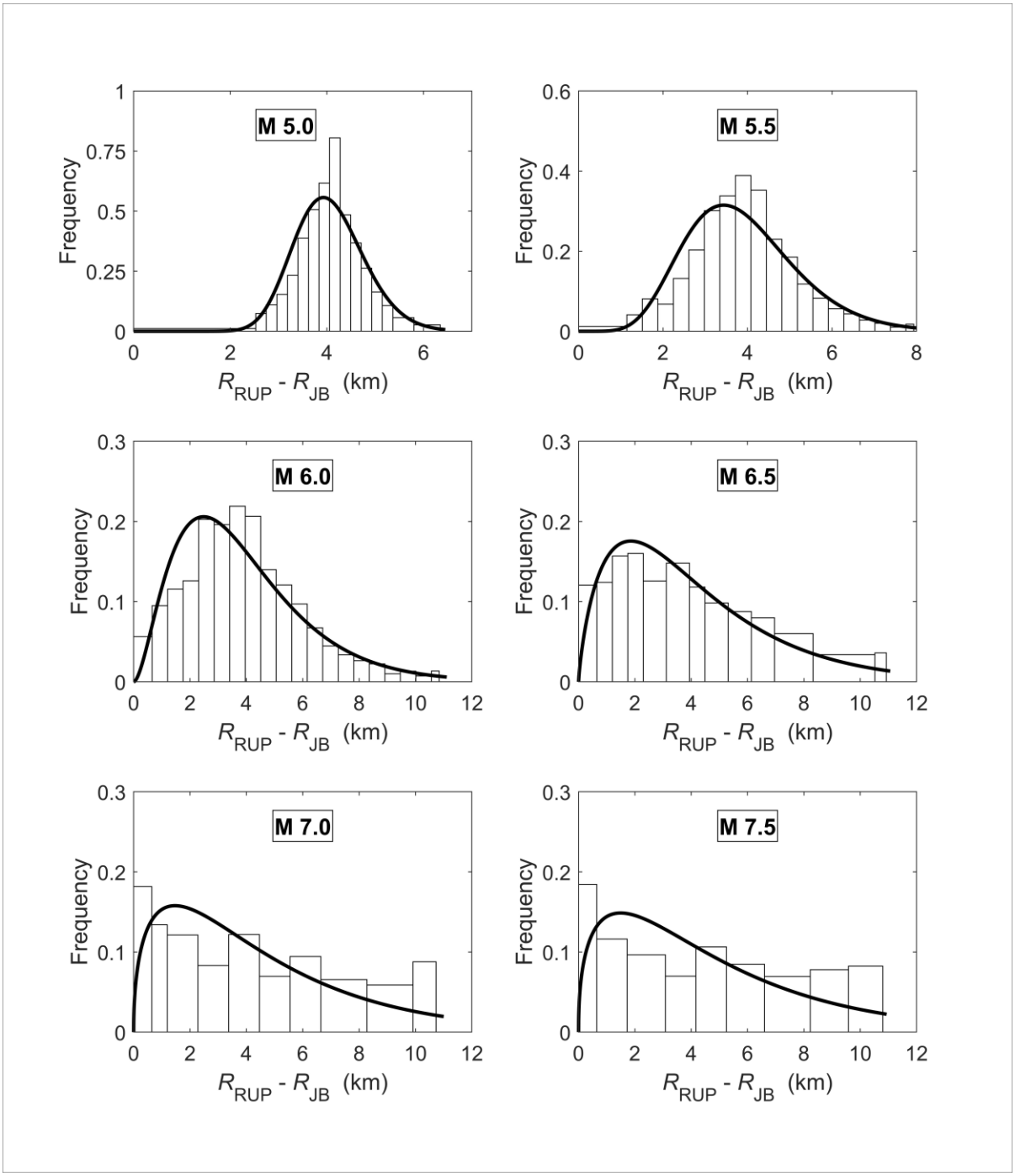

Figure 3.8 Histogram plots of the difference of R_{RUP} and R_{JB} for a dip-slip fault with dip angle **50**° at different magnitudes for a R_{JB} of 10 km. The solid line represents the gamma distribution fitted to the histogram. The mean and the standard deviation of the distribution can be used in regression analysis to determine the coefficients at different M, $R_{JB,}$ and $\boldsymbol{\delta}$ in the empirical equations for R_{RUP}.

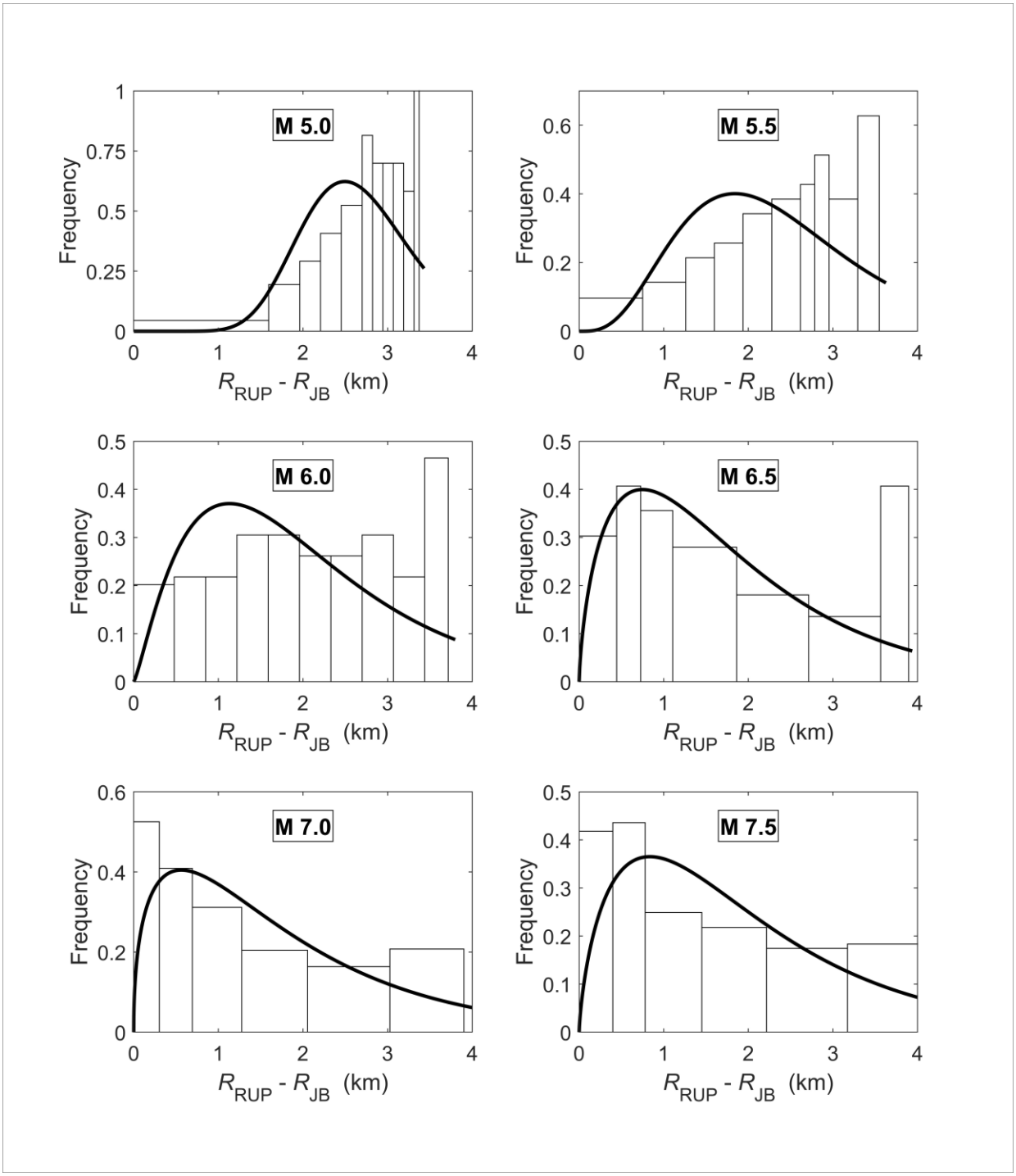

Figure 3.9 Histogram plots of the difference between R_{RUP} and R_{JB} for a vertical strike-slip fault at different magnitudes for a R_{JB} of 10 km. The solid line represents the gamma distribution fitted to the histogram. The mean and the standard deviation of the distribution can be used in regression analysis to determine the coefficients at different M, $R_{JB,}$ and $\boldsymbol{\delta}$ in the empirical equations for R_{RUP}.

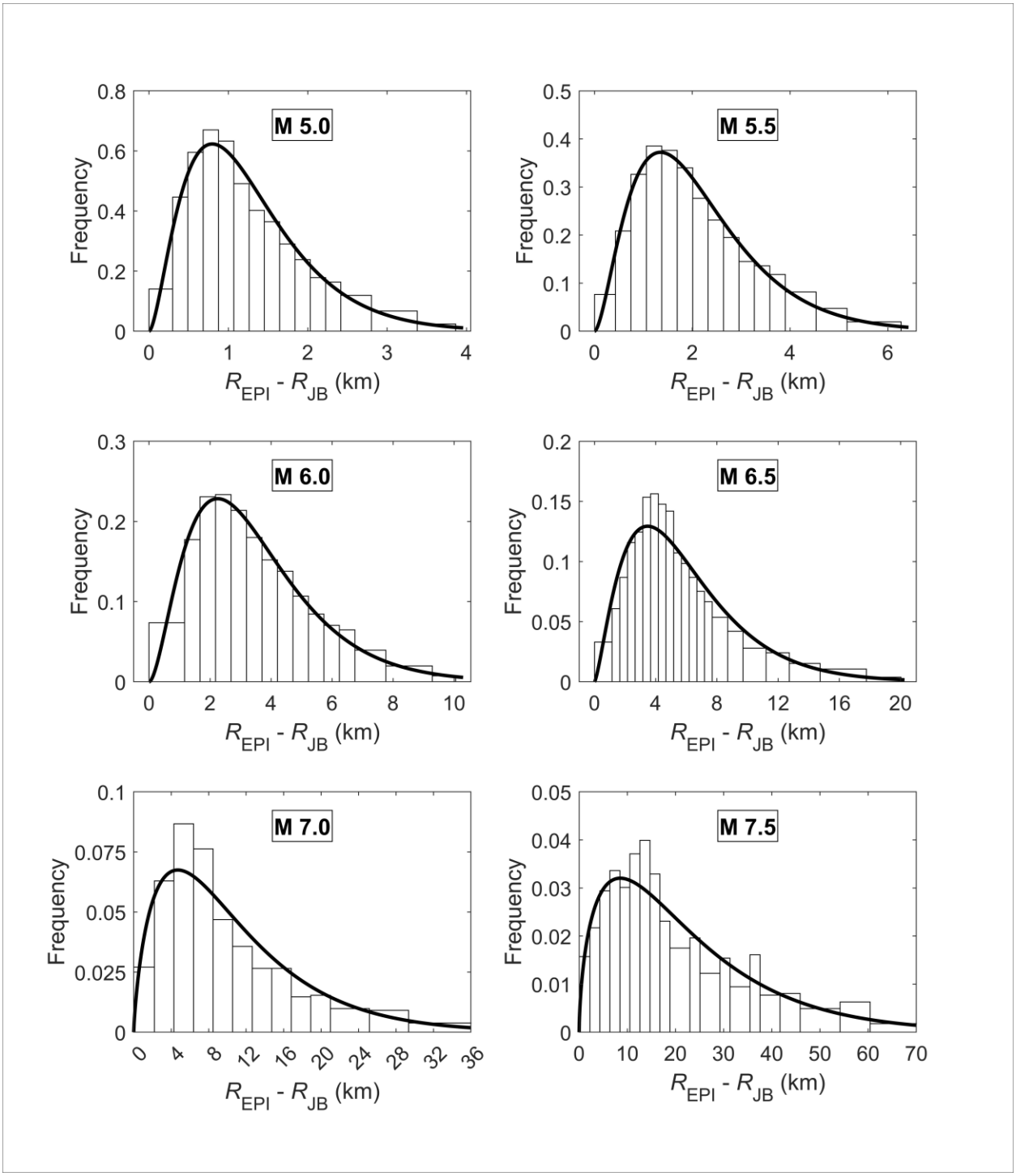

Figure 3.10 Histogram plots of the difference of R_{EPI} and R_{JB} for a dip-slip fault with dip angle **50°** at different magnitudes for a R_{JB} of 10 km. The solid line represents the gamma distribution fitted to the histogram. The mean and the standard deviation of the distribution can be used in regression analysis to determine the coefficients at different M, $R_{JB,}$ and $\boldsymbol{\delta}$ in the empirical equations for R_{EPI}.

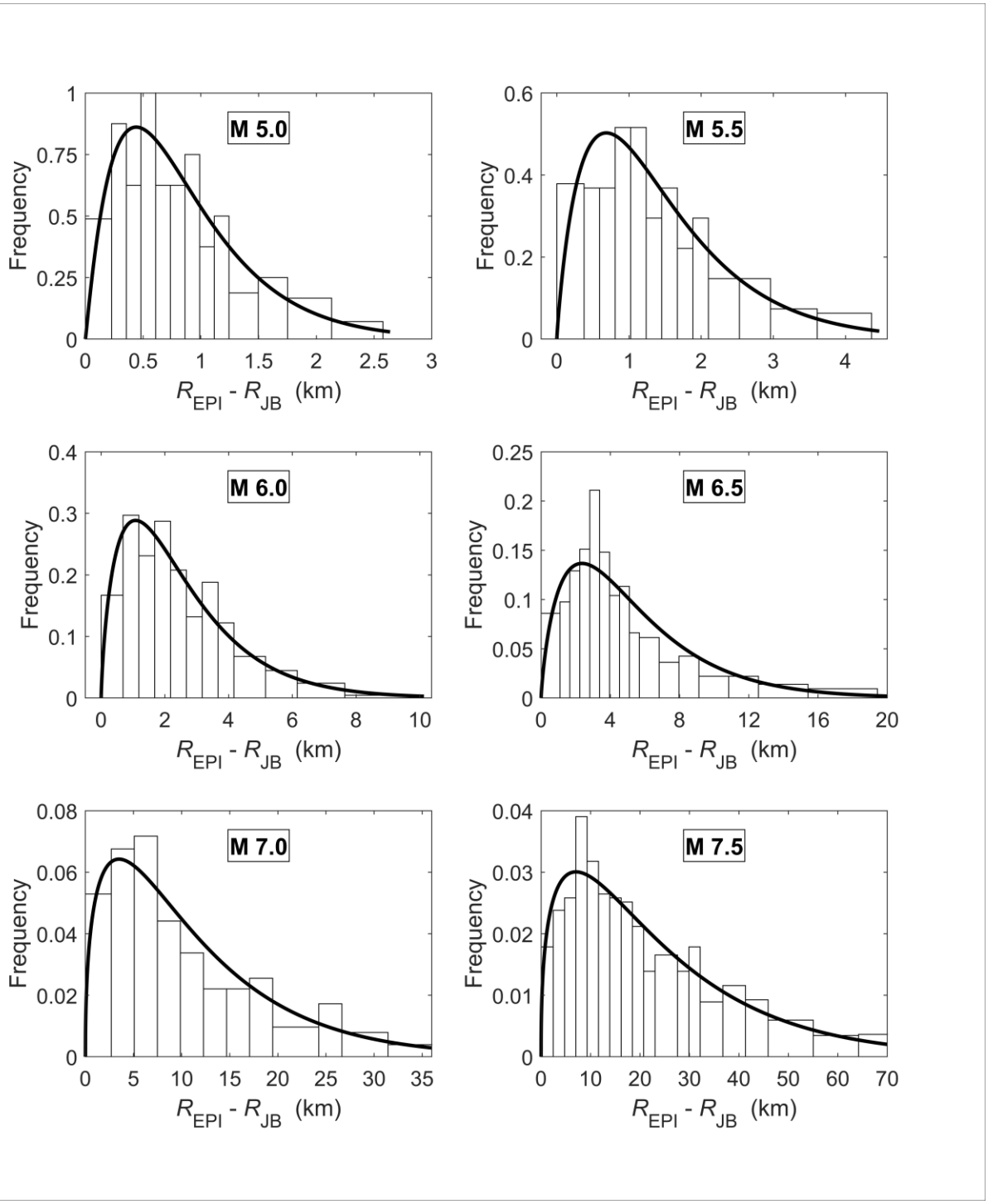

Figure 3.11 Histogram plots of the difference between R_{EPI} and R_{JB} for a vertical strike-slip fault at different magnitudes for a R_{JB} of 10 km. The solid line represents the gamma distribution fitted to the histogram. The mean and the standard deviation of the distribution can be used in regression analysis to determine the coefficients at different M, R_{JB}, and $\boldsymbol{\delta}$ in the empirical equations for R_{EPI}.

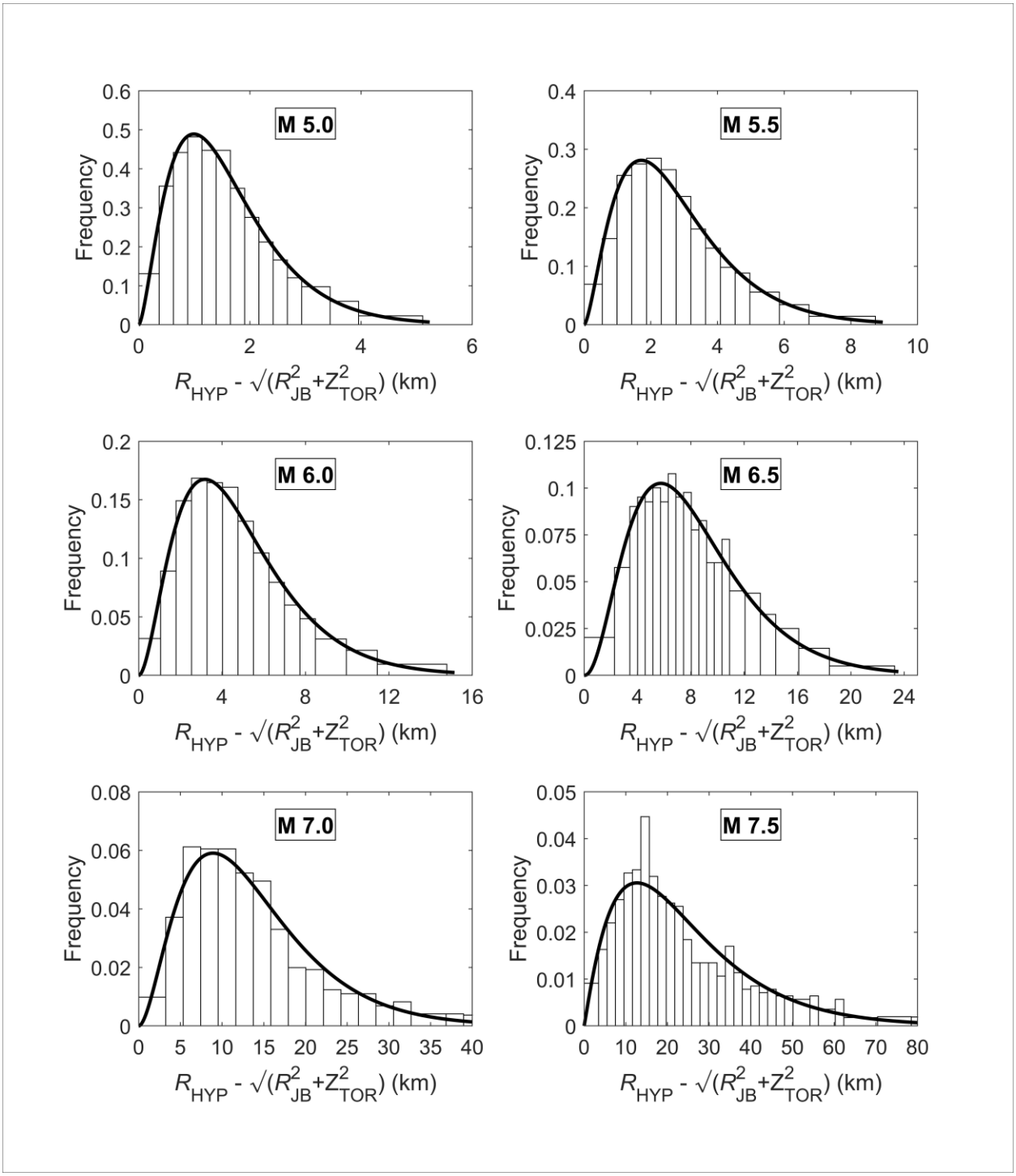

Figure 3.12 Histogram plots of the difference of R_{HYP}, R_{JB}, and Z_{TOR} for a dip-slip fault with dip angle **50°** at different magnitudes for a R_{JB} of 10 km. The solid line represents the gamma distribution fitted to the histogram. The mean and the standard deviation of the distribution can be used in regression analysis to determine the coefficients at different M, $R_{JB,}$ and $\boldsymbol{\delta}$ in the empirical equations for R_{HYP}.

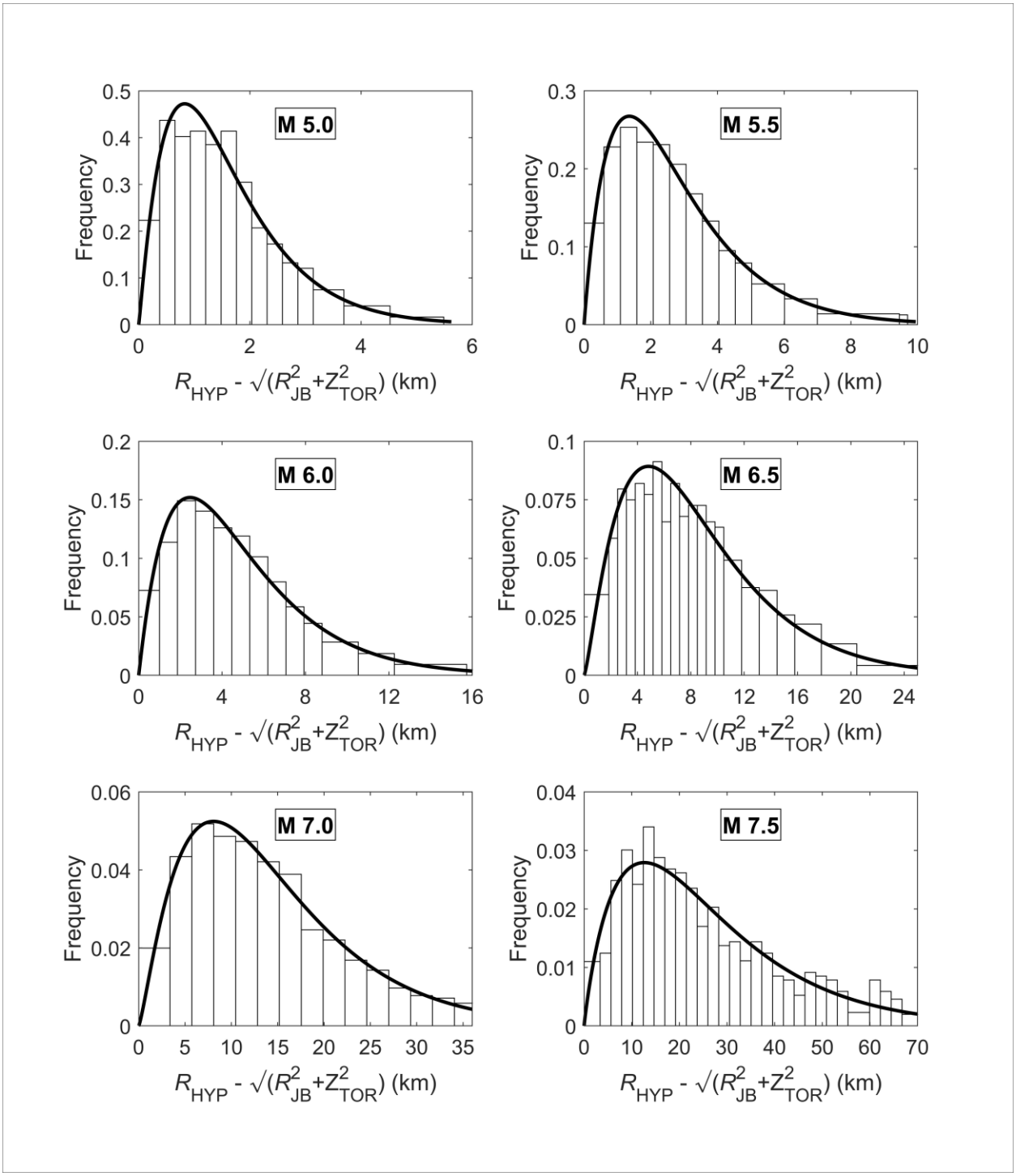

Figure 3.13 Histogram plots of the difference of R_{HYP}, R_{JB}, and Z_{TOR} for a vertical strike-slip fault at different magnitudes for a R_{JB} of 10 km. The solid line represents the gamma distribution fitted to the histogram. The mean and the standard deviation of the distribution can be used in regression analysis to determine the coefficients at different M, $R_{JB,}$ and $\boldsymbol{\delta}$ in the empirical equations for R_{HYP}.

3.4.2 Sensitivity of azimuth angle

The target distance metric varies significantly with the azimuth angle for a given R_{JB}, M, and δ. Boore (2009) determined that the distances parallel to the fault are much larger than the distances perpendicular to the center of the fault for a vertical strike-slip fault at M 5 and M 7. The values converge at larger distances. For sites perpendicular to the center of the fault, the values converged at a distance of 5 km for M 5 and 70 km for the M 7 earthquake event. Similarly, the values converged at 100 km for M 5 and more than 200 km for M 7 if the site is parallel to the fault. In this section, we discuss the variation in estimating the target distance metrics based on the azimuth of the fault using the equations discussed previously.

3.4.2.1 Sensitivity of azimuth angle for Rupture distance

The sensitivity of R_{RUP} with azimuth angle varies significantly based on the magnitude, R_{JB}, and dip angle (Kayastha et al., 2023a). The variation of R_{RUP} with θ for a dip angle of 50° is plotted in Figure 3.14. For smaller magnitudes ($M \leq 5$), R_{RUP} is almost constant at different azimuth angles for a given R_{JB} and dip angle. As the magnitude increases, we can observe significant variation in the calculated R_{RUP} for sites along the footwall (represented by negative azimuth values) and hanging wall (represented by positive azimuth values). The variation is almost abrupt for magnitude 8, as observed by a steep slope between azimuth angles (-3, 3). The variation is also significantly higher at smaller distances (R_{JB} = 1km) and negligible at large distances (R_{JB} = 100 km).

We have also plotted the variation of R_{RUP} with θ for M 7 in Figure 3.15. As the dip angle increases, the maximum value of the ratio of R_{RUP} to R_{JB} decreases. There is no effect of azimuth angle for a

vertical strike-slip fault. For other dip angles, we can observe higher variation at small R_{JB} (R_{JB} = 1 km) and insignificant variation at large distances (R_{JB} = 100 km).

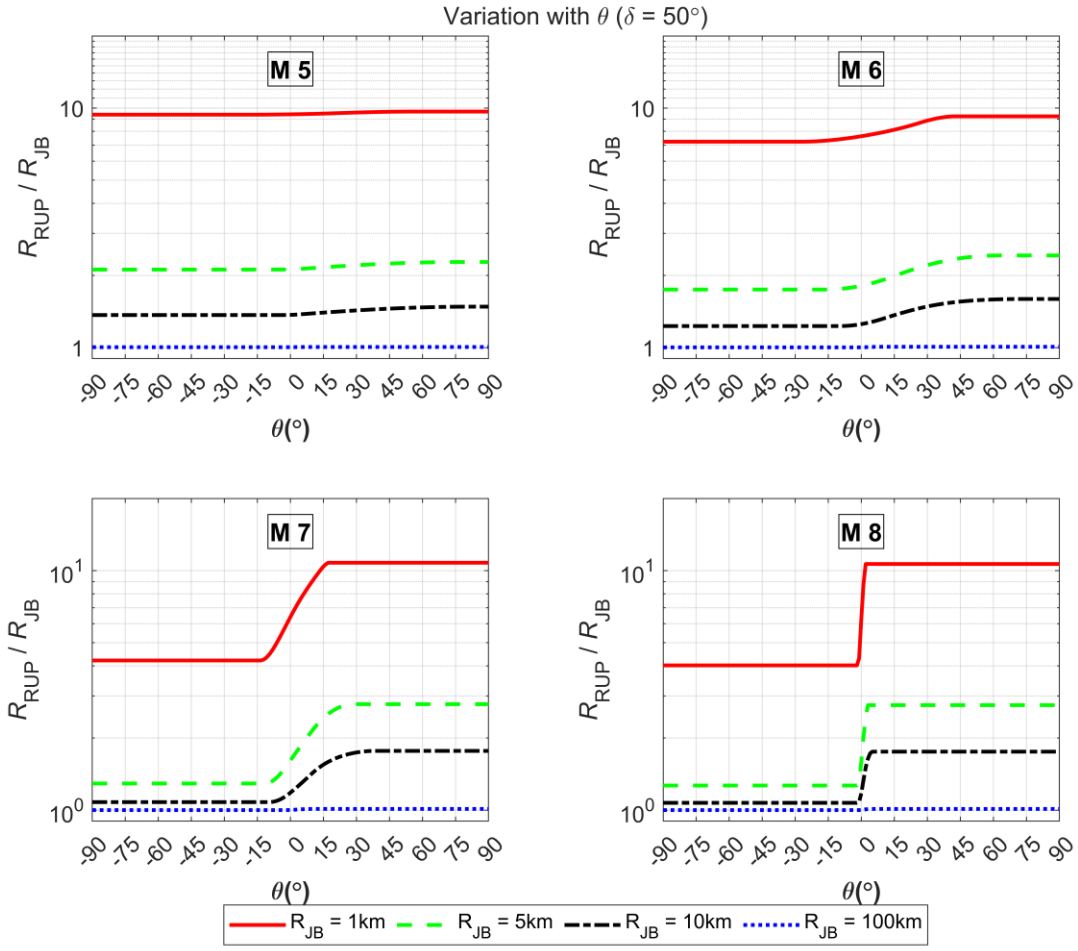

Figure 3.14 Variation of the ratio of R_{RUP} to R_{JB} versus the azimuth angle ($\boldsymbol{\theta}$) at different magnitudes and R_{JB} for a dip-slip fault with dip angle **50°**.

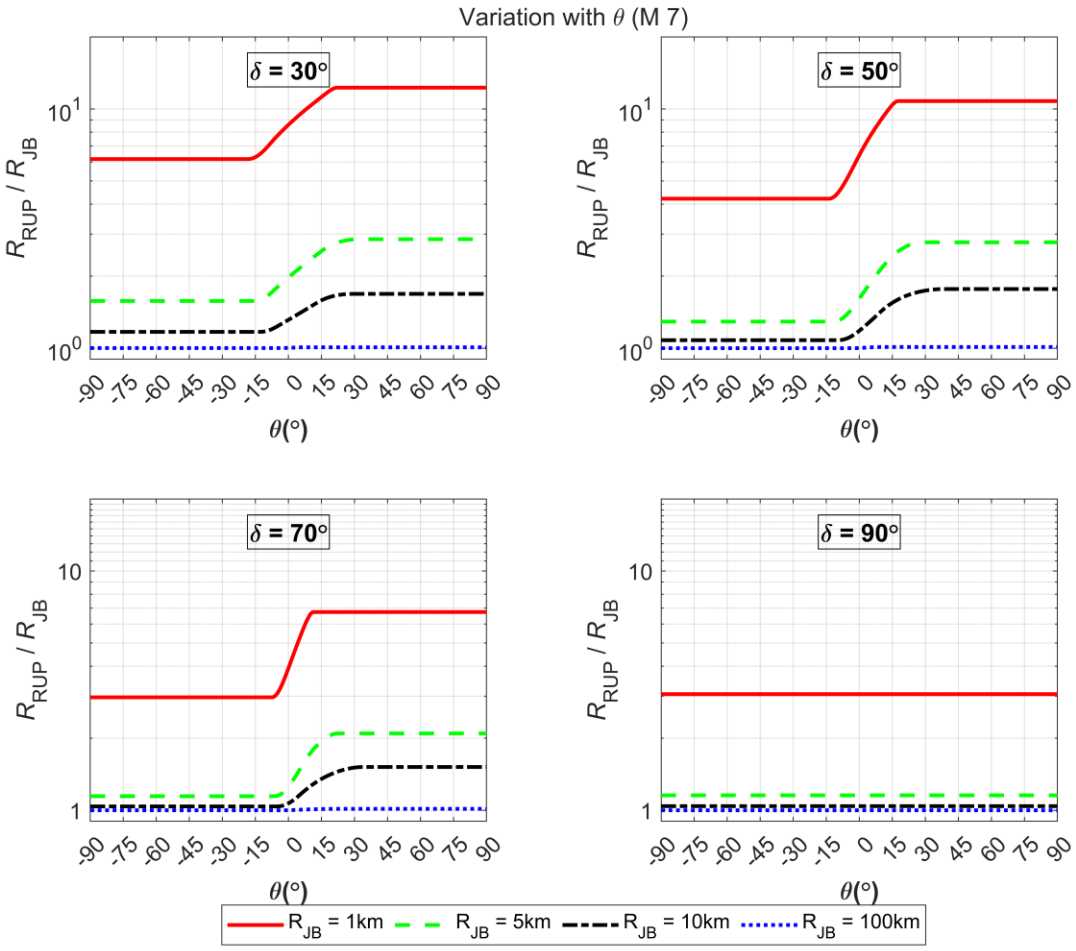

Figure 3.15 Variation of the ratio of R_{RUP} to R_{JB} versus the azimuth angle ($\boldsymbol{\theta}$) at different dip angles and R_{JB} for a M 7 earthquake event.

3.4.2.2 Sensitivity of azimuth angle for Epicentral distance

For the comparison, we have only considered an azimuth angle from 0° to 90° due to symmetry, as discussed in the previous sections. Figure 3.16 shows the variation of the ratio of R_{EPI} to R_{JB} for different magnitudes and R_{JB} for a dip angle of 50°. Similarly, Figure 3.17 shows the variation in the ratio of R_{EPI} to R_{JB} for different dip angles and R_{JB} at M 7. We can observe that the ratio is higher for smaller R_{JB} and decreases as the R_{JB} increases for all magnitudes. This trend strengthens our assumptions that R_{EPI} and R_{JB} vary significantly at smaller distances and that the values are

closer to each other at large distances (Kayastha et al., 2023a). The ratio is also constant at a smaller azimuth angle and decreases exponentially after a hinge point. The hinge point is calculated based on the parameters θ_0 and θ_1 discussed in the previous section. The hinge point is dependent on magnitude; the value of the hinge point decreases as the magnitude increases. As observed in Figure 3.17, the hinge point also depends on the dip angle, with the hinge point decreasing as the dip angle increases. For the vertical strike-slip fault, after the hinge point, we can observe that the ratios are equal for different magnitudes. This can be explained by the equations discussed previously. For $\theta_0 \leq \theta < 90$, $R_{EPI} = \frac{R_{JB}}{\sin(\theta)} \rightarrow \frac{R_{EPI}}{R_{JB}} = \frac{1}{\sin(\theta)}$. Hence, the ratios are dependent only on the azimuth angle beyond the hinge point.

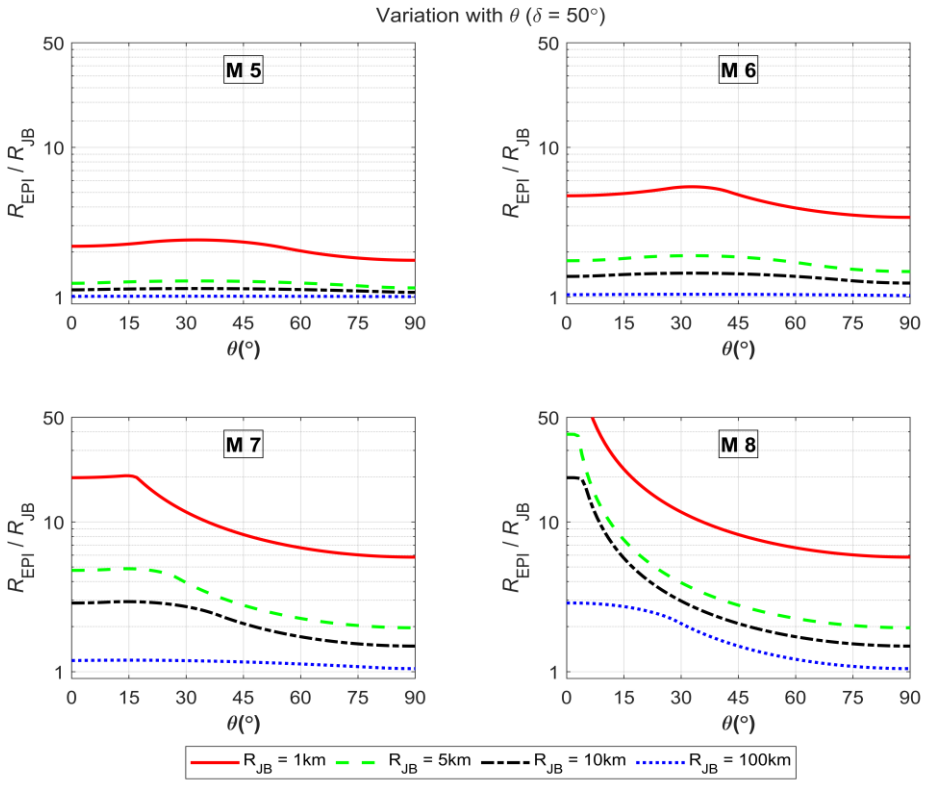

Figure 3.16 Variation of the ratio of R_{EPI} to R_{JB} versus the azimuth angle ($\boldsymbol{\theta}$) at different magnitudes and R_{JB} for a dip-slip fault with dip angle $\mathbf{50°}$.

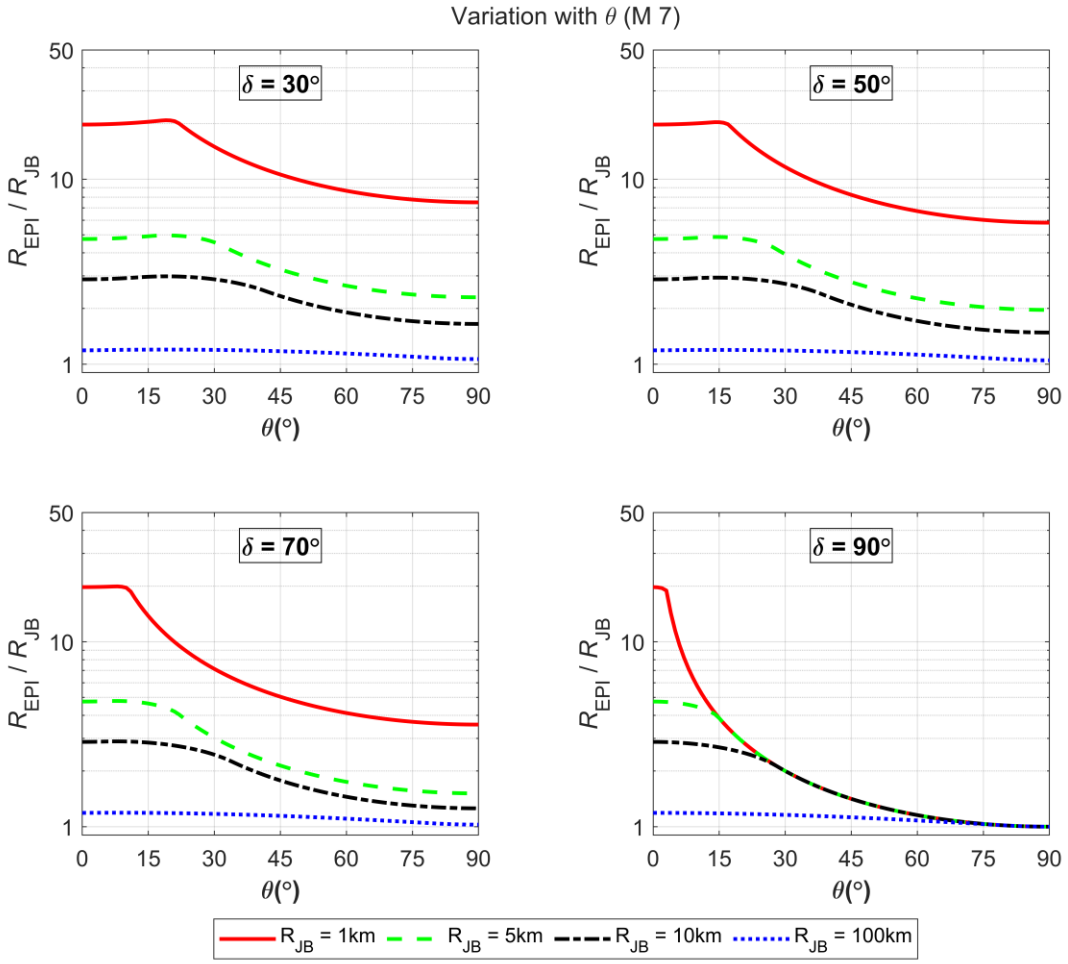

Figure 3.17 Variation of the ratio of R_{EPI} to R_{JB} versus the azimuth angle ($\boldsymbol{\theta}$) at different dip angles and R_{JB} for a M 7 earthquake event.

3.4.2.2 Sensitivity of azimuth angle for Hypocentral distance

Figure 3.18 shows the trend of the ratio of R_{HYP} to R_{JB} for different magnitudes and distances at a dip angle of 50°. The trends for the ratio of R_{HYP} to R_{JB} are similar to the trends observed in the plots for the ratio of R_{EPI} to R_{JB}. The smaller R_{JB} (R_{JB} = 1km) has higher ratios compared to larger R_{JB}. The hinge points are negligible for smaller magnitudes (M<=6).

The variation of the ratio of R_{HYP} to R_{JB} versus azimuth at magnitude 7 for different R_{JB} and dip angles is plotted in Figure 3.19. As the dip angle increase, the hinge value for the azimuth decreases. Unlike the observation in the plot of the ratio of R_{EPI} to R_{JB} versus azimuth for the vertical strike-slip fault, the values beyond the hinge point are not constant for the ratio of R_{HYP} to R_{JB} for the vertical strike-slip fault. The variation is due to the depth term 'z', which significantly affects the values at smaller R_{JB} and is negligible at large distances.

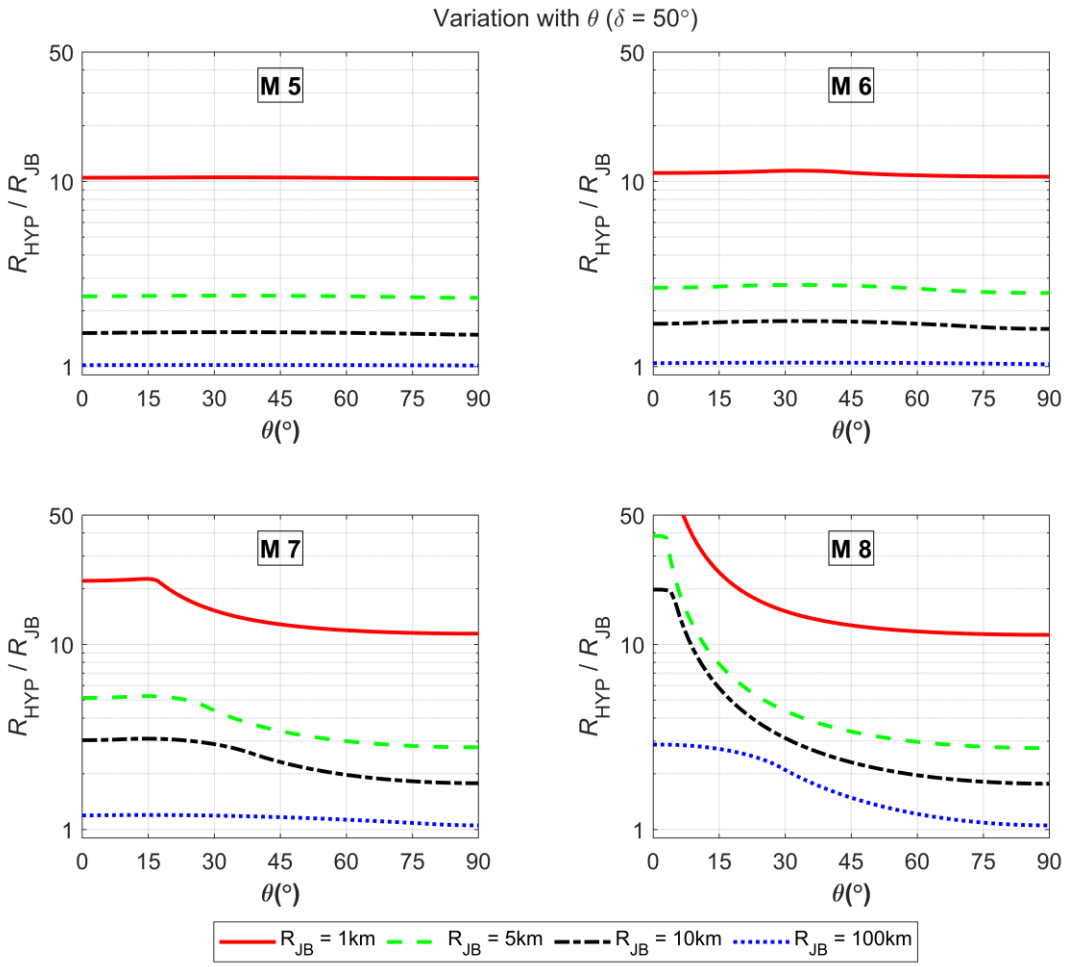

Figure 3.18 Variation of the ratio of R_{HYP} to R_{JB} versus the azimuth angle ($\boldsymbol{\theta}$) at different magnitudes and R_{JB} for a dip-slip fault with dip angle **50°**.

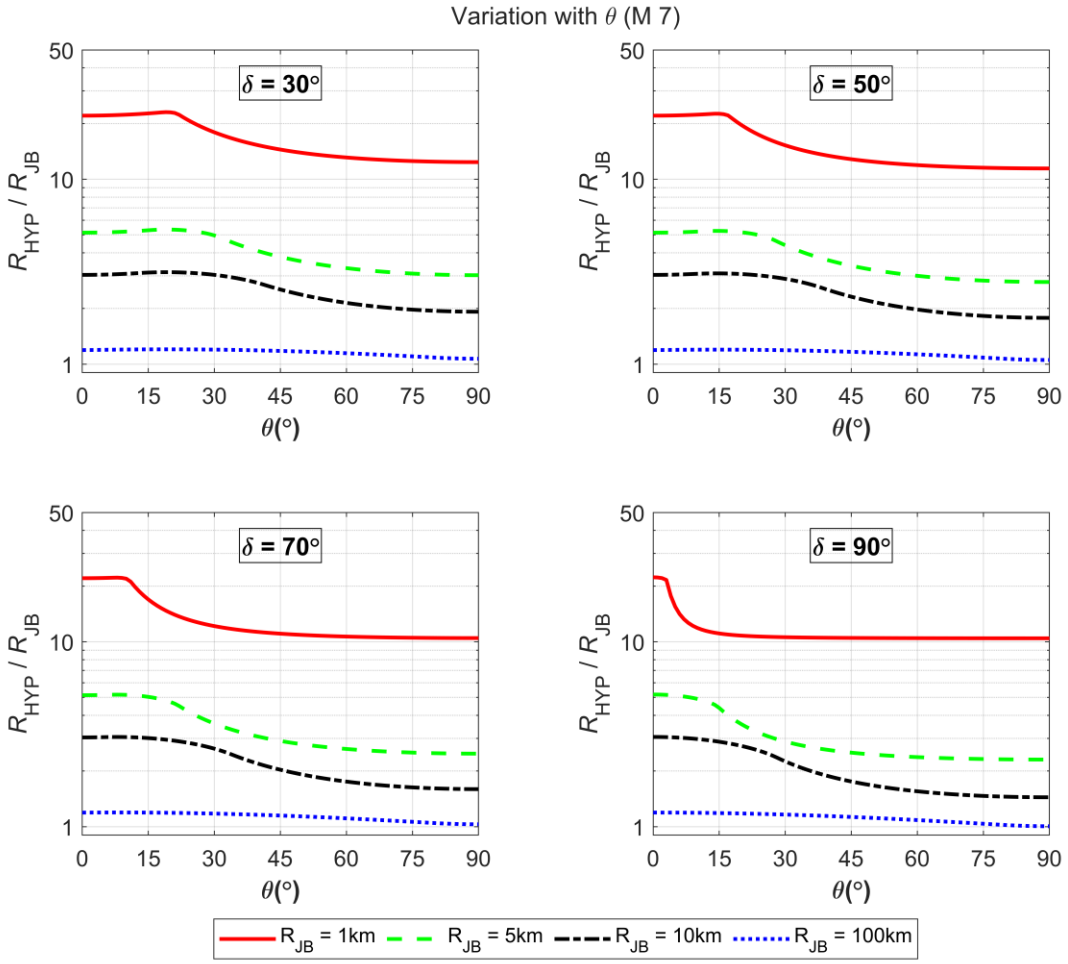

Figure 3.19 Variation of the ratio of R_{HYP} to R_{JB} versus the azimuth angle ($\boldsymbol{\theta}$) at different dip angles and R_{JB} for a M 7 earthquake event.

3.4.3 Saturation effects

In the plots for R_{EPI} and R_{JB} as shown in Figure 3.20, we can observe that for small R_{JB} (R_{JB} = 1km), the R_{EPI} and R_{HYP} values are significantly higher. For M 7 earthquake, for R_{JB} of 1 km, the R_{HYP} value varies from 10 km to 25 km. Such large variations are not observed at large distances (R_{JB} = 100 km). The large variation at close distances is a limitation of point-based distances (Kayastha et al., 2023a). Point-based distances such as R_{EPI} and R_{HYP} assume the total energy of

an earthquake is released from a single point. However, it has been observed that the seismic energy is released from the whole ruptured fault. At large distances, the energy from the sub-faults of the ruptured fault reaches the site of interest with relatively short delays among each other. However, at close distances, only a fraction of the ruptured fault is actually closer to the site of interest. So, the energy from the sub-fault closer to the site reaches it faster than the energy from the furthest sub-fault.

The saturation effects can be modeled in point-based distance models using virtual points, as shown in studies by Atkinson and Silva (2000) and Boore (2009). The virtual point is placed at an effective distance such that the virtual point can mimic the extended fault and release identical total energy to the site.

Mathematically, $R_{EFF} = \sqrt{R^2 + h^2}$, where R_{EFF} is the effective distance, R is the actual point-based distance, and 'h' is the finite fault factor (Tavakoli et al., 2018; Atkinson and Silva, 2000). So, to determine the actual point-based distance, $R = \sqrt{R_{EFF}^2 - h^2}$.

R_{EFF} is the point-based distance that we have calculated using the geometry of the fault. Hence, these values are significantly higher due to the finite fault factor. To determine the actual point-based distances, we need to determine the finite fault factor and remove them from the calculated point-based distances.

For Strike-slip faults,

$$R_C = \begin{cases} \dfrac{R_{JB}}{\sin(\theta)} & \theta_0 \le \theta < 90 \\ \sqrt{\left(\dfrac{L}{2}\right)^2 + R_{JB}^2 - 2 * \left(\dfrac{L}{2}\right) * R_{JB} * \cos\left(180 - \left[\theta + \sin^{-1}\left(\dfrac{\sin(\theta) * \dfrac{L}{2}}{R_{JB}}\right)\right]\right)} & 0 \le \theta < \theta_0 \end{cases} \quad (3.32)$$

$$< R_{EPI} >_\theta = \int_{-\frac{l}{2}}^{\frac{l}{2}} \sqrt{R_C^2 + x^2 - 2xR_C\cos(\theta)}\ p(x)dx \quad (3.33)$$

When the site lies on top of the fault, R_{JB} and R_{EPI} are 0. However, R_{EPI} calculated based on the equation derived based on the geometry of the fault discussed previously is not zero. The resultant value provides us with the finite-fault factor.

$$R_{JB} = R_{EPI} = 0$$

$$\Rightarrow R_C = \frac{L}{2}$$

$$\Rightarrow h = < R_{EPI} >_\theta$$

For an azimuth angle $\theta = 0°$,

$$h = \int_{-\frac{l}{2}}^{\frac{l}{2}} \sqrt{\left(\frac{L}{2}\right)^2 + x^2 - 2 * x * \frac{1}{L} * \cos(0)}\ p(x)dx$$

Assuming a uniform distribution of the epicenter along the fault, $p(x) = 1/L$

Also,$\cos(0) = 1$, so

$$h = \int_{-\frac{l}{2}}^{\frac{l}{2}} \sqrt{\left(\frac{L}{2}\right)^2 + x^2 - 2 * x * \left(\frac{L}{2}\right)} * \frac{1}{L} * dx$$

$$h = \int_{-\frac{l}{2}}^{\frac{l}{2}} \sqrt{\left(\frac{L}{2} - x\right)^2} * \frac{1}{L} * dx$$

$$h = \int_{-\frac{l}{2}}^{\frac{l}{2}} \left(\frac{L}{2} - x\right) * \frac{1}{L} * dx$$

$$h = \int_{-\frac{l}{2}}^{\frac{l}{2}} \left(\frac{1}{2} - \frac{x}{L}\right) * dx$$

$$h = \frac{1}{2} * \left[\frac{L}{2} + \frac{L}{2}\right] - \frac{1}{L} * \left[\frac{L^2}{8} - \frac{L^2}{8}\right]$$

$$h = \frac{L}{2} \tag{3.34}$$

So, the value of 'h' for a strike-slip fault is equal to half the length of the fault. This is valid only when $\theta = 0°$, i.e., when the site lies at the end of the fault (since 'θ' is used to represent the location of the site about the fault). For values other than $\theta = 0°$, the value for 'h' differs. The finite-fault factor (h) for different azimuth angles for vertical strike-slip faults and dip-slip faults can be calculated numerically by using the equations for $< R_{EPI} >_\theta$ assuming a very small value of R_{JB} (R_{JB} = 0.0000001 km). This assumption does not affect the resultant calculated finite-fault factor, as shown in Table 3.2.

Table 3.2 Comparison of the finite-fault factor obtained numerically (h_{calc}) with equation (3.34) for different magnitudes at a site located parallel to the ruptured fault ($\boldsymbol{\theta} = \mathbf{0}°$).

Magnitude	Length (km)	h_{calc} (km)	$h = 0.5 * L$ (km)
5.00	2.37	1.19	1.19
5.50	4.22	2.11	2.11
6.00	7.50	3.75	3.75
6.50	13.34	6.67	6.67
7.00	37.49	18.74	18.74
7.50	118.55	59.28	59.28
8.00	374.89	187.45	187.45

For dip-slip faults,

$$R_C = \begin{cases} \dfrac{R_{JB} + \dfrac{L}{2}}{\cos(\theta')} & 0 \le \theta < \theta_1 \\ \sqrt{R_{JB}^2 + y^2 + \left(\dfrac{L}{2}\right)^2 - 2\sqrt{y^2 + \left(\dfrac{L}{2}\right)^2}\, R_{JB}\cos(\gamma)} & \theta_1 \le \theta < \theta_0 \\ \dfrac{y + R_{JB}}{\sin(\theta')} & \theta_0 \le \theta < 90 \end{cases} \quad (3.35)$$

When $R_{JB} \xrightarrow{lim} 0$,

$$\theta_0 = \tan^{-1}\left[\frac{\frac{Wcos(\delta)}{2} + R_{JB}}{\frac{L}{2}}\right] = \tan^{-1}\left[\frac{\frac{Wcos(\delta)}{2}}{\frac{L}{2}}\right] = \tan^{-1}\left[\frac{Wcos(\delta)}{L}\right]$$

$$\theta_1 = \tan^{-1}\left[\frac{\frac{Wcos(\delta)}{2}}{\frac{L}{2} + R_{JB}}\right] = \tan^{-1}\left[\frac{\frac{Wcos(\delta)}{2}}{\frac{L}{2}}\right] = \tan^{-1}\left[\frac{Wcos(\delta)}{L}\right]$$

$$\theta_p = \theta_0 = \theta_1 = \tan^{-1}\left[\frac{Wcos(\delta)}{L}\right]$$

$$R_C = \begin{cases} \dfrac{\frac{L}{2}}{\cos(\theta')} & 0 \le \theta < \theta_p \\ \dfrac{y}{\sin(\theta')} & \theta_p \le \theta < 90 \end{cases}$$

$$< R_{EPI} >_\theta = \int_0^{W\cos(\delta)} \int_{-\frac{l}{2}}^{\frac{l}{2}} \sqrt{R_C^2 + x^2 - 2xR_C\cos(\theta)}\; p(x)p(y)dxdy$$

$$h = \int_0^{W\cos(\delta)} \int_{-\frac{l}{2}}^{\frac{l}{2}} \sqrt{R_C^2 + x^2 - 2xR_C\cos(\theta)}\; p(x)p(y)dxdy \qquad (3.36)$$

Figure 3.20 shows the variation of the ratio of the finite fault factor to the length of the fault versus θ for different dip angles and magnitudes at R_{JB} = 1 km. As discussed previously, the hinge point is based on θ_0 and θ_1. When R_{JB} = 0, $\theta_p = \theta_0 = \theta_1$, as discussed previously. The value of θ_p depends on the dimensions of the fault and the dip angle. For our calculation, we have chosen the aspect ratio as 1 $\left(\frac{L}{W} = 1\right)$. As a result, the θ_p value for M 5 and M 6 is the same and the ratio of 'h/L' is similar. However, the calculated fault dimensions may fall over the surface at larger magnitudes. When we fix the top of the fault on the surface for such cases, we need to recalculate the fault dimensions keeping the rupture area constant, resulting in a change in the value of the aspect ratio. For larger magnitudes, the 'h/L' value is similar up to θ_p and decreases beyond the hinge point as the magnitude increases. The 'h/L' value is constant for the vertical strike-slip fault for all magnitudes. It is 0.5 at $\theta = 0°$, and zero elsewhere.

Using the finite-fault factor, we can calculate the R_{EPI} and R_{HYP} values used to determine the empirical equations discussed in the next chapter.

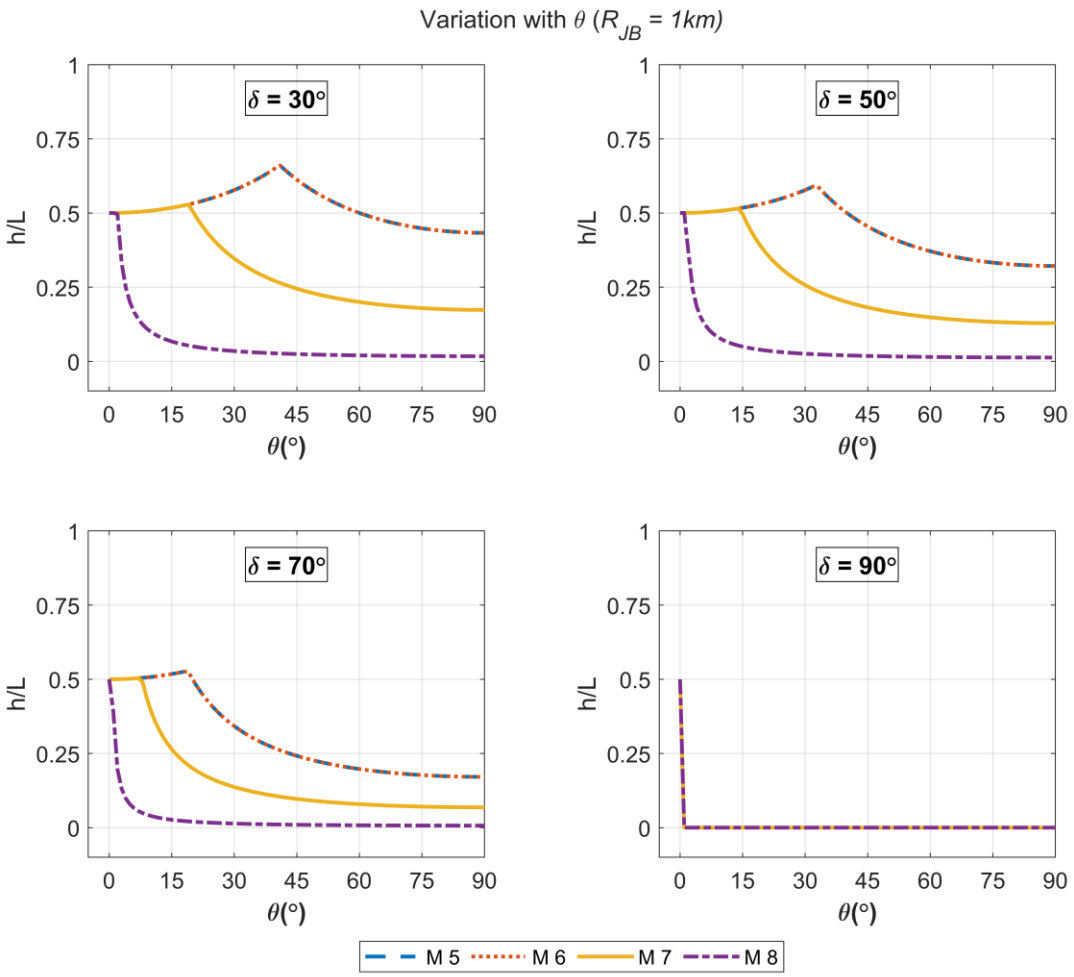

Figure 3.20 Variation of the ratio of the finite fault factor (h) to the length of the fault versus the azimuth angle ($\boldsymbol{\theta}$) at a R_{JB} of 1 km for different magnitudes and dip angles.

3.4.4 Effect of aspect ratio

As discussed in the previous sections, we used an aspect ratio (the ratio of length to width) of 1 for the calculations. Different published studies have used different aspect ratios to determine the dimensions of the fault based on the ruptured area. EPRI (2004) used an aspect ratio of 3 for a strike-slip fault and an aspect ratio of 2 for a dip-slip fault. Thompson and Worden (2018) used an aspect ratio of 1.7 for the active continental region and 1.0 for the stable continental region. In this section, we examine the impact of aspect ratio in estimating distance metrics.

For smaller earthquakes (M≤6), the dimensions of the ruptured fault based on magnitude is also small, so there is not a significant variation between the estimated distance metrics using different aspect ratios, as shown in Figure 3.21 for the ratio of R_{RUP} to R_{JB} versus R_{JB} for different magnitudes for a dip-slip fault with a dip angle of 50°. There is a slight variation for a vertical strike-slip fault for M 6 that is not observed for dip-slip faults, as seen in Figure 3.22. As we have shown in the equations to calculate the distance metrics, the length and the width of the ruptured fault are essential parameters for the dip-slip fault. However, for the strike-slip fault, only the length of the fault is used to estimate the distance metrics. As a result, the variation in length due to different aspect ratios causes a slight variation in the estimated distance metrics for the strike-slip fault, while the impact is not felt for the dip-slip fault. The variation is observed at small R_{JB} ($R_{JB} \leq 20$ km). The estimated distance is the smallest for AR 1.0 and the highest for AR 3.0. Similar observations can be made for the effects of the aspect ratio on R_{EPI} for different magnitudes and dip angles, as shown in Figure 3.23 and Figure 3.24, respectively. Figure 3.25 and Figure 3.26 show the variation of the ratio of R_{HYP} to R_{JB} versus R_{JB} at different aspect ratios for different magnitudes and dip angles, respectively.

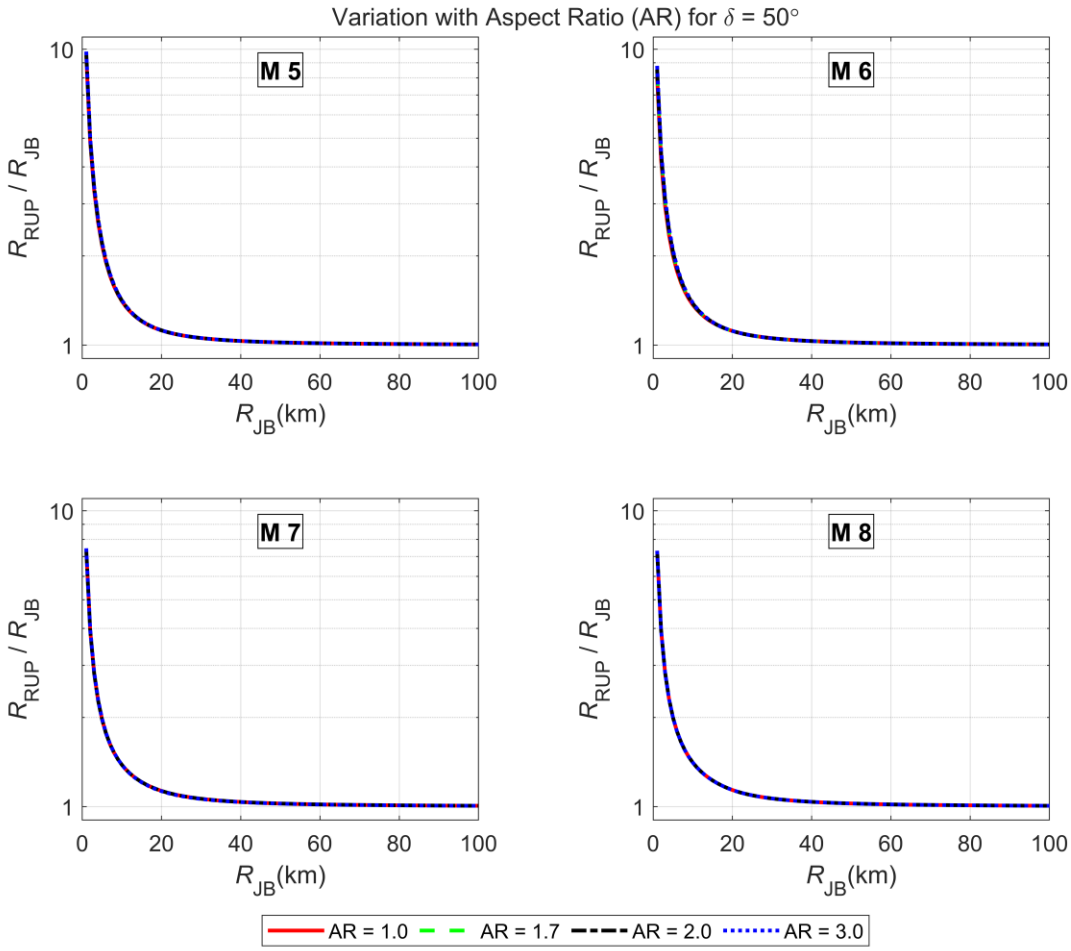

Figure 3.21 Variation of the ratio of R_{RUP} to R_{JB} versus R_{JB} for different magnitudes and aspect ratios (AR) for a dip-slip fault with a dip angle of 50°.

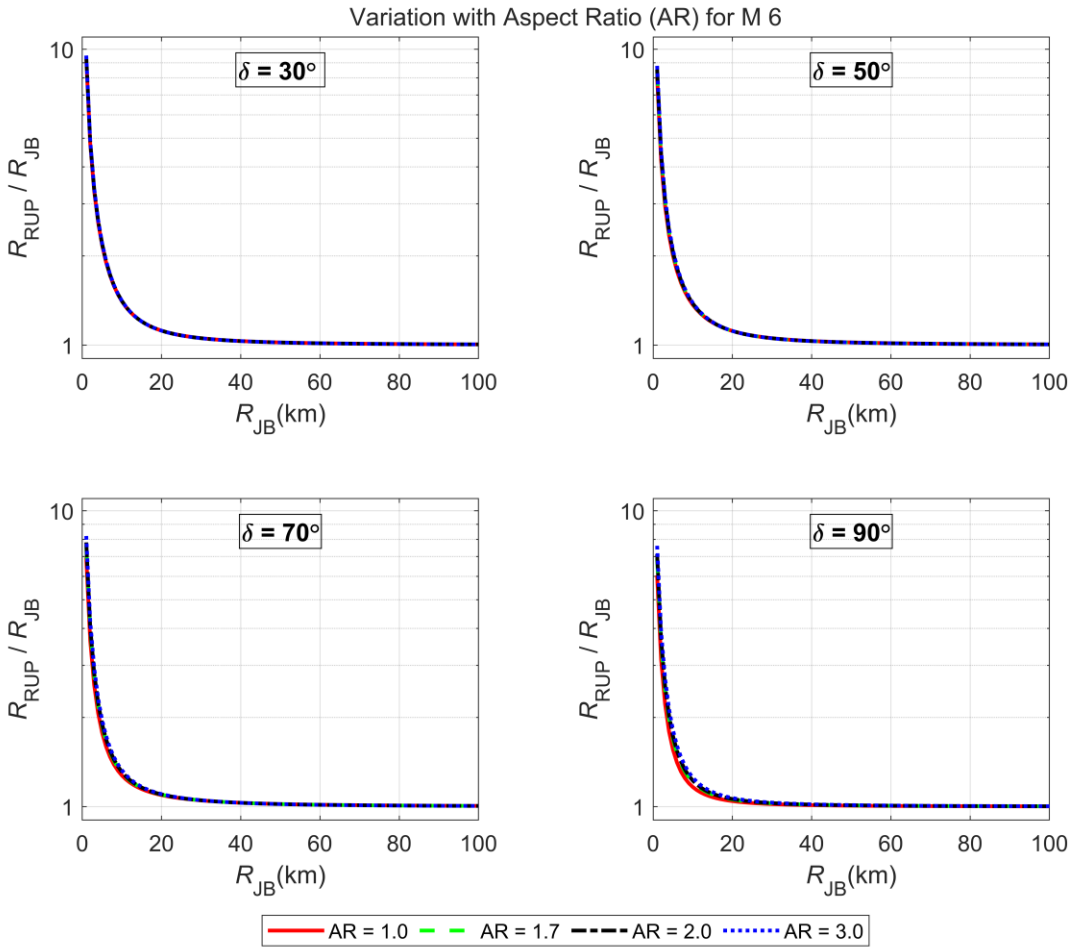

Figure 3.22 Variation of the ratio of R_{RUP} to R_{JB} versus R_{JB} for different dip angles and aspect ratios (AR) for a M 6 earthquake event.

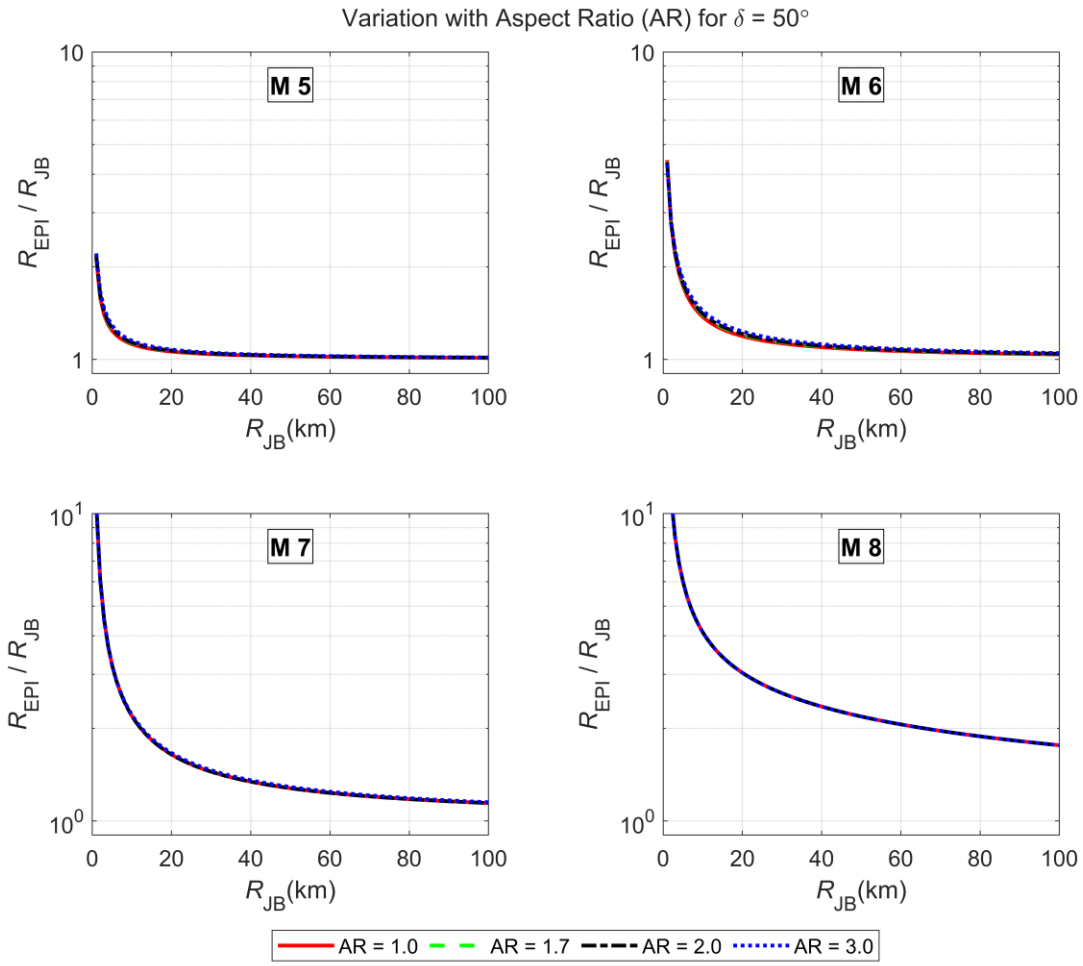

Figure 3.23 Variation of the ratio of R_{EPI} to R_{JB} versus R_{JB} for different magnitudes and aspect ratios (AR) for a dip-slip fault with a dip angle of 50°.

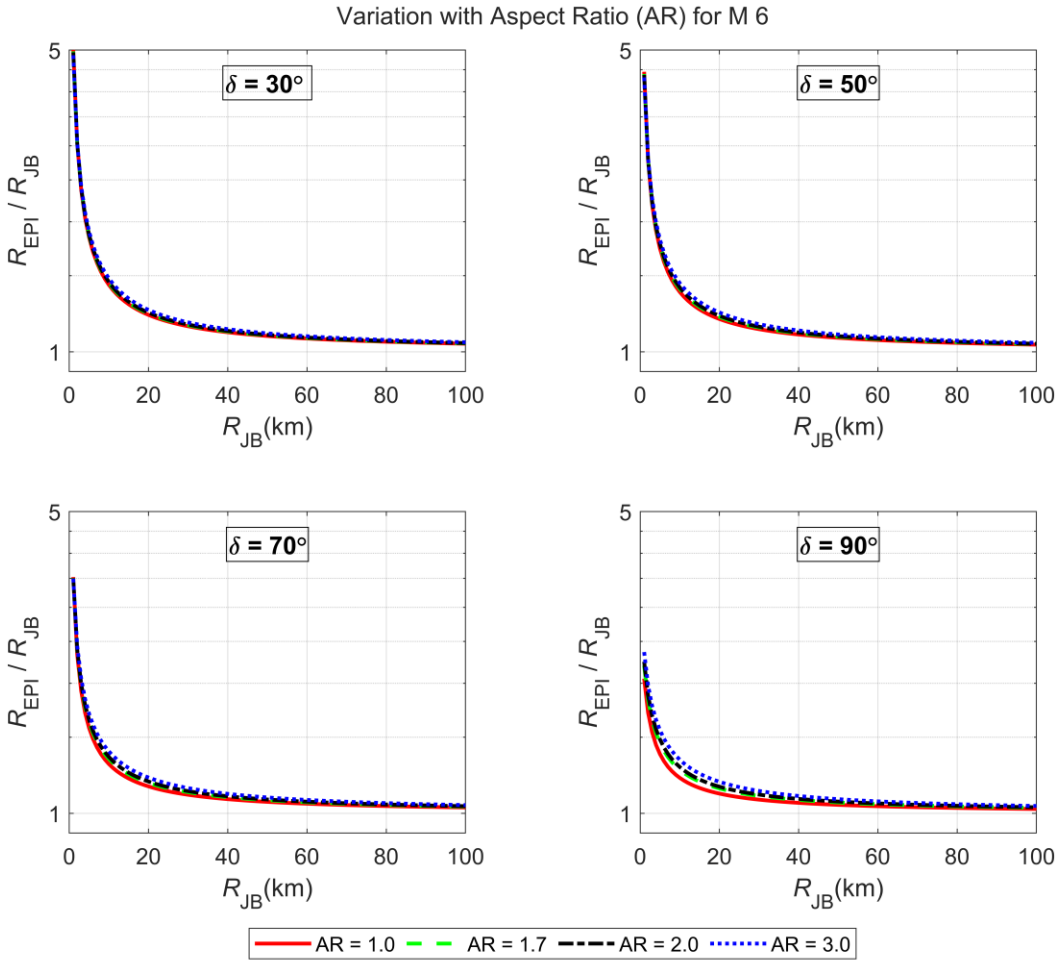

Figure 3.24 Variation of the ratio of R_{EPI} to R_{JB} versus R_{JB} for different dip angles and aspect ratios (AR) for a M 6 earthquake event.

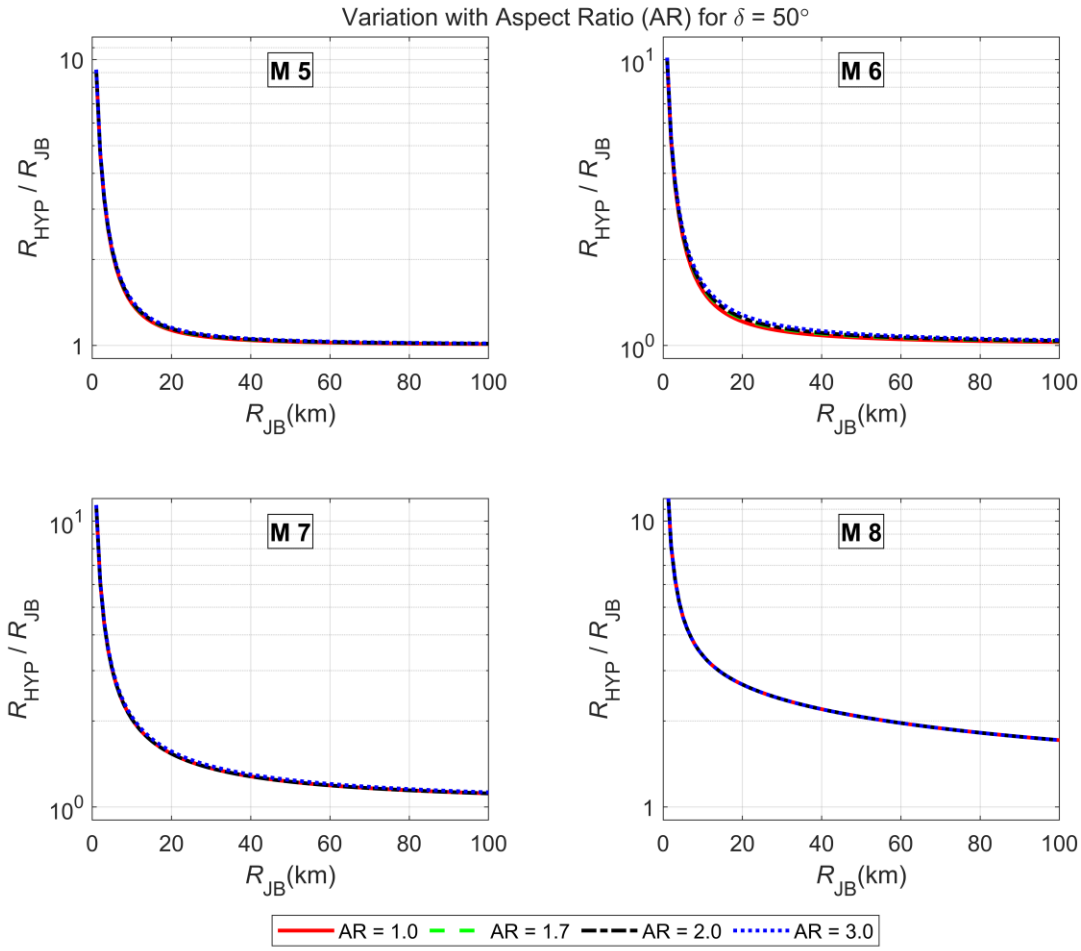

Figure 3.25 Variation of the ratio of R_{HYP} to R_{JB} versus R_{JB} for different magnitudes and aspect ratios (AR) for a dip-slip fault with a dip angle of 50°.

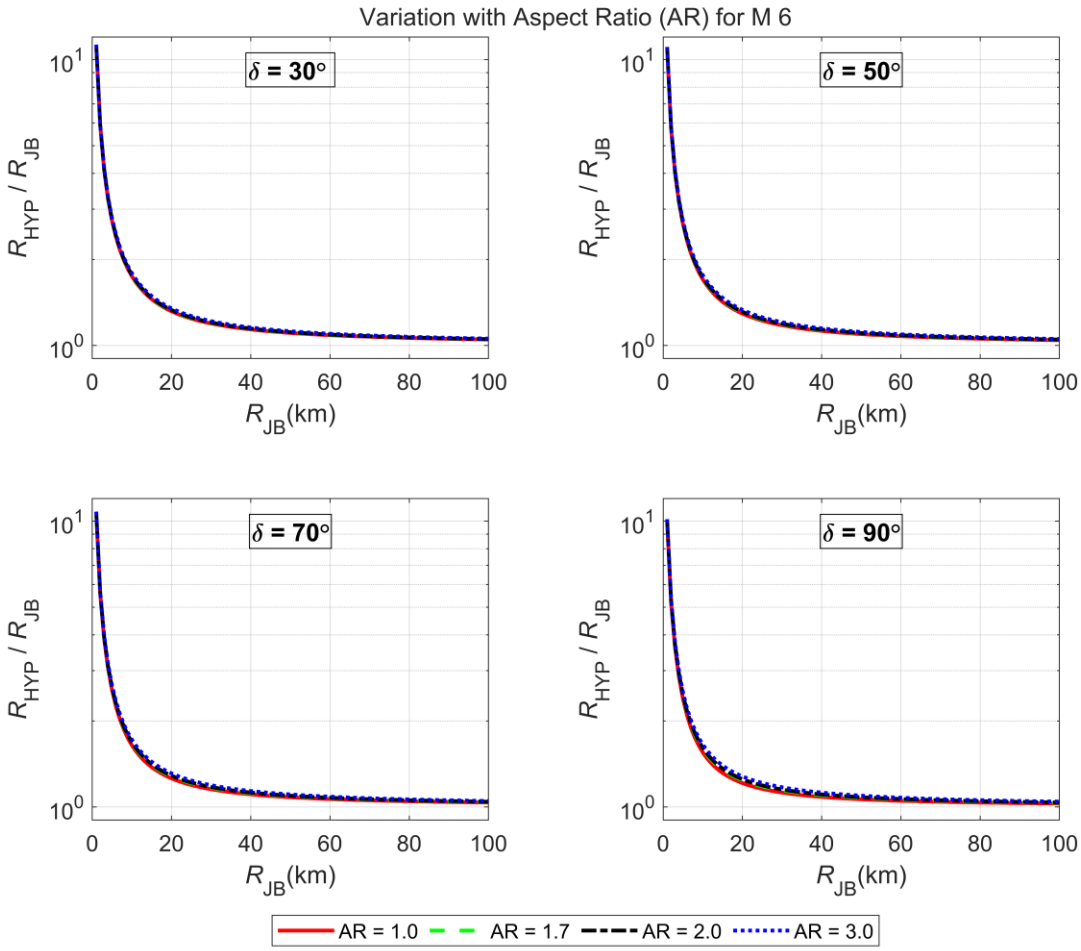

Figure 3.26 Variation of the ratio of R_{HYP} to R_{JB} versus R_{JB} for different dip angles and aspect ratios (AR) for a M 6 earthquake event.

The variations are not observed for large-magnitude earthquakes for either dip-slip or vertical strike-slip faults (Kayastha et al., 2023a). We have restricted the depth of the fault to the seismogenic depth (15 km). The calculated depth using Scherbaum et al. (2004) for larger magnitudes is usually higher than the seismogenic depth. Due to this restriction, we need to recalculate the width of the fault based on the restricted depth and then calculated the length of the fault while keeping the ruptured area constant. So, for higher magnitude earthquakes, the aspect ratio is not maintained to satisfy the conditions for the depth of the fault. So, the aspect ratio only

affects smaller magnitude earthquakes for the vertical strike-slip fault. This variation is also not very significant. Thompson and Worden (2018) also determined that the calculated distances are identical when they compared the results for a range of AR observed in the NGA-West2 database for the active continental region (AR varying from 0.75 to 4.75) with the assumed AR of 1.7 that they used for their studies.

3.5 Chapter Conclusion

In this chapter, we discussed the equations for different distance metrics based on the geometry of the fault. The geometry of the fault is dependent on the magnitude of the earthquake, the dip angle of the fault, and the depth to the top of the rupture. The fault dimensions are determined based on the magnitude using Somerville (2014). We can either specify the depth to the top of the rupture or use the magnitude to determine the depth to the top of the rupture using Scherbaum et al. (2004). For our calculations, we have used Scherbaum et al. (2004) to determine the hypocentral depth. The hypocentral depth and the width of the ruptured fault are then used to determine the depth to the top of the rupture. We have provided the equations for fault-based distance metrics R_X, R_Y, and R_{RUP} and point-based distance metrics R_{EPI} and R_{HYP}. For point-based distance metrics, the fault is discretized, and the location of the hypocenter is randomized across the fault based on Mai et al. (2005). We have used a virtual site model to model the fault and the site where the fault is constant, and the site moves along the fault at a fixed distance. Based on the azimuth angle from the fault to the site, the estimated distance also changes significantly. The effect of azimuth angle is less pronounced for smaller magnitudes ($M \leq 6$) and at larger distances ($R_{JB} \geq 100\ km$). This effect is also not observed in the case of R_{RUP} for a vertical strike-slip fault. We have also discussed

the saturation effects, which can be observed for larger magnitudes and at small distances. The effect of aspect ratio was determined to be not significant in the estimation of distance metrics.

Chapter 4 Mean Models for distance metrics conversions

4.1 Introduction

We conducted a non-linear least squares regression analysis for the data to develop a suitable empirical relation between R_{JB} and the target distance. For regression, we used the mean value of the target distances at different azimuths for a given R_{JB}. To determine the correlation between the target distance metric and R_{JB}, we choose an appropriate functional form that best describes their relationship. The functional form is dependent on the M, Z_{TOR}, and δ of the fault and can be presented as

$$R_{target} = f(R_{JB}, M, \delta, Z_{TOR}) + \sigma \quad (4.1)$$

where σ is the standard deviation due to variations in different parameters such as the location of the hypocenter, azimuth, and geometry of the fault. Separate equations have been presented for dip-slip faults and vertical strike-slip faults. For the vertical strike-slip faults, the width of the fault does not impact the calculation of the target distance, but the width of the fault is an essential parameter for the dip-slip fault. Due to this, the final values obtained for both cases are different from each other and are better represented if we conduct separate regressions on these datasets. Though azimuth angles are an important parameter to accurately determine the target distance metrics, we have not included it as a dependent variable. Instead, we have calculated the mean target distance across all azimuth angles. For cases with more information, such as the location of the hypocenter or azimuth, Approach-3 discussed in section 2.2.3, where each possible source-site scenario is simulated, would provide better results than the proposed empirical equations. The proposed empirical equations would only provide mean values considering random azimuth and hypocenter locations.

4.1.1 Joyner-Boore distance and Rupture distance

Based on equation (3.16), we determine the mean R_{RUP} for a given R_{JB} at different lengths, widths, and dip angles of the fault. Due to symmetry, only azimuth angles from $-90°$ to $90°$ are used for calculation. Separate regression analysis was carried out for vertical strike-slip faults and dip-slip faults. At different dip angles, the coefficients for the dip-slip faults are different. The relationship between R_{JB} and R_{RUP} for dip-slip faults can be represented as:

$$\begin{gathered} E[R_{RUP}|R_{JB}, M, \delta] = R_{JB} + C_1 \exp(-C_2(M-5)) \exp\left(-C_3 R_{JB}\right) + C_4 \exp\left(-C_5 R_{JB}\right) \pm CF_{HW} + \sigma_{RUP} \\ CF_{HW} = C_6 \exp\left(C_7(M-5)\right) \exp\left(-C_8 R_{JB}\right) \end{gathered} \tag{4.2}$$

where parameters C_1 to C_8 are the regression coefficients, and CF_{HW} is the hanging wall and footwall parameter. Coefficients C_1 to C_8 are obtained from regression analysis and are provided in Table 4.1. The coefficients for dip angles not listed can be determined using interpolation. σ_{RUP} is the standard deviation discussed in the next section. The CF_{HW} term is positive on the hanging wall side of the fault and negative on the footwall side of the fault. If the location of the site about the fault is not known, $CF_{HW} = 0$. The effect of the CF_{HW} term is discussed in later sections.

For a vertical strike-slip fault,

$$E[R_{RUP}|R_{JB}, M, \delta] = R_{JB} + C_1 \exp(-C_2(M-5)^2) \exp\left(-C_3 R_{JB}\right) + C_4 \exp\left(-C_5 R_{JB}\right) + \sigma_{RUP} \tag{4.3}$$

The effect of the footwall and hanging wall is not observed for a vertical strike-slip fault. As a result, the CF_{HW} term is zero and not included in equation (4.3). As shown in Figure 4.1, the values obtained from the empirical equation (represented as lines) closely align with the mean data obtained from the equation (represented by dots). For this comparison, the CF_{HW} term is not included for all dip angles. R_{RUP} is considerably larger than R_{JB} at shorter distances (<10 km), but the values converge at larger R_{JB} (>30 km). R_{RUP} varies with the dip angle of the fault and the

magnitude of the earthquake event, though the variation is mainly observed below 20 km. At smaller distances, we observe that R_{RUP} decreases as the magnitude increases, though this effect is not observed for smaller dip angles (δ=30°).

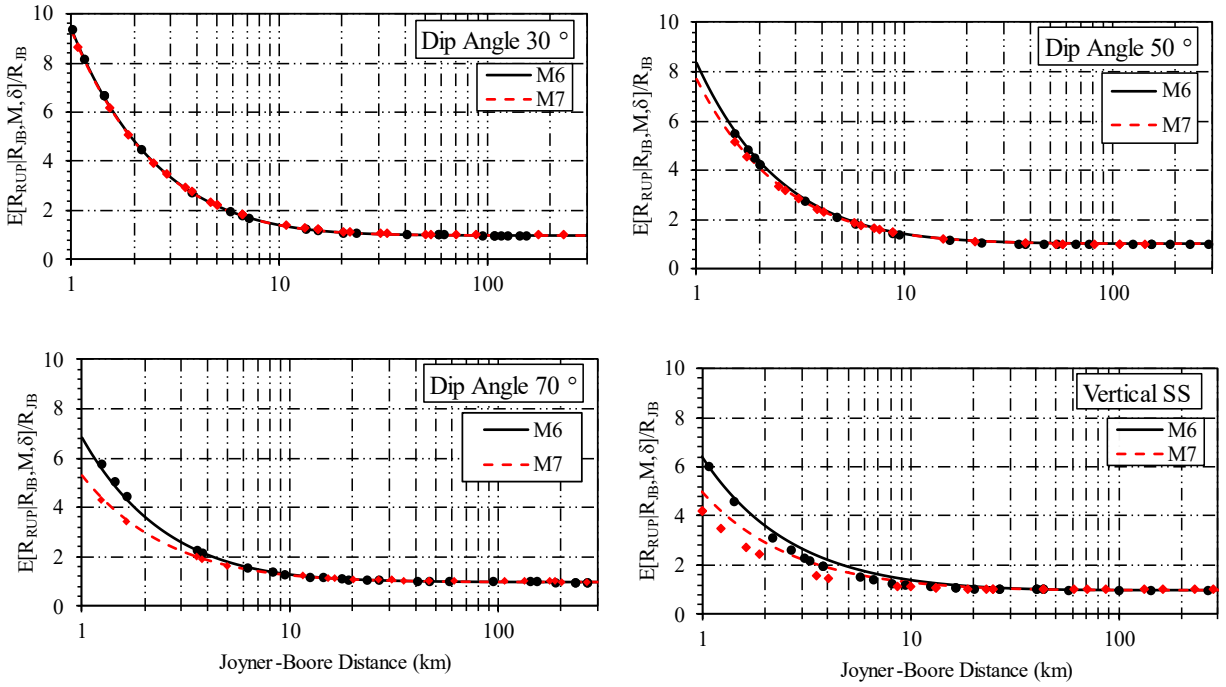

Figure 4.1 Comparison of the ratio of R_{RUP} to R_{JB} versus R_{JB} for dip-slip fault with dip angles of **30°**, **50°**, and 70°, and vertical strike-slip fault for moment magnitudes of 6 (solid line) and 7 (dashed line). The dots represent the mean values for the distribution, and the lines represent the empirical equations fitted to the distribution.

Table 4.1 Coefficients for E [$R_{RUP}|R_{JB}$, M, $\boldsymbol{\delta}$] at different dip angles for a given Magnitude (M) and Joyner-Boore distance (R_{JB}) (azimuth angle ($\boldsymbol{\theta}$) and hypocenter location are randomized).

δ	Mean					Footwall			Hanging wall		
	C_1	C_2	C_3	C_4	C_5	C_6	C_7	C_8	C_6	C_7	C_8
10	2.921	-0.0561	0.0193	7.230	0.1330	0.4552	0.4328	0.0378	0.2143	0.6287	0.0309
20	2.791	-0.0379	0.0184	7.015	0.1265	0.7921	0.4583	0.0350	0.3910	0.6414	0.0291
30	2.694	-0.0255	0.0175	6.516	0.1166	0.9846	0.4824	0.0309	0.5210	0.6486	0.0263
40	2.971	-0.0329	0.0183	5.544	0.1126	1.0360	0.5036	0.0261	0.5995	0.6443	0.0226
50	4.527	-0.2602	0.2028	4.647	0.0281	0.9599	0.5208	0.0209	0.6166	0.6339	0.0183
60	5.795	-0.6589	0.2502	4.378	0.0265	0.7832	0.5324	0.0152	0.5639	0.6144	0.0134
70	7.240	-0.7457	0.1909	3.028	0.0185	0.5390	0.5383	0.0090	0.4366	0.5898	0.0080
80	8.616	-0.7218	0.1365	1.481	0.0089	0.2631	0.5418	0.0024	0.2387	0.5641	0.0019
90	3.634	-0.7624	0.0424	3.896	0.0262						

4.1.2 Joyner-Boore distance and Epicentral distance

The azimuth angles from 0° to 90° can model the entire range of possible values for R_{EPI} for a given R_{JB} at a given length, width, and dip angle of the fault. The regression analysis is performed separately for the dip-slip fault ($\delta \neq 90°$) and vertical strike-slip fault ($\delta = 90°$). The functional form that can fit the mean values of R_{EPI} at different R_{JB} for a dip-slip fault is

$$\mathrm{E}[\mathrm{R}_{\mathrm{REPI}}|\mathrm{R}_{\mathrm{JB}}, \mathrm{M}, \delta] = R_{JB} + C_1 \exp(C_2(M-5)^2)\left(R_{JB}^{C_3} - C_4\right) + C_5 R_{JB}^{C_6} + C_7 \exp\left(C_8(M-5)\right) + \sigma_{EPI} \qquad (4.4)$$

Similarly, for the vertical strike-slip fault ($\delta = 90°$),

$$\mathrm{E}[\mathrm{R}_{EPI}|\mathrm{R}_{\mathrm{JB}}, \mathrm{M}, \delta] = \mathrm{R}_{\mathrm{JB}} + C_1 \exp(C_2(M-5))\left(R_{JB}^{C_3} - C_4\right) + C_5 R_{JB}^{C_6} + C_7 \exp\left(C_8(M-5)\right) + \sigma_{\mathrm{EPI}} \qquad (4.5)$$

where the coefficients C_1 to C_8 are obtained from regression analysis and presented in Table 4.2. σ_{EPI} is the standard deviation discussed later. The coefficients are different for different dip angles. The coefficients for dip angles not listed can be determined using interpolation. Figure 4.2 shows the variation of R_{EPI} obtained from the empirical equations with the mean for dip-slip faults with dip angles of 30°, 50°, and 70°, respectively. R_{EPI} is always greater than or equal to R_{JB} at all magnitudes and dip angles. The difference between the two distances is substantial for dip-slip faults at higher magnitudes. At R_{JB} of 1 km, R_{EPI} for a 30° dip-slip fault is three times greater for M 6 and five times greater for M 7. Since the rupture area increases with magnitude, the length and width of the fault are large for higher magnitudes, resulting in higher mean R_{EPI} values for the same R_{JB} values. This effect of large magnitude is less prominent for the vertical strike-slip fault since only one fault dimension, the length of the fault, affects R_{EPI}.

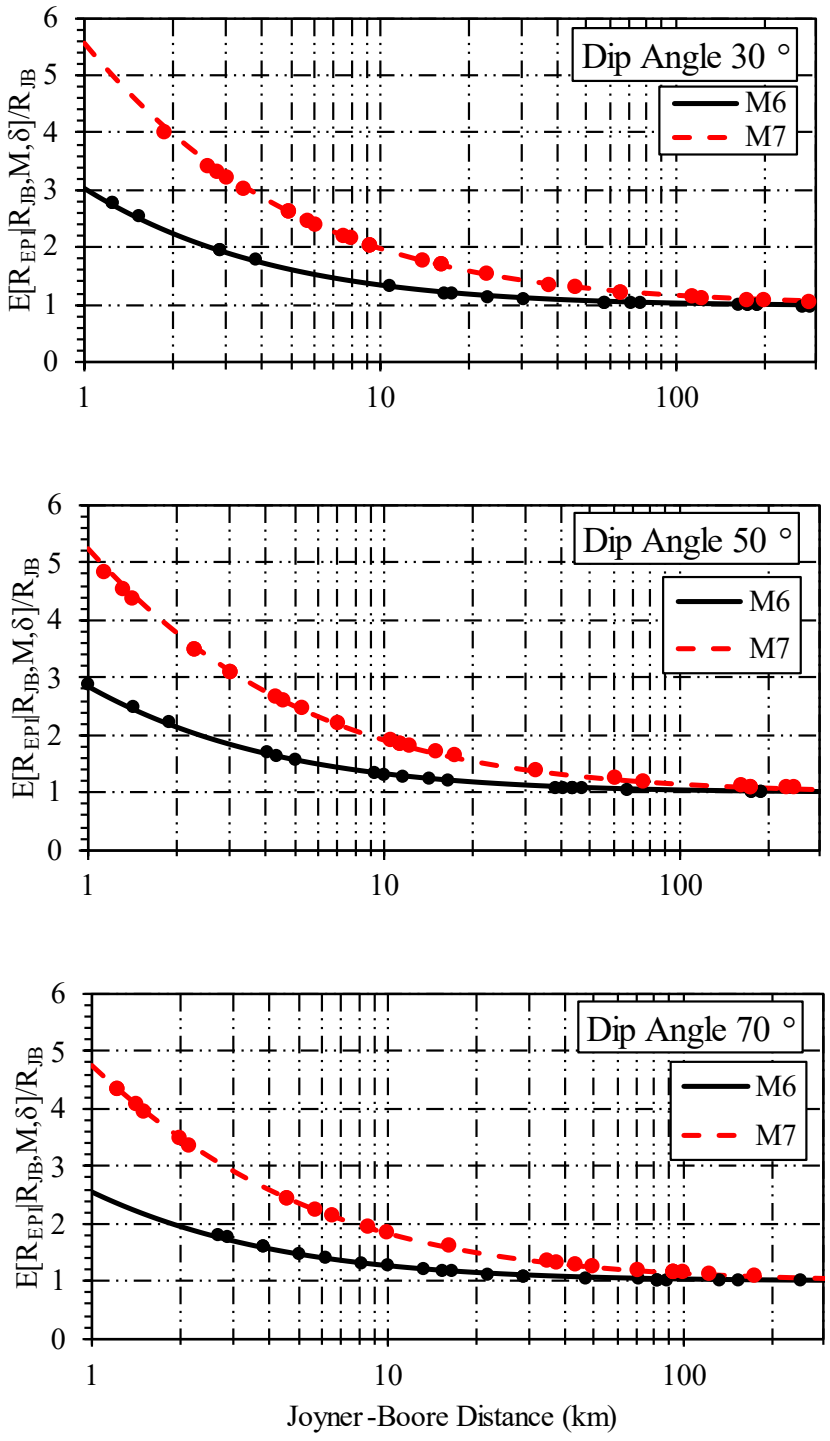

Figure 4.2 Comparison of the ratio of R_{EPI} to R_{JB} versus R_{JB} for dip-slip fault with dip angles of **30°**, **50°**, and 70° for moment magnitudes of 6 (solid line) and 7 (dashed line). The dots represent the mean values for the distribution, and the lines represent the empirical equations fitted to the distribution.

Table 4.2 Coefficients for E [$R_{EPI}|R_{JB}$, M, $\boldsymbol{\delta}$] at different dip angles for a given Magnitude (M) and Joyner-Boore distance (R_{JB}) (azimuth angle ($\boldsymbol{\theta}$) and hypocenter location are randomized).

δ	C_1	C_2	C_3	C_4	C_5	C_6	C_7	C_8
10	3.595	0.2506	0.24	0.8218	-0.9044	0.4764	1.267	0.5607
20	3.56	0.252	0.239	0.8151	-0.9039	0.4742	1.234	0.5588
30	3.52	0.2542	0.237	0.8044	-0.9142	0.4688	1.192	0.5495
40	3.46	0.2568	0.2345	0.7781	-0.9315	0.4609	1.107	0.5342
50	3.403	0.2601	0.2308	0.7478	-0.9674	0.443	1.023	0.5021
60	3.377	0.2637	0.2253	0.713	-1.038	0.4296	0.947	0.4405
70	3.537	0.2653	0.2151	0.6761	-1.319	0.3846	1.064	0.2525
80	3.846	0.2646	0.2021	0.6551	-1.854	0.3269	1.483	0.0026
90	0.2211	1.74	0.188	0.7227	-0.00295	1.169	0.5337	0.4944

4.1.3 Joyner-Boore distance and Hypocentral distance

Due to symmetry, the azimuth angles from 0° to 90° are used to obtain R_{HYP} for a given R_{JB} at different magnitudes and dip angles. As discussed, separate regressions are carried out at different dip angles. Equation (4.6) provides the equation for the dip-slip fault, and equation (4.7) for the vertical strike-slip fault.

$$\begin{aligned} &\mathrm{E}[\mathrm{R}_{HYP}|\mathrm{R}_{\mathrm{JB}}, \mathrm{M}, \delta, \mathrm{Z}_{\mathrm{TOR}}] \\ &= \sqrt{\mathrm{R}_{\mathrm{JB}}^2 + \mathrm{Z}_{\mathrm{TOR}}^2} + C_1 \exp(C_2(M-5)^2)\left(R_{JB}^{C_3} - C_4\right) + C_5 R_{JB}^{C_6} + C_7 \exp\left(C_8(M-5)\right) \\ &+ \sigma_{\mathrm{HYP}} \end{aligned} \tag{4.6}$$

$$E[R_{HYP}|R_{JB}, M, \delta, Z_{TOR}]$$

$$= \sqrt{R_{JB}^2 + Z_{TOR}^2} + C_1 \exp(C_2(M-5)) \left(R_{JB}^{C_3} - C_4\right) + C_5 R_{JB}^{C_6} + C_7 \exp\left(C_8(M-5)\right) \quad (4.7)$$

$$+ \sigma_{HYP}$$

where parameters C_1 to C_8 are regression coefficients and are provided in Table 4.3. 'M' is the moment magnitude, δ is the dip angle, and Z_{TOR} is the depth to the top of the rupture. σ_{HYP} is the standard deviation discussed later.

Apart from magnitude, dip angle, and R_{JB}, R_{HYP} also depends on the depth to the top of the rupture (Z_{TOR}). A comparison of the fitting of the mean values with the empirical equation is shown in Figure 4.3 for dip angles of 30°, 50°, and 70°, respectively. R_{HYP} increases slightly with increasing magnitude at small distances and converges at large R_{JB} values.

Table 4.3 Coefficients for E [$R_{HYP}|R_{JB}$, M, $\boldsymbol{\delta}$, Z_{TOR}] at different dip angles for a given Magnitude (M), depth to the top of the rupture (Z_{TOR}), and Joyner-Boore distance (R_{JB}) (azimuth angle ($\boldsymbol{\theta}$) and hypocenter location are randomized).

δ	C_1	C_2	C_3	C_4	C_5	C_6	C_7	C_8
10	4.75	0.242	0.2242	0.9981	-0.563	0.579	0.6626	0.7618
20	4.207	0.2556	0.2203	1.045	-0.5616	0.5622	1.25	0.6849
30	3.656	0.2706	0.2174	1.082	-0.608	0.5306	1.793	0.6471
40	3.112	0.2864	0.2162	1.099	-0.7109	0.4867	2.273	0.6175
50	2.634	0.3028	0.2157	1.101	-0.8945	0.4333	2.746	0.584
60	2.246	0.319	0.215	1.092	-1.135	0.3839	3.184	0.5505
70	2.02	0.3321	0.2119	1.065	-1.438	0.3429	3.601	0.511
80	1.87	0.3429	0.2075	1.041	-1.628	0.3243	3.828	0.4867
90	1.846	0.3573	0.1933	1.086	-2.031	0.2987	4.533	0.455

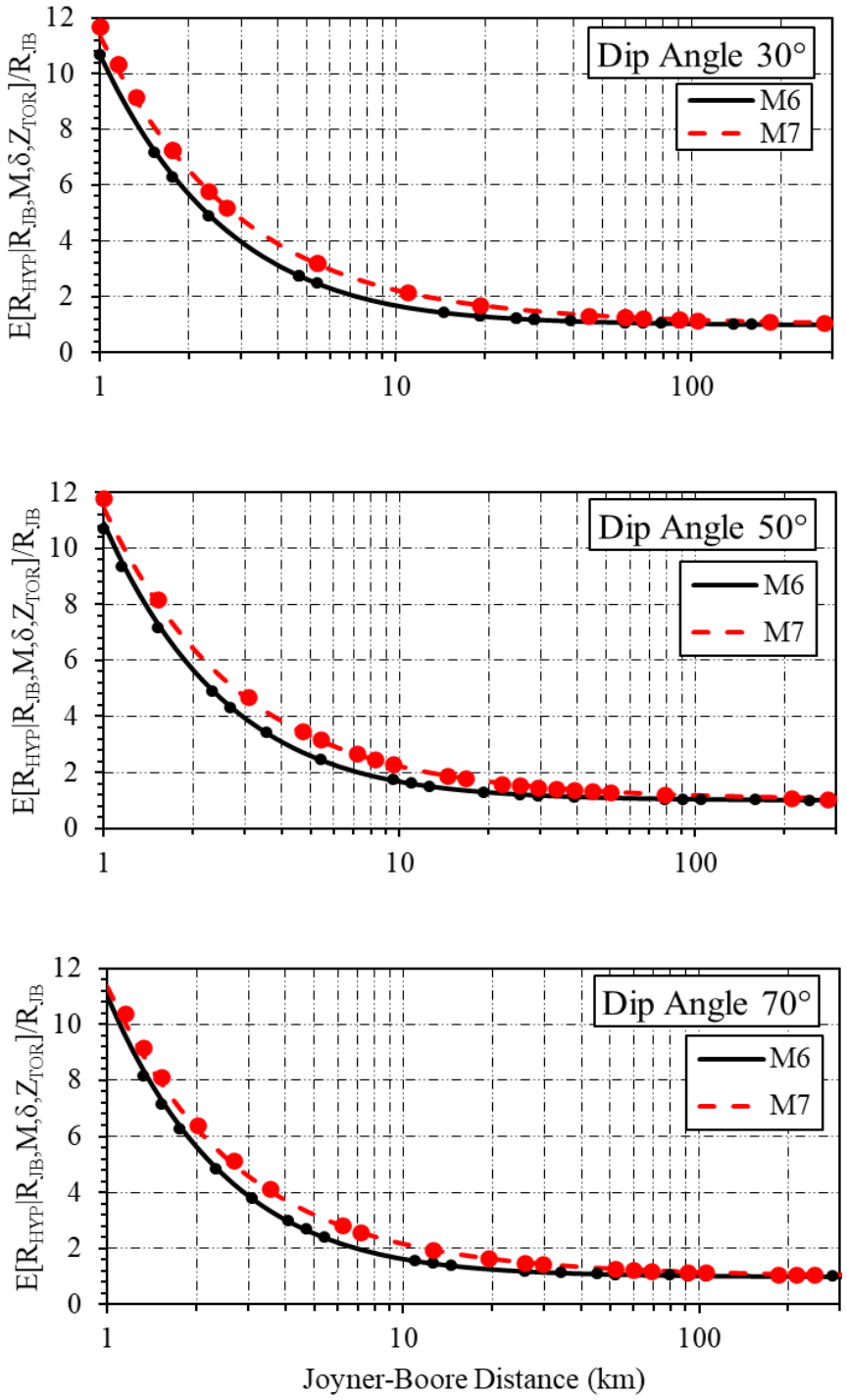

Figure 4.3 Comparison of the ratio of R_{HYP} to R_{JB} versus R_{JB} for dip-slip fault with dip angles of **30°**, **50°**, and 70° for moment magnitudes of 6 (solid line) and 7 (dashed line). The dots represent the mean values for the distribution, and the lines represent the empirical equations fitted to the distribution.

4.2 Residuals

To evaluate the proposed empirical equation for mean R_{RUP}, we plot the residuals, which are the differences between the predicted mean R_{RUP} values and the actual mean R_{RUP} values, as shown in Figure 4.4 for M 6 and M 7 for dip-slip faults with dip angles of 30°, 50°, 70°, and for a vertical strike-slip fault. For a dip angle of 30°, the difference between the calculated and actual values is only $\pm$0.2 km. The maximum difference of 0.4 km can be observed for M 7 at 100 km for a 50° dip-slip fault. Similarly, we calculated the residuals for R_{EPI} and R_{HYP}. As shown in Figure 4.5 for R_{EPI}, we can observe a maximum variation of $\pm$3.0 km, though it is observed at large distances (>100 km). At smaller distances (< 30 km), the residuals are nearly equal to 0 km at all dip angles. We can make similar observations for mean $R_{HYP,}$ as shown in Figure 4.6.

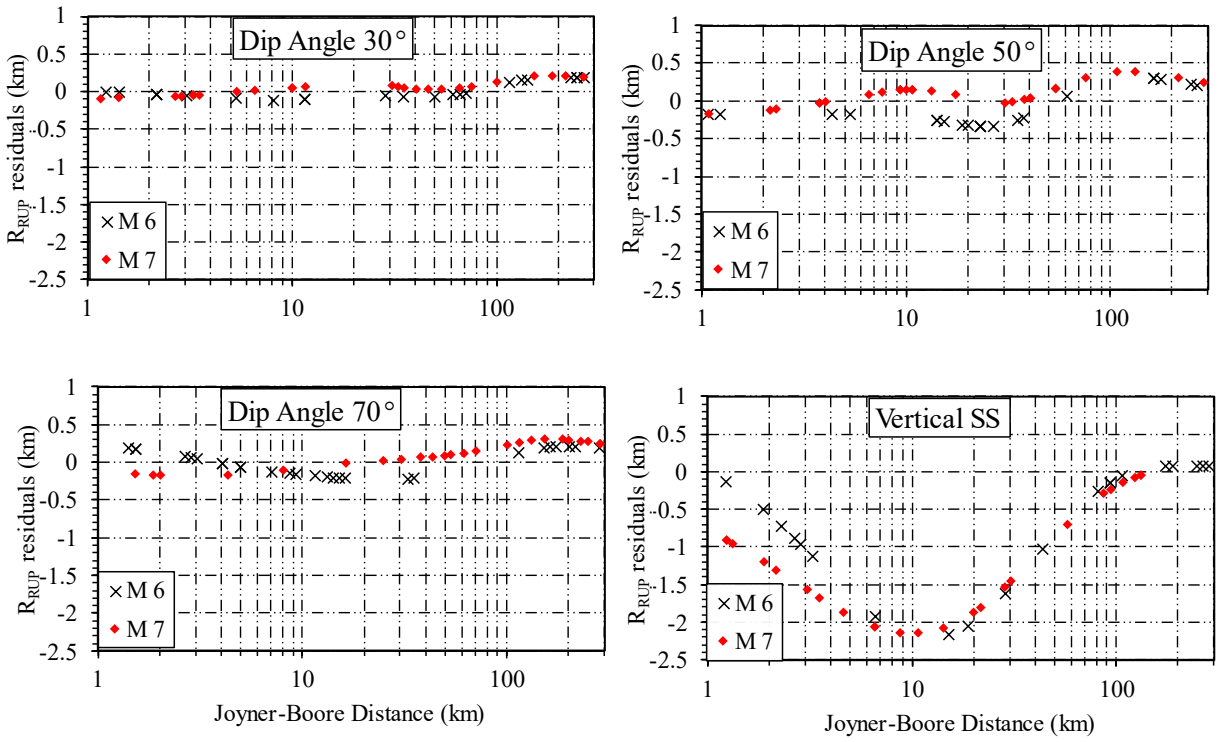

Figure 4.4 Residual values at M 6 and M 7 for mean R_{RUP} at dip angles 30°, 50°, 70°, and for vertical strike-slip fault.

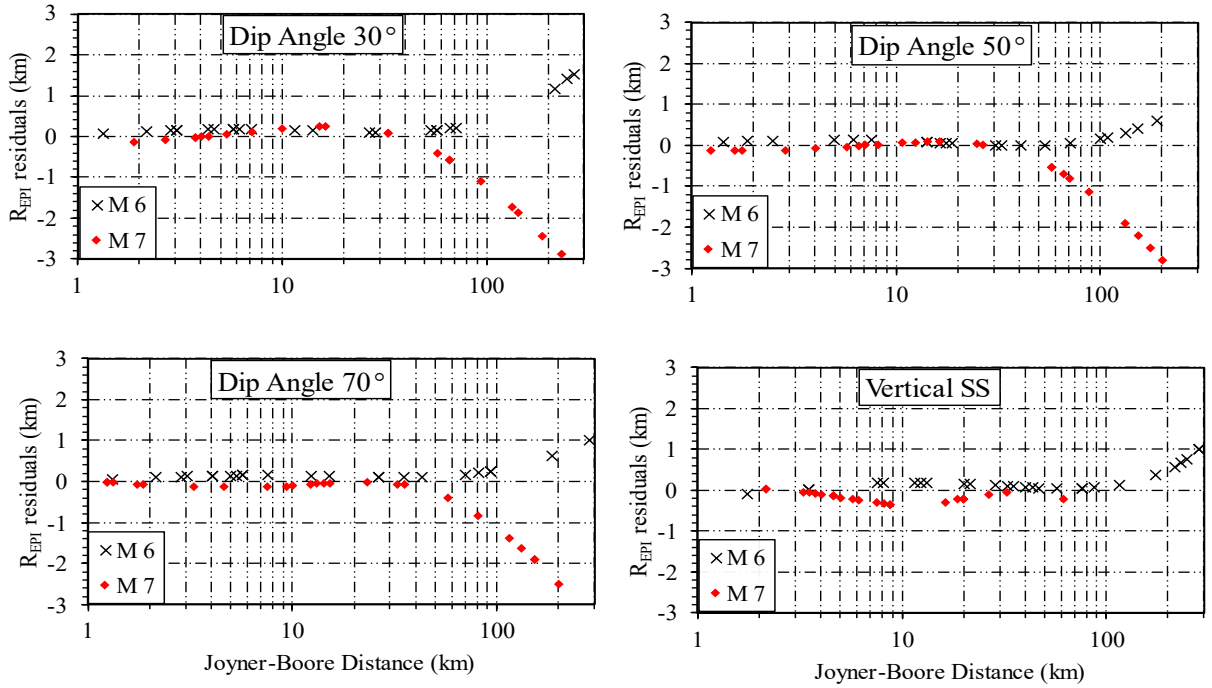

Figure 4.5 Residual values at M 6 and M 7 for mean R_{EPI} at dip angles 30°, 50°, 70°, and for vertical strike-slip fault.

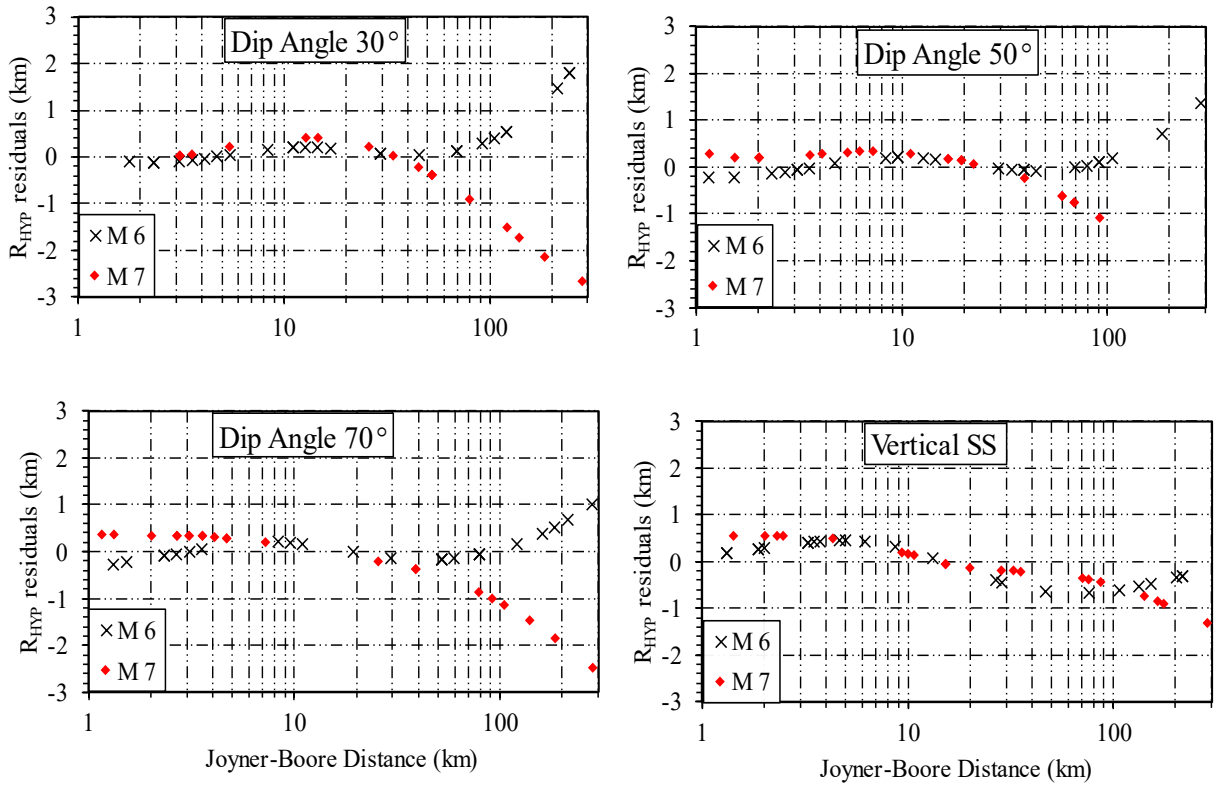

Figure 4.6 Residual values at M 6 and M 7 for mean R_{HYP} at dip angles 30°, 50°, 70°, and for vertical strike-slip fault.

4.3 Effect of hanging wall and footwall

Many GMMs have a hanging wall or footwall flag which is used to fix the site on the hanging wall or the footwall side of the fault. In this section, we study the impact of the location of the site about the fault. For this study, we examine a dip-slip fault with a 50° dip angle at M 7 as shown in Figure 4.7. We have an 80 km by 80 km plot varying from -40 to 40 in both directions, as shown in Figure 4.7. The center of the fault is located at the center of the plot (0,0). We generate observation sites on the plot with a gridded density of 1 km (only a small sample of observation sites are shown in Figure 4.7 for clarity). For each observation point, we calculate the R_{JB} and the target distance metric (R_{target}) from the fault. We divide R_{target} by R_{JB} to determine the ratio. We then use the calculated ratios to plot the contour map.

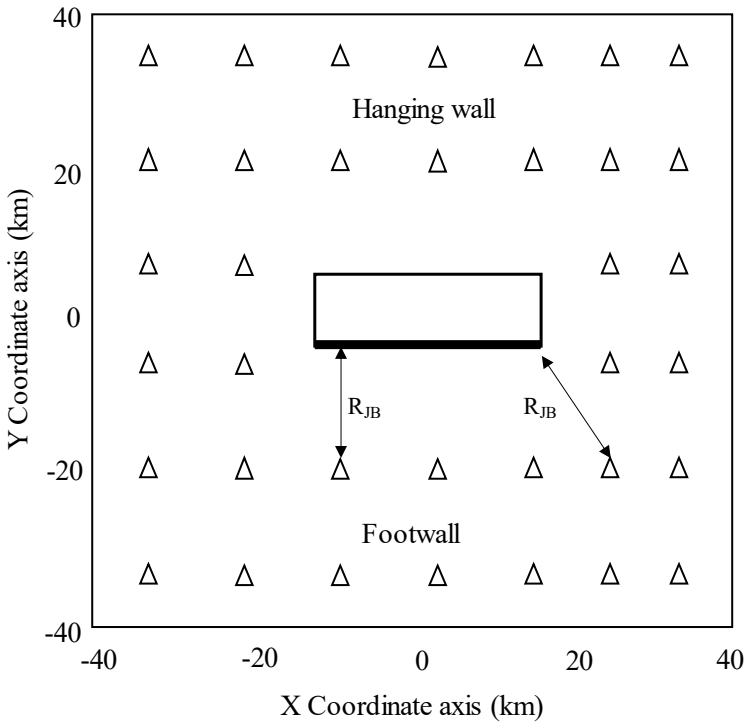

Figure 4.7 The rectangle represents the projection of the ruptured fault on the surface. The dark line represents the projection of the top edge of the ruptured fault. The triangles represent the observation sites located at every 1 km R_{JB} from the center (0,0) (Only a small sample of observation sites are shown for clarity). The length and width of the fault are based on the magnitude and dip angle calculated using Somerville (2014). The center of the fault is (0,0).

4.3.1 Effect on R_{RUP}

For the dip-slip fault, R_{RUP} is always measured from the top of the rupture to the site on the footwall side of the fault. However, at the hanging wall side of the fault, R_{RUP} is also dependent on the depth of the rupture and dip angle. So, R_{RUP} calculated on the footwall side of the fault is always less than or equal to R_{RUP} calculated on the hanging wall side of the fault for a constant R_{JB}, as shown in Figure 4.8 and Figure 4.9. The R_{RUP} is calculated in Figure 4.8 based on the geometry of the fault, as presented in equation (3.16). The R_{RUP} for Figure 4.9 is based on the empirical equations for R_{RUP} (equation 4.2). For both figures, the contours of the ratios are closer together on the footwall side of the fault, representing smaller R_{RUP} values for the same R_{JB} values. The contours

of the ratios are further apart at the hanging side of the fault. Also, R_{RUP} and R_{JB} values are the same (representing the ratio of 1) for R_{JB} greater than 15 km for the footwall and 40 km for the hanging wall.

In Figure 4.8, the variation of R_{RUP} is gradual from the footwall to the hanging wall side of the fault, but the variation is abrupt in Figure 4.9, as we have used a step function. For a more gradual variation, we can use the mean equation of the R_{RUP} for the sites along the width of the fault. We have also plotted similar contour plots for Scherbaum et al. (2004). Since they do not differentiate between the hanging wall and the footwall side of the fault, the contour lines are uniform across the fault as shown in Figure 4.10.

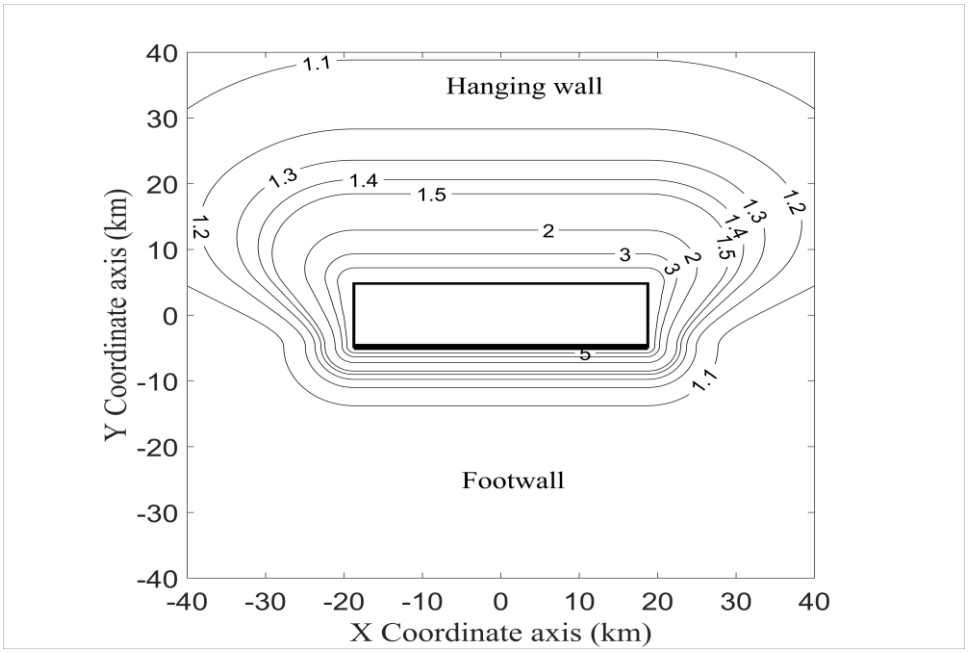

Figure 4.8 Contour plot for the ratio of R_{RUP} to R_{JB} for Magnitude 7 and dip angle **50**°. R_{RUP} is calculated using equation (3.16). The contour of the ratios is closer together at the footwall side of the fault than the hanging wall side of the fault, as R_{RUP} for a given R_{JB} is smaller at the footwall compared to the hanging wall side of the fault.

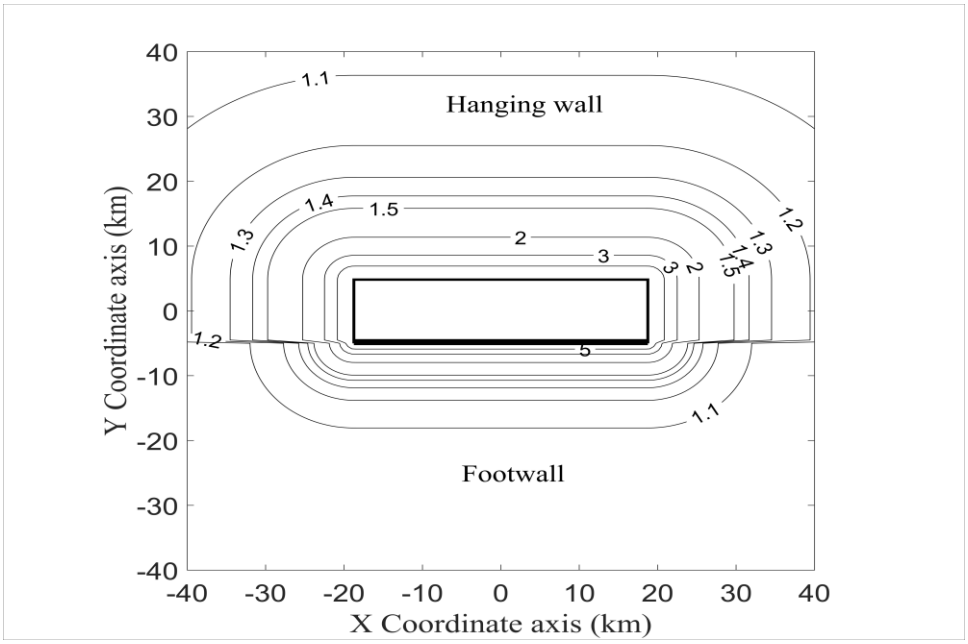

Figure 4.9 Contour plot for the ratio of R_{RUP} to R_{JB} for Magnitude 7 and dip angle **50°**. R_{RUP} is calculated using equation (4.2). The contour of the ratios is closer together at the footwall side of the fault than the hanging wall side of the fault, as R_{RUP} for a given R_{JB} is smaller at the footwall compared to the hanging wall side of the fault.

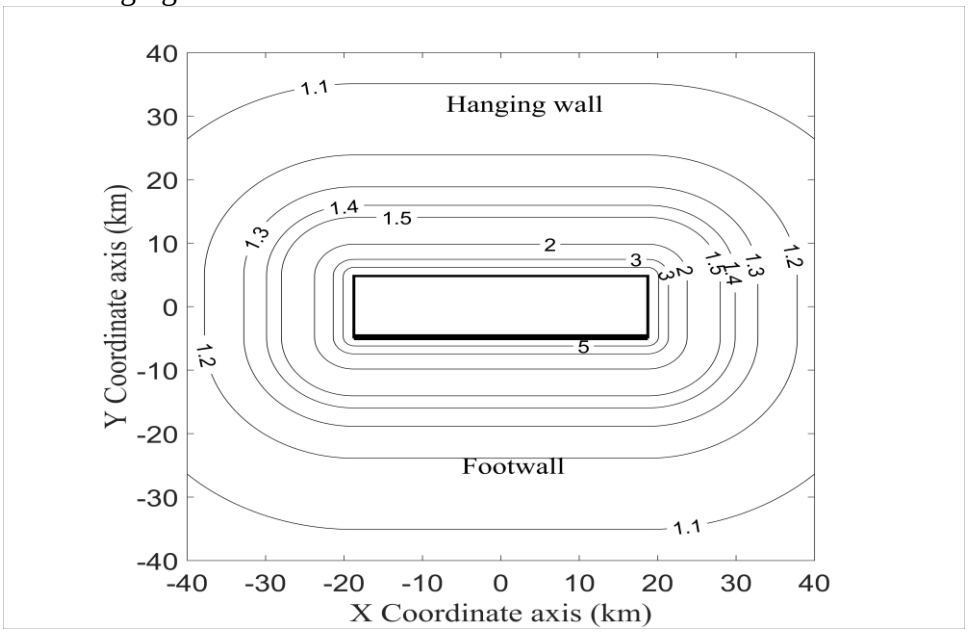

Figure 4.10 Contour plot for the ratio of R_{RUP} to R_{JB} for Magnitude 7 and dip angle **50°**. R_{RUP} is calculated based on Scherbaum et al. (2004). The contour of the ratios is the same on both the footwall side of the fault and the hanging wall side of the fault. Scherbaum et al. (2004) also do not differentiate between different dip angles for the dip-slip fault so the results would not change for other dip angles of the same magnitude.

4.3.2 Effect on R_{EPI}

Unlike R_{RUP}, which is a fault-based distance metric, R_{EPI} is a point-based distance metric. So, we do not observe any effect of hanging wall or footwall on the estimation of R_{EPI}. Figure 4.11 shows the contour plot for the ratio of R_{EPI} to R_{JB} for a dip-slip fault with a dip angle of 50° and M 7. R_{EPI} is calculated based on the geometry of the fault using equation (3.17). We can observe that the contours on the hanging wall side and the footwall side of the fault are similar. The only variation is due to the azimuth of the fault to the site. The ratios are higher parallel to the fault and are smaller perpendicular to the fault. Figure 4.12 shows the contour plot for the ratio of mean R_{EPI} to R_{JB} calculated using equation (4.4). Since the mean of the values across all the azimuths of the fault is used, the contour is uniform across the fault.

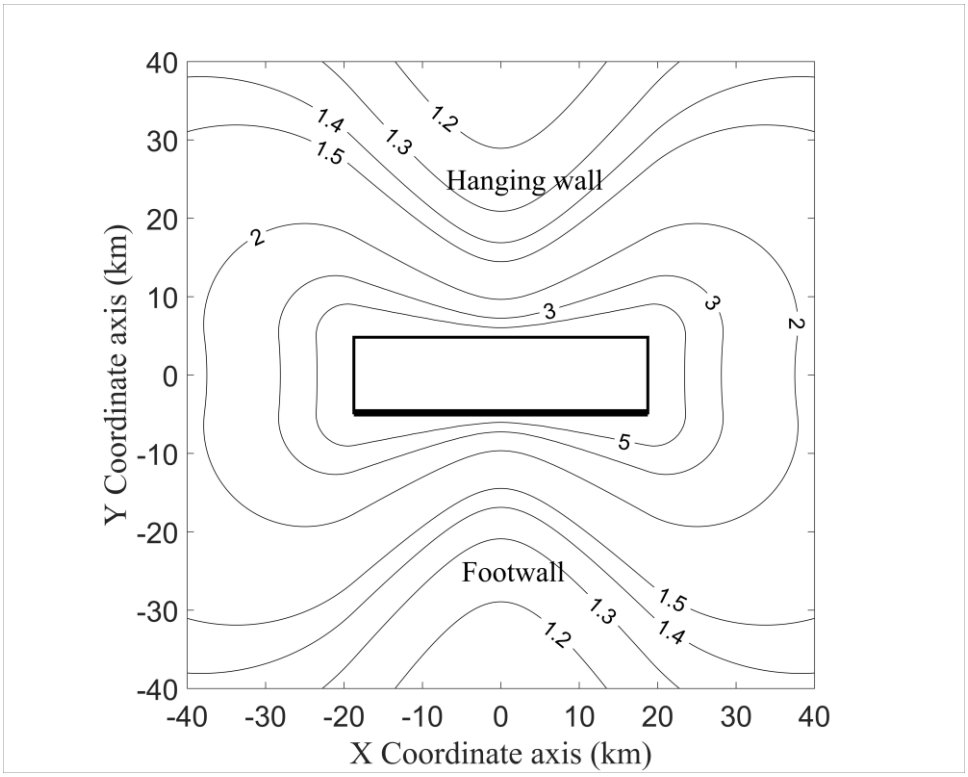

Figure 4.11 Contour plots for the ratio of R_{EPI} to R_{JB} for a M 7 earthquake with dip angle **50°**. R_{EPI} is calculated based on the geometry of the fault using equation (3.17).

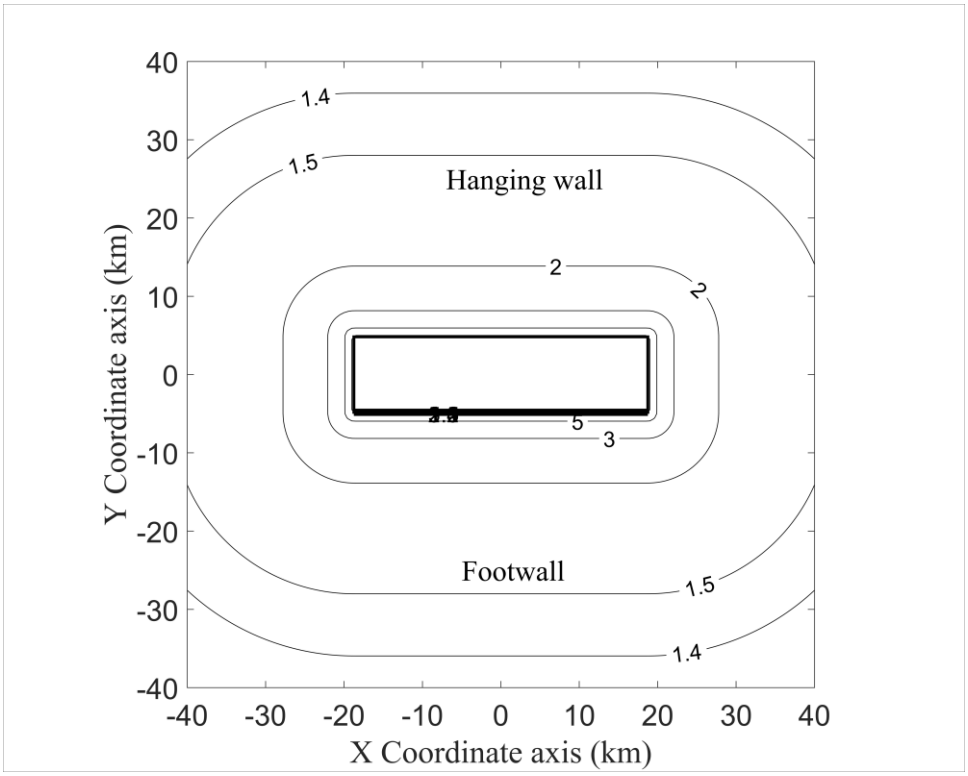

Figure 4.12 Contour plots for the ratio of R_{EPI} to R_{JB} for a M 7 earthquake with dip angle **50°**. R_{EPI} is calculated using the empirical equation (4.4).

4.3.3 Effect on R_{HYP}

Similar to R_{EPI}, R_{HYP} is also a point-based distance metric, so we do not observe any effect of hanging wall or footwall on the estimation of R_{HYP}. Figure 4.13 shows the contour plot for the ratio of R_{HYP} to R_{JB} for a dip-slip fault with a dip angle of 50° and M 7. R_{HYP} is calculated based on the geometry of the fault using equation (3.18). We can observe that the contours on the hanging wall side and the footwall side of the fault are similar. We can also observe the variation due to the azimuth of the fault to the site, with the ratios higher parallel to the fault and smaller perpendicular to the fault. Figure 4.14 shows the contour plot for the ratio of mean R_{HYP} to R_{JB} calculated using equation (4.6). Since the mean of the values across all the azimuths of the fault is used, the contour is uniform across the fault.

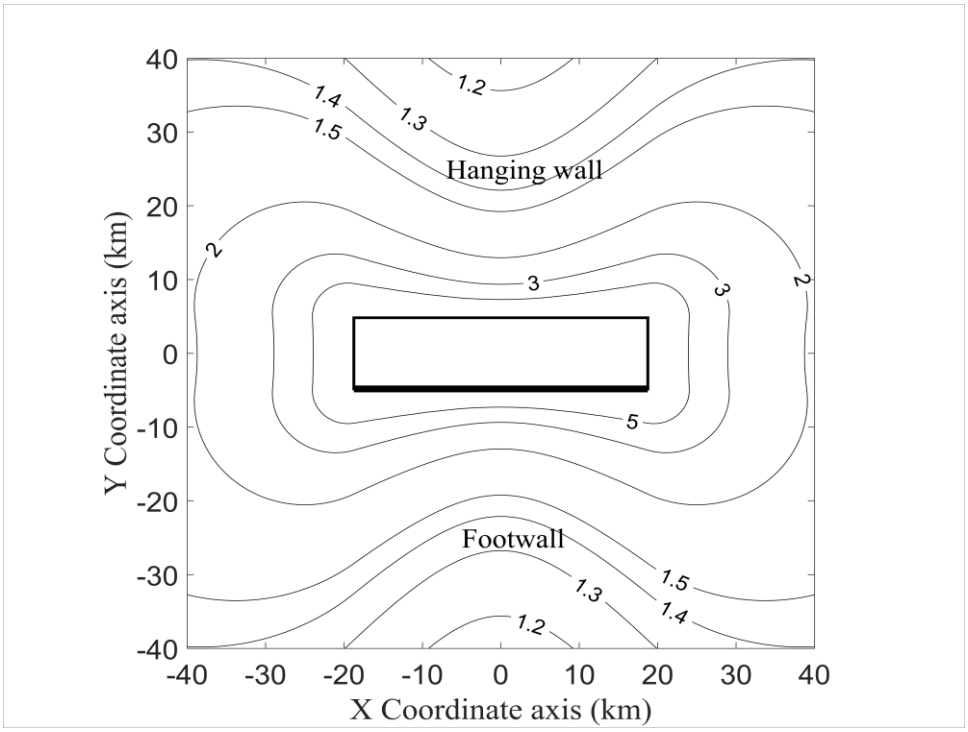

Figure 4.13 Contour plots for the ratio of R_{HYP} to R_{JB} for a M 7 earthquake with dip angle **50°**. R_{HYP} is calculated using equation (3.18).

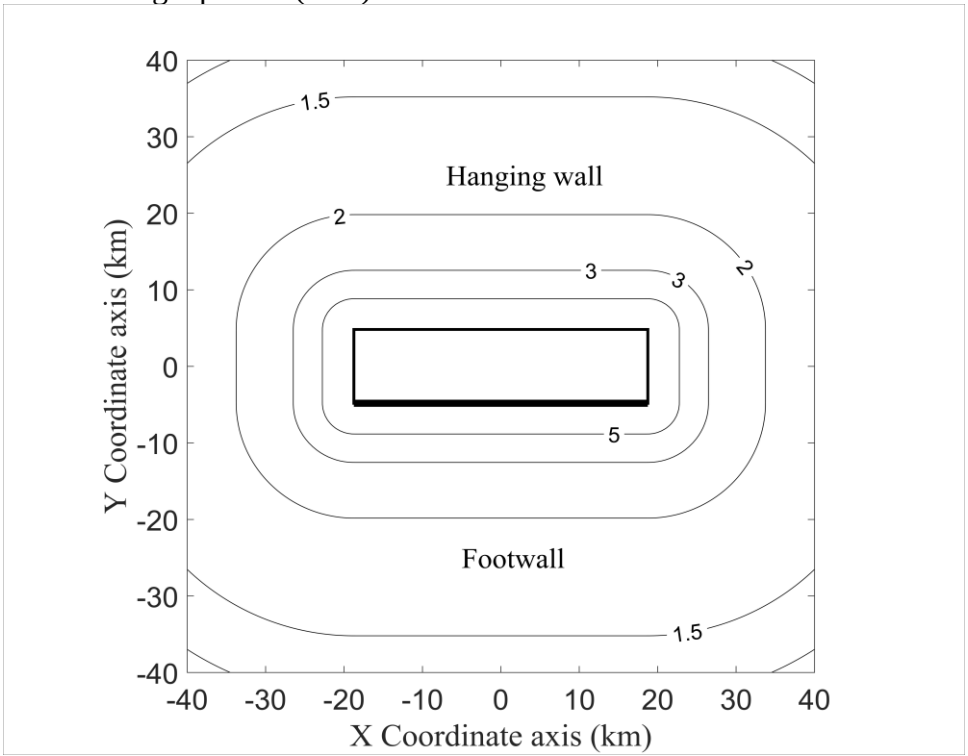

Figure 4.14 Contour plots for the ratio of R_{HYP} to R_{JB} for a M 7 earthquake with dip angle **50°**. R_{HYP} is calculated using equation (4.6).

4.4 Discussions

We compared our results with the equations provided by Scherbaum et al. (2004), EPRI (2004), and Thompson and Worden (2018). Scherbaum et al. (2004) provided a polynomial equation with different coefficients for different distance conversions. Different GMMs have been defined by EPRI (2004): three models (GMM-1, GMM-2, and GMM-4) based on R_{JB}, and one model (GMM-3) based on R_{RUP}. They have also provided equations to convert these distance metrics to R_{EPI} for each GMM. The assumptions for each published study we have used for comparison are listed in

Table 4.4. Figure 4.15 shows the variation of the ratio of R_{target} to R_{JB} versus R_{JB} for different magnitude events and compares the values with those obtained from other published studies. Since Scherbaum et al. (2004) are limited to M 7.5, we have provided a comparison for M 6 and M 7. For the ratio of R_{EPI} to R_{JB}, Scherbaum et al. (2004) predict higher values at smaller distances (<10 km), while EPRI (2004) predicts comparatively lower values. The values for the strike-slip model developed in this study closely follow other studies for distances greater than 10 km at all magnitudes. The values obtained from the proposed empirical equations and Thompson and Worden (2018) differ from EPRI (2004) at smaller distances (<10 km) for M 7. The differences in values result from different assumptions and methodologies. The calculations used in this study and Thompson and Worden (2018) are also independent of GMMs or the oscillator period. Overall, the values are consistent with the other published studies.

The comparison of variation of the ratio of R_{RUP} to R_{JB} versus R_{JB} is also presented in Figure 4.15 for M 6 and M 7. The comparison is shown for the dip-slip fault. For the comparison, we have used a dip angle of 60°, though other dip angles also provide similar results. EPRI (2004) does not provide a separate equation to convert between R_{JB} and R_{RUP}. The values obtained from this study

are slightly higher at a smaller distance (< 10 km) compared to other published studies for M 6. The values are consistent at distances greater than 10 km for all magnitudes. The variation in the values at distances less than 10 km directly results from the choice of depth to the top of the rupture (Z_{TOR}). At smaller distances, the calculated R_{RUP} is directly affected by Z_{TOR}. Z_{TOR} does not have a significant impact on R_{RUP} at large distances. For magnitude 7, the mean R_{RUP} calculated in this study is similar to other published studies. For all magnitudes, the calculated R_{RUP} from all the studies falls between the R_{RUP} calculated for the hanging wall and the footwall in this study.

Only Scherbaum et al. (2004) have provided an empirical relationship between R_{HYP} and R_{JB}. The values are consistent with this study for M 6 and M 7. For calculation, we have assumed the depth to the top of the rupture as 3 km. Similar to R_{RUP}, R_{HYP} is also sensitive to Z_{TOR} value at small distances.

Table 4.4 Distance conversion assumptions from different published studies used for comparison in this study.

Description	Fault Type	Magnitude Scaling relation	Aspect Ratio (AR)	Depth (km)
This study	Strike-slip	Somerville (2014)	1	0-15
This study	Dip-slip	Somerville (2014)	1	0-15
EPRI (2004)	Strike-slip	Somerville (2004)	3	0-25
EPRI (2004)	Dip-slip	Somerville (2004)	2	0-25
Scherbaum et al. (2004)	Strike-slip Dip-slip	Wells and Coppersmith (1994)		
Thompson and Worden (2018)	Strike-slip	Somerville (2014)	1	0-15
Thompson and Worden (2018)	Dip-slip	Somerville (2014)	1	0-15

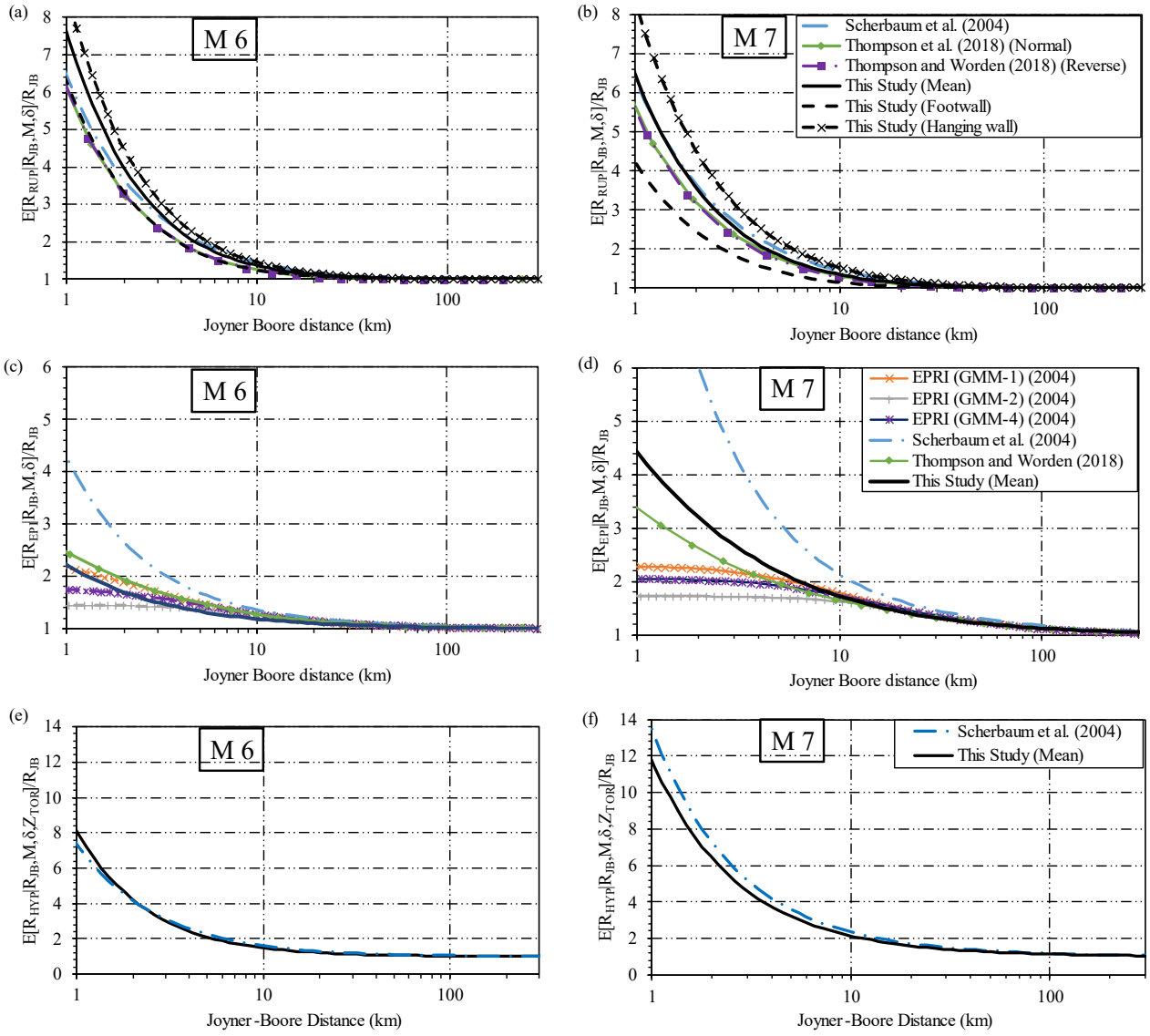

Figure 4.15 Comparison with other models for mean distance conversion at Magnitude 6 (left) and Magnitude 7 (right) for R_{RUP}, R_{EPI}, and R_{HYP}. The mean results for R_{EPI} and R_{HYP} are based on the strike-slip fault, and the mean results for R_{RUP} are based on the 60° dip-slip fault. The comparison is made with other published studies which provide a relationship for the conversion of each distance metric. For example, Scherbaum et al. (2004) provide relationships for R_{JB}, R_{RUP}, R_{EPI}, and R_{HYP}, while EPRI (2004) and Thompson et al. (2018) provide relationships only for R_{EPI}, R_{JB}, and R_{RUP}. For R_{HYP}, the Z_{TOR} value is fixed at 3 km.

4.5 Chapter Conclusion

In this chapter, we proposed the empirical equations for different distance metrics based on the mean values at various azimuths of the fault. The proposed empirical equations are dependent on the magnitude of the earthquake, the dip angle of the fault, and the depth to the top of the rupture. We have developed the empirical equations for R_{RUP}, R_{EPI}, and R_{HYP}. Based on the residual calculations for the actual and the predicted target distances, we can conclude that the proposed empirical equations can accurately predict the mean of the target distances. The proposed empirical equations also include the effect of hanging wall and footwall, which is not observed in other similar distance metric prediction equations. Overall, the result from the proposed empirical equations provides values similar to other published studies. The proposed empirical equations can be used in seismic hazard analysis to convert from R_{JB} to other distance metrics for any ground motion models for the stable continental region.

Chapter 5 Capturing the uncertainty in distance metric conversions

5.1 Introduction

The proposed empirical equations discussed in Chapter 4 provide the mean target distance for a given magnitude, dip angle, and Joyner-Boore distance. There are several uncertainties in the calculated distance metrics associated with the variation in azimuth angle from the site to the fault, location of the hypocenter, distribution of hypocenter location, and directivity effects. To accurately determine the seismic hazard of an area, it is crucial to consider the effect of these uncertainties in the calculated hazard (Kayastha et al., 2022b). In this chapter, we have proposed empirical equations to capture the uncertainties in the distance metrics conversions for each target distance metric. The proposed equations are based on the magnitude (M) of the earthquake event, the Joyner-Boore distance (R_{JB}), and the dip angle of the fault. Our dataset has considered variations along different azimuth angles from the fault. We have also considered variations for the rupture area of the fault for the same magnitude using epsilon values ranging from -3 to 3 for the magnitude scaling relationship Somerville (2014). We have also assumed various locations for the hypocenter along the length, width, and depth of the fault based on Mai et al. (2005). The effects of directivity have not been considered in this study.

5.2 Sigma Models for distance metrics conversion

5.2.1 Rupture distance and Joyner-Boore distance

The sigma for R_{RUP} is based on M, δ, and R_{JB} and can be represented as follows:

$$\sigma_{[R_{RUP}|R_{JB},M,\delta]} = C_1 \exp\left(C_2(M-5)\right) * \exp\left(-C_3 R_{JB}\right) \quad (5.1)$$

where regression coefficients C_1 to C_3 are provided in Table 5.1 as a function of dip angles. The coefficients differ for the mean, hanging wall, or footwall side of the fault. For the vertical strike-

slip fault, only coefficients for the mean are provided, as there is no hanging wall effect. As discussed previously, the coefficients for dip angles not listed can be determined by interpolation. The sigma values increase with increasing dip angle for smaller magnitudes (M<6.0). Above M 6.0, no specific trends between the sigma and dip angle could be observed. The sigma also increases with increasing magnitudes for all dip angles. However, there is a decrease in sigma with increasing distance since there is less variation in values at larger distances (because R_{JB} and R_{RUP} are almost the same at large distances).

Table 5.1 Coefficients for calculation of $\boldsymbol{\sigma}_{[\boldsymbol{RRUP}|\boldsymbol{RJB},\boldsymbol{M},\boldsymbol{\delta}]}$ at different dip angles for a given Magnitude (M) and Joyner-Boore distance (R_{JB}) (azimuth angle ($\boldsymbol{\theta}$) and hypocenter location are randomized).

	Mean			Footwall			Hanging wall		
dip	c1	c2	c3	c1	c2	c3	c1	c2	c3
10	0.1807	0.4005	0.0385	0.2132	0.3418	0.04356	0.1886	0.3921	0.03496
20	0.346	0.4005	0.03749	0.4249	0.3353	0.04934	0.353	0.3982	0.03056
30	0.4837	0.3958	0.03597	0.6296	0.3264	0.05632	0.4771	0.3994	0.02592
40	0.591	0.3816	0.03438	0.8203	0.3138	0.06418	0.5559	0.3908	0.02145
50	0.6763	0.3507	0.0333	0.9861	0.295	0.07151	0.5961	0.3655	0.01749
60	0.7653	0.2982	0.03472	1.114	0.2704	0.07638	0.6219	0.3137	0.01495
70	0.9143	0.2416	0.04623	1.201	0.2477	0.07897	0.698	0.2435	0.01845
80	1.124	0.213	0.06916	1.251	0.2321	0.08013	0.9934	0.1898	0.05233
90	1.091	0.3018	0.07638						

5.2.2 Epicentral distance and Joyner-Boore distance

The standard deviation for R_{EPI} at a given R_{JB}, M, and δ for dip-slip fault can be determined using the equation:

$$\sigma_{[R_{EPI}|R_{JB},M,\delta]} = C_1 \exp(C_2(M-5)) \left(R_{JB}^{C_3} - C_4\right) + C_5 R_{JB}^{C_6} \tag{5.2}$$

The coefficients C_1 to C_6 are determined using regression and listed in Table 5.2. The coefficients are different for different dip angles. The sigma value increases with increasing magnitude and distance. Though sigma increases with dip angles at a smaller magnitude and R_{JB}, at large magnitudes, there is no significant variation in sigma values for different dip angles.

Table 5.2 Coefficients for calculation of $\boldsymbol{\sigma}_{[\boldsymbol{REPI}|\boldsymbol{RJB},\boldsymbol{M},\boldsymbol{\delta}]}$ at different dip angles for a given Magnitude (M) and Joyner-Boore distance (R_{JB}) (azimuth angle ($\boldsymbol{\theta}$) and hypocenter location are randomized).

δ	C_1	C_2	C_3	C_4	C_5	C_6
10	0.07256	1.71	0.3498	0.5909	0.7239	-0.2208
20	0.07344	1.708	0.3493	0.5906	0.7198	-0.2371
30	0.07504	1.704	0.3483	0.5921	0.7148	-0.2657
40	0.07752	1.697	0.3467	0.5918	0.7103	-0.3078
50	0.08021	1.691	0.3451	0.5899	0.7049	-0.3563
60	0.08405	1.683	0.343	0.5895	0.7101	-0.4151
70	0.09132	1.668	0.3392	0.5999	0.7467	-0.4853
80	0.1031	1.646	0.332	0.6298	0.8473	-0.5442
90	0.1678	1.848	0.1752	0.9409	1.494	-0.4161

5.2.3 Hypocentral distance and Joyner-Boore distance

The standard deviation for R_{HYP} at a given R_{JB}, M, and δ for dip-slip faults can be determined using the equation:

$$\sigma_{[R_{HYP}|R_{JB},M,\delta]} = C_1 \exp(C_2(M-5))\left(R_{JB}^{C_3} - C_4\right) + C_5 R_{JB}^{C_6} + C_7 \exp\left(C_8(M-5)\right) \qquad (5.3)$$

Similarly, for the vertical strike-slip fault ($\delta = 90°$),

$$\sigma_{[R_{HYP}|R_{JB},M,\delta]} = C_1 \exp(C_2(M-5)^2)\left(R_{JB}^{C_3} - C_4\right) + C_5 R_{JB}^{C_6} + C_7 \exp\left(C_8(M-5)\right) \quad (5.4)$$

The coefficients C_1 to C_8 are determined using regression and listed in Table 5.3. The coefficients differ for different dip angles, and the sigma value increases with magnitude, dip angle, and distance. For large magnitudes (M>7.5), there is no considerable variation in sigma values for different dip angles.

Table 5.3 Coefficients for calculation of $\boldsymbol{\sigma_{[RHYP|RJB,M,\delta,Z_{TOR}]}}$ at different dip angles for a given Magnitude (M), depth to the top of the rupture (Z_{TOR}), and Joyner-Boore distance (R_{JB}) (azimuth angle ($\boldsymbol{\theta}$) and hypocenter location are randomized).

δ	C_1	`C_2	C_3	C_4	C_5	C_6	C_7	C_8
10	0.06713	1.735	0.3506	0.5713	0.4025	-0.3045	0	0
20	0.06924	1.737	0.346	0.6179	0.9081	-0.4381	0	0
30	0.07177	1.737	0.3418	0.6587	1.456	-0.4835	0	0
40	0.03256	1.897	0.4069	0.9976	-0.05961	0.7247	0.7838	0.6469
50	0.03361	1.897	0.4038	1.006	-0.2863	0.4537	1.32	0.4966
60	0.03339	1.904	0.4048	1.063	-0.4847	0.3859	1.72	0.4531
70	0.03449	1.898	0.4062	1.133	-0.5475	0.3862	1.903	0.4562
80	0.03582	1.89	0.408	1.242	-0.4631	0.4328	1.848	0.505
90	0.7622	0.3002	0.405	1.168	-0.9389	0.4699	2.303	0.4218

5.3 Residuals

We have also plotted the residuals for the sigma of R_{RUP}, R_{EPI}, and R_{HYP} for M 6 and M 7 at dip angles of 30°, 50°, and 70°, and for the vertical strike-slip fault as shown in Figure 5.1, Figure 5.2, and Figure 5.3 respectively. The residual values are similar to the mean values, with a residual

sigma variation of ±0.4 km for R_{RUP}, ±2 km for $R_{EPI,}$ and ±3 km for R_{HYP}. For all cases, the residual values are closer to 0 at small distances (R_{JB} < 30 km).

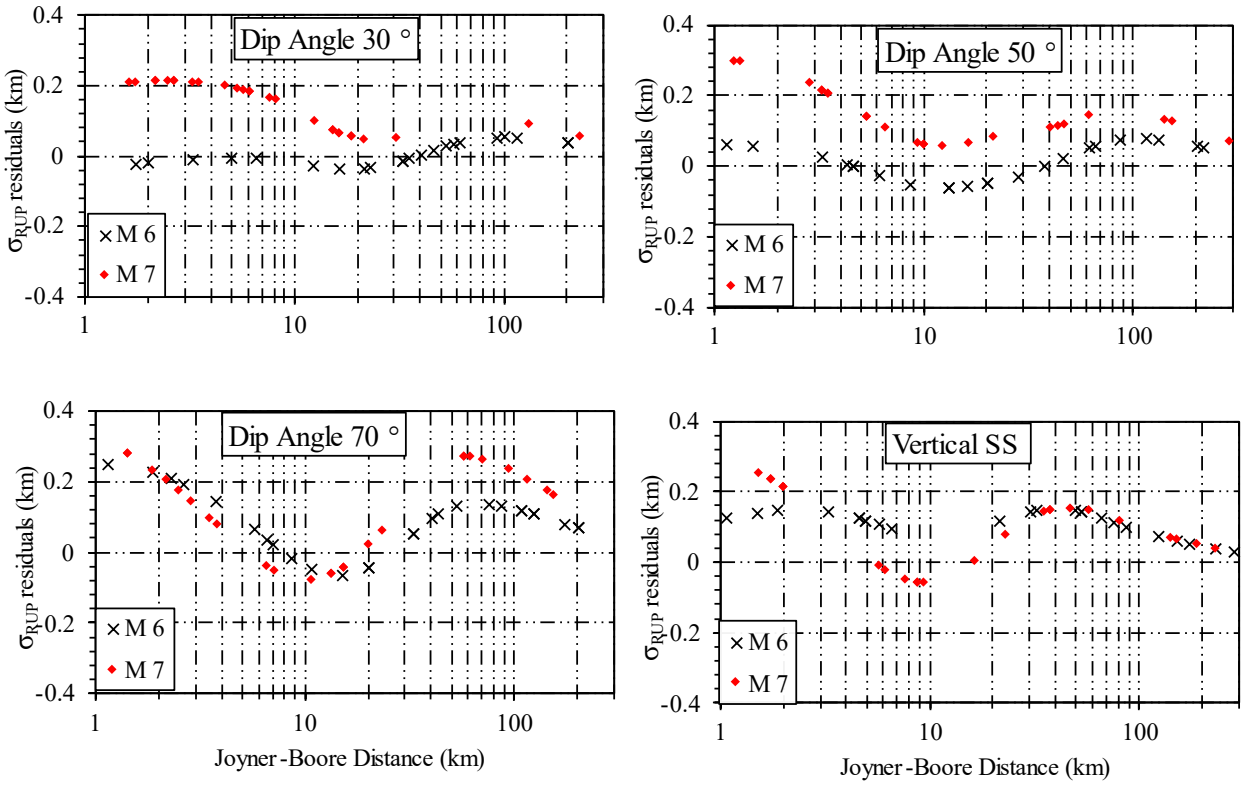

Figure 5.1 Residual values at M 6 and M 7 for sigma of R_{RUP} at dip angles 30°, 50°, 70°, and for vertical strike-slip fault.

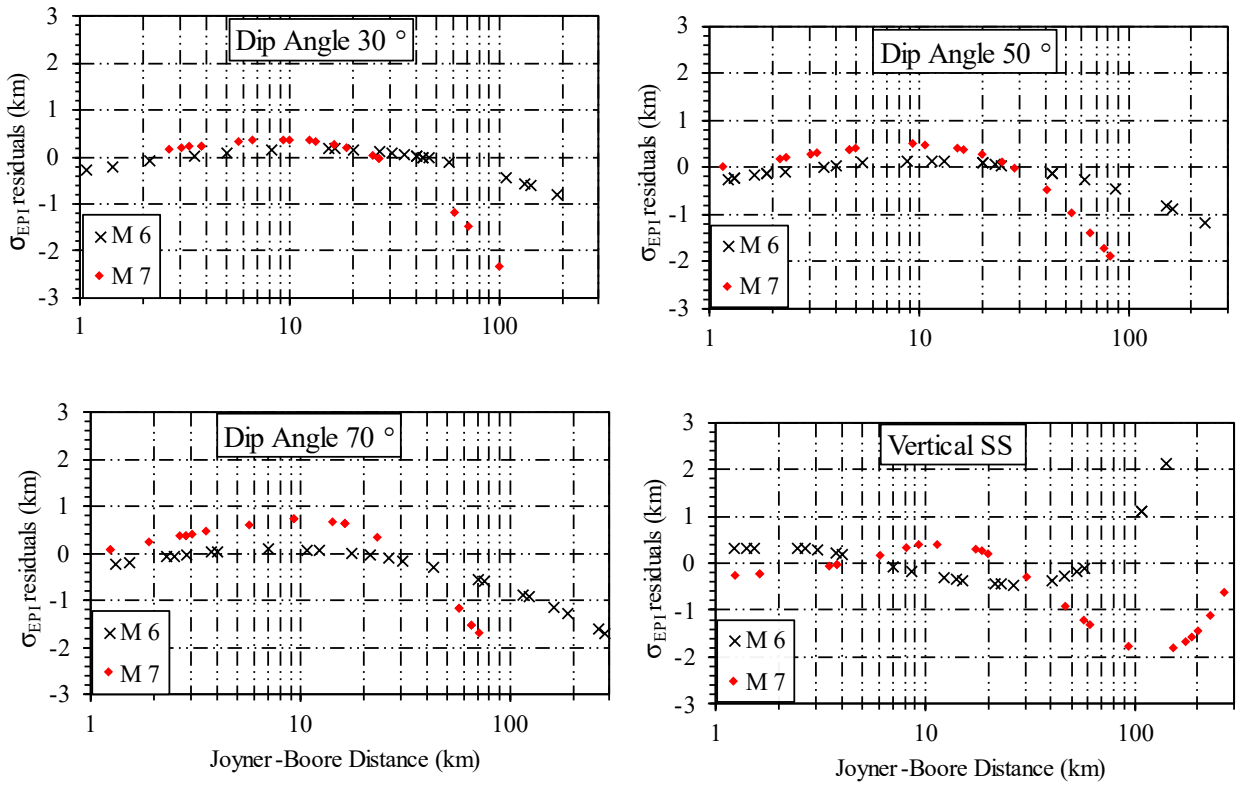

Figure 5.2 Residual values at M 6 and M 7 for sigma of R_{EPI} at dip angles 30°, 50°, 70°, and for vertical strike-slip fault.

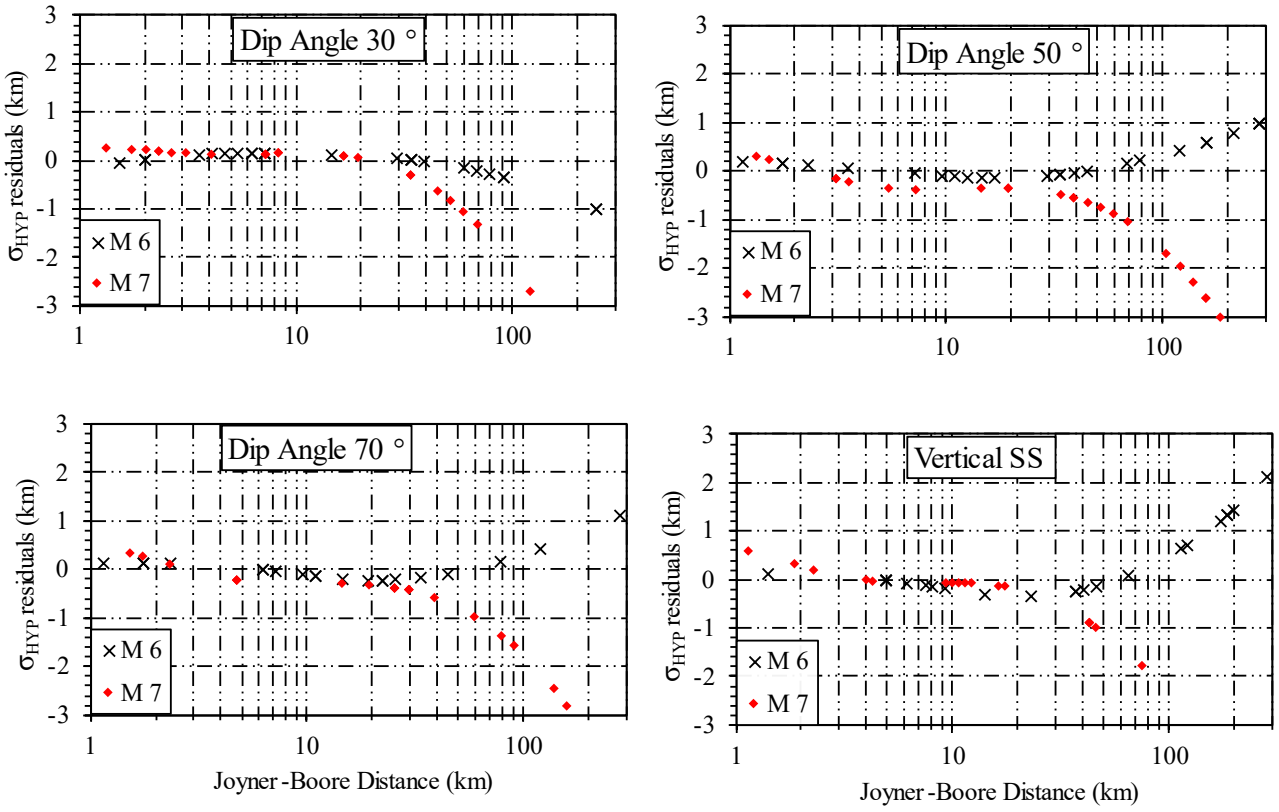

Figure 5.3 Residual values at M 6 and M 7 for sigma of R_{HYP} at dip angles 30°, 50°, 70°, and for vertical strike-slip fault.

5.4 Discussions

The sigma of the proposed model in this study is considerably smaller than Scherbaum et al. (2004), as shown in Figure 5.4 for R_{RUP}, R_{EPI}, and R_{HYP}. The sigma obtained from Scherbaum et al. (2004) for R_{EPI} is much larger for all magnitudes, and similar trends can be observed for R_{HYP}. For R_{RUP}, at smaller distances (<10 km for M 6), the sigma values are slightly higher for this study compared to Scherbaum et al. (2004); however, the difference is negligible (<0.5 km). The sigma has not been compared with EPRI (2004) as it depends on the ground-motion models, so a

comparison would not be valid. Similarly, Thompson and Worden (2018) use R_{EPI} as a reference distance, so a direct comparison of sigma is not possible.

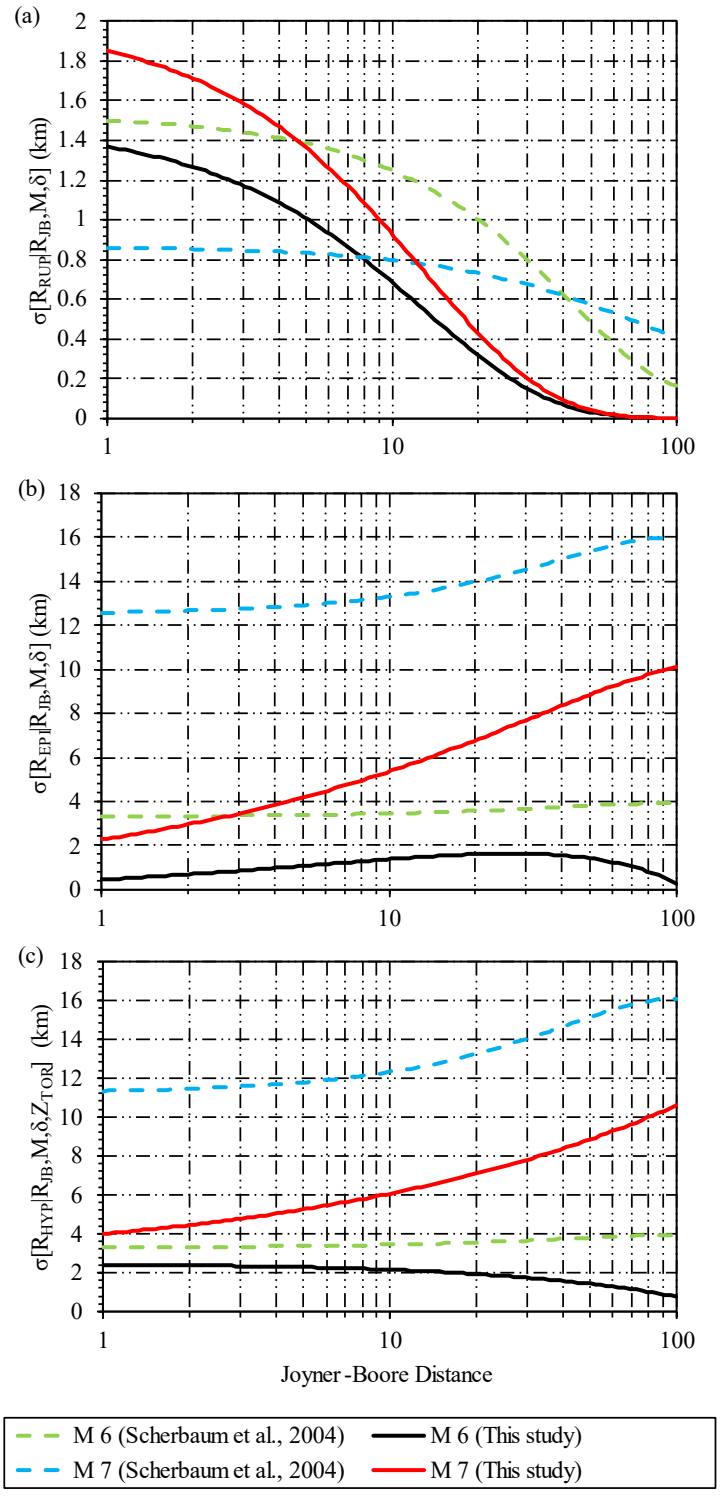

Figure 5.4 Compares the standard deviation for R_{EPI}, R_{HYP}, and R_{RUP} versus R_{JB} obtained from this study and Scherbaum et al. (2004) for Vertical Strike-slip fault for Magnitude 6 and Magnitude 7.

Chapter 6 Applications

6.1 Application in GMMs

In performing PSHA, one must consider whether the source modeling approach is consistent with the distance metric used in the GMMs and can be included in PSHA by calculating an additional variability due to the conversion from R_{JB} to other distance metrics. The total sigma can be calculated using the law of propagation of error as follows:

$$\sigma_{\text{total}} = \sqrt{\sigma_{\text{GMM}}^2 + \Delta\sigma^2}$$
$$\Delta\sigma^2 = \left(\frac{\partial \ln(Y)}{\partial R_{\text{GMM}}}\right)^2 \sigma^2_{[R_{\text{GMM}}|R_{\text{PSHA}}, M, \delta]} \tag{6.1}$$

where σ_{GMM} is the standard deviation for the GMM, $\ln(Y)$ is the natural logarithm of the ground motion and $\sigma_{[R_{\text{GMM}}|R_{\text{PSHA}}, M, \delta]}$ is the standard deviation for the conversion from GMM distances to PSHA distances. The GMMs can be based on R_{JB} or R_{RUP}. If the GMM is based on R_{JB} and the PSHA is based on R_{EPI}, then:

$$\Delta\sigma^2 = \Delta\sigma^2_{[R_{JB}|R_{EPI}, M, \delta]} = \left(\frac{\partial \ln(Y)}{\partial R_{JB}}\right)^2 \sigma^2_{[R_{JB}|R_{EPI}, M, \delta]} \tag{6.2}$$

$$\sigma^2_{[R_{JB}|R_{EPI}, M, \delta]} = \left[\frac{\partial R_{JB}}{\partial R_{EPI}}\right]^2 \sigma^2_{[R_{EPI}|R_{JB}, M, \delta]} \tag{6.3}$$

We can directly calculate the $\frac{\partial R_{JB}}{\partial R_{EPI}} = \frac{1}{(\frac{\partial R_{EPI}}{\partial R_{JB}})}$ (using the empirical equation for $R_{EPI;}$ $\frac{\partial R_{EPI}}{\partial R_{JB}} \neq 0$), or we can use the Taylor series expansion. Using the Taylor series, we can consider only the first-order approximation of the second moment obtained from the Taylor expansion for simplicity. If

there is no empirical relation between the distance metrics, we can use the following approximation:

$$\frac{\partial R_{JB}}{\partial R_{EPI}} = \frac{2\Delta R_{JB}}{< R_{EPI} >_{R_{JB}+\Delta R_{JB}} - < R_{EPI} >_{R_{JB}-\Delta R_{JB}}} \tag{6.4}$$

In which $< R_{EPI} >_{R_{JB}+\Delta R_{JB}}$ is the mean R_{EPI} for a given reference distance of $R_{JB} + \Delta R_{JB}$. Since we have the relation between different distance metrics in our case, we can directly calculate $\frac{\partial R_{JB}}{\partial R_{EPI}}$. $\sigma^2_{[R_{EPI}|R_{JB},M,\delta]}$ can be calculated using equation (5.2) for different magnitudes and dip angles. Similarly, for a GMM based on R_{RUP} and a PSHA based on R_{EPI},

$$\Delta\sigma^2 = \Delta\sigma^2_{[R_{RUP}|R_{EPI},M,\delta]} = \left(\frac{\partial \ln(Y)}{\partial R_{RUP}}\right)^2 \sigma^2_{[R_{RUP}|R_{EPI},M,\delta]} \tag{6.5}$$

We can also calculate similar values for R_{RUP} and R_{HYP} using equation (5.1) and equation (5.3), respectively.

6.2 Application in NSHMP-haz

Powers et al. (2022) developed USGS National Seismic Hazard Mapping Project (NSHMP) codes for performing PSHA for the US and its territories. We modified the NSHMP-haz software to calculate the R_{RUP} using the proposed empirical equations. We conducted a seismic hazard study at four different sites for a vertical strike-slip fault and a dip-slip fault with a dip angle of 50°, as shown in Figure 6.1. For the comparison, we have used Pezeshk et al. (2011) as the GMM, which uses R_{RUP} as the reference distance, to determine the hazard. We assume a fault capable of generating an earthquake of M 7. The rupture dimensions are calculated based on Somerville (2014). The depth to the top of the rupture is calculated using Scherbaum et al. (2004). For M 7,

the Z_{TOR} is 3.54 km for the vertical strike-slip fault and 3.42 km for the dip-slip fault with a 50° dip angle. Assigning different Z_{TOR} values would result in larger differences in the hazard. The activity rate is set to 1 in 500 years. We also calculated the hazard for activity rates of 1 in 1000 years, 1 in 2500 years, and 1 in 10000 years, but the relative differences between the hazard calculated based on original codes and modified codes (which uses the empirical equation for R_{RUP} developed herein) are similar. We found that these equations provided comparable hazard results to those determined using NSHMP-haz for the vertical strike-slip fault as shown in Figure 6.2. The predicted hazard is lower using the proposed empirical equations since it predicted slightly higher values for R_{RUP}. The difference is negligible at R_{RUP} greater than 20 km, as observed by the minimum variation in hazard calculated for Site 4. For the dip-slip fault, the difference is much higher, as shown in Figure 6.3. The hazard may also be higher or lower than those predicted by the NSHMP-haz software, based on the location of the site (hanging wall or footwall).

NSHMP-haz uses different rupture scaling relationships to determine the ruptured dimensions based on magnitude. These scaling relationships, such as "NSHM_SOMERVILLE" have sigma associated with them, so we may obtain a range of ruptured area values (and their respective length and width) for a given magnitude. The empirical equations used here have considered different ruptured area values for a given magnitude, resulting in a wide range of values. Due to this variation, there is a difference in the calculated hazard. Figure 6.4 shows the variation of hazard for distances at one standard deviation above and below the mean for a vertical strike-slip fault for Site 1 and Site 4. This difference is more prominently observed for dip-slip faults, where the width of the fault is also an important parameter, as shown in Figure 6.5 for Site 2 and Site 4.

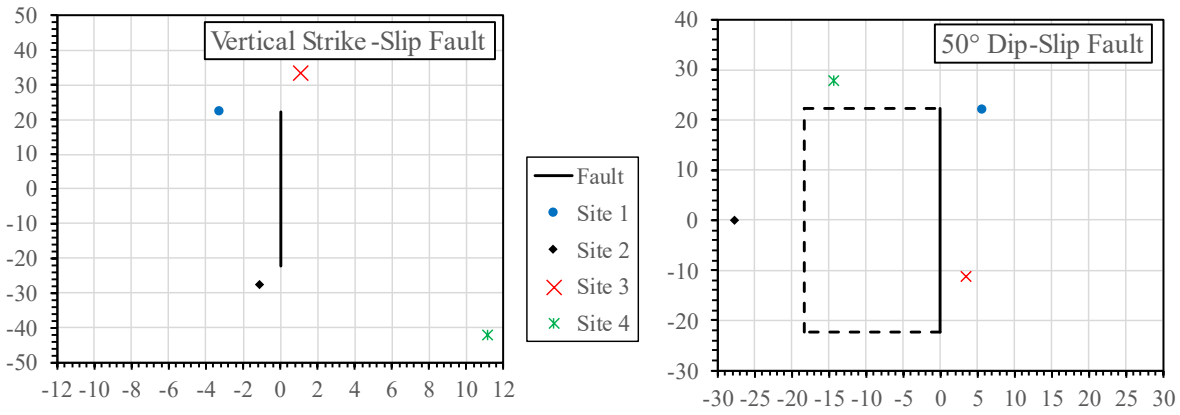

Figure 6.1 Location of the sites about the fault for M 7 earthquake for vertical strike-slip fault (a) and dip-slip fault with 50° dip angle (b). The line represents the fault, and the points represent the location of the sites.

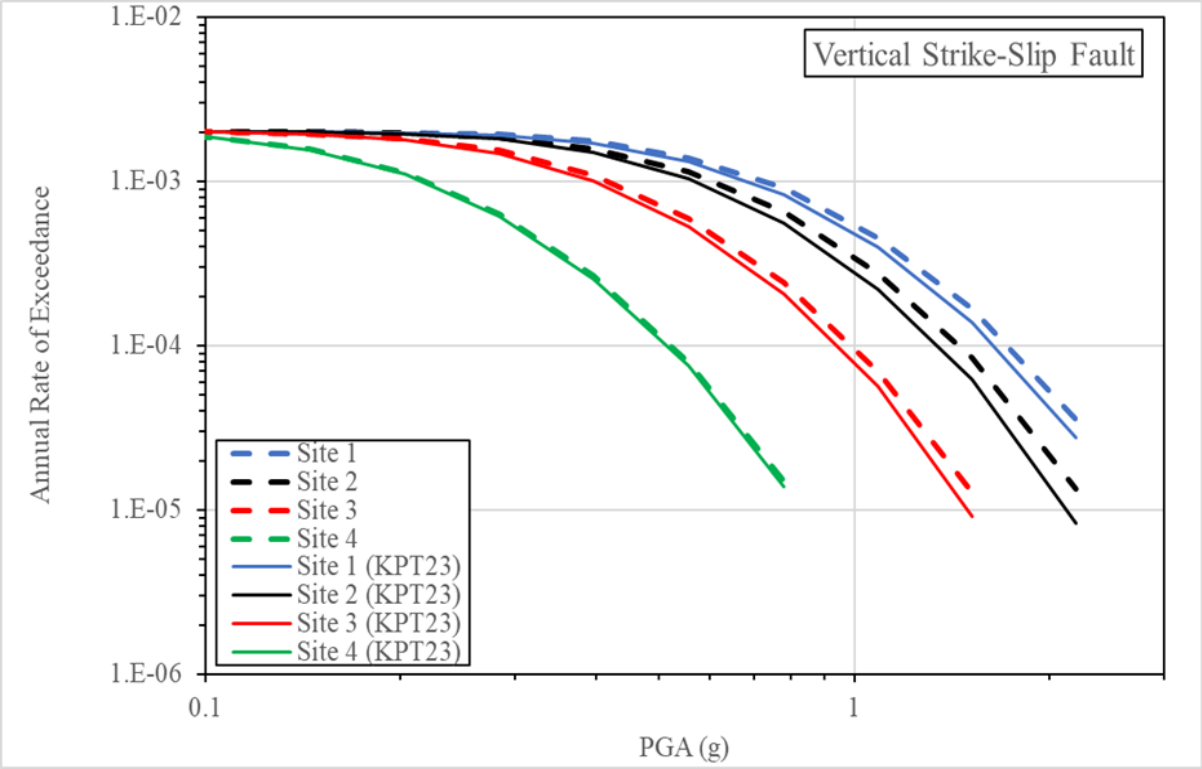

Figure 6.2 Hazard curves at different sites for Peak Ground Acceleration (PGA) and activity rate of 1 in 500 years for a vertical strike-slip fault. The dotted lines represent the values obtained from NSHMP-haz software, and the solid lines represent the values obtained using the empirical equations proposed in this study (KPT23).

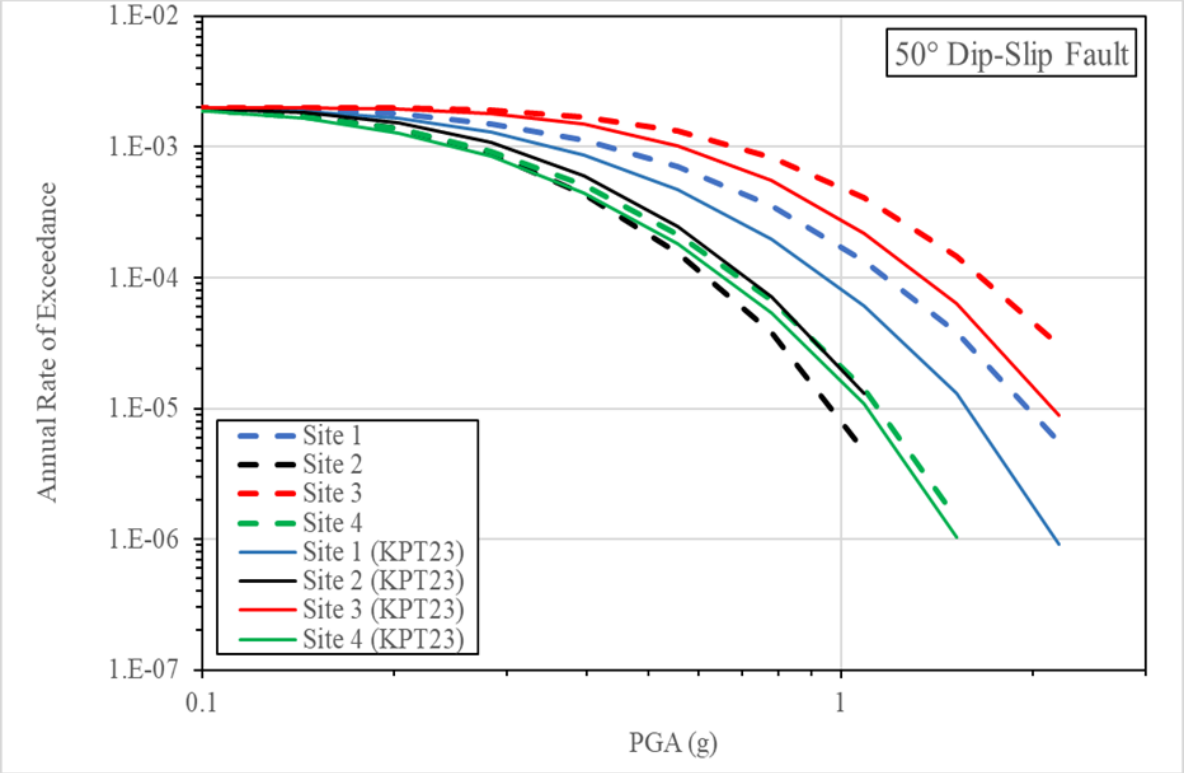

Figure 6.3 Hazard curves at different sites for Peak Ground Acceleration (PGA) and activity rate of 1 in 500 years for dip-slip fault with 50° dip angle. The dotted lines represent the values obtained from NSHMP-haz software, and the solid lines represent the values obtained using the empirical equations proposed in this study (KPT23).

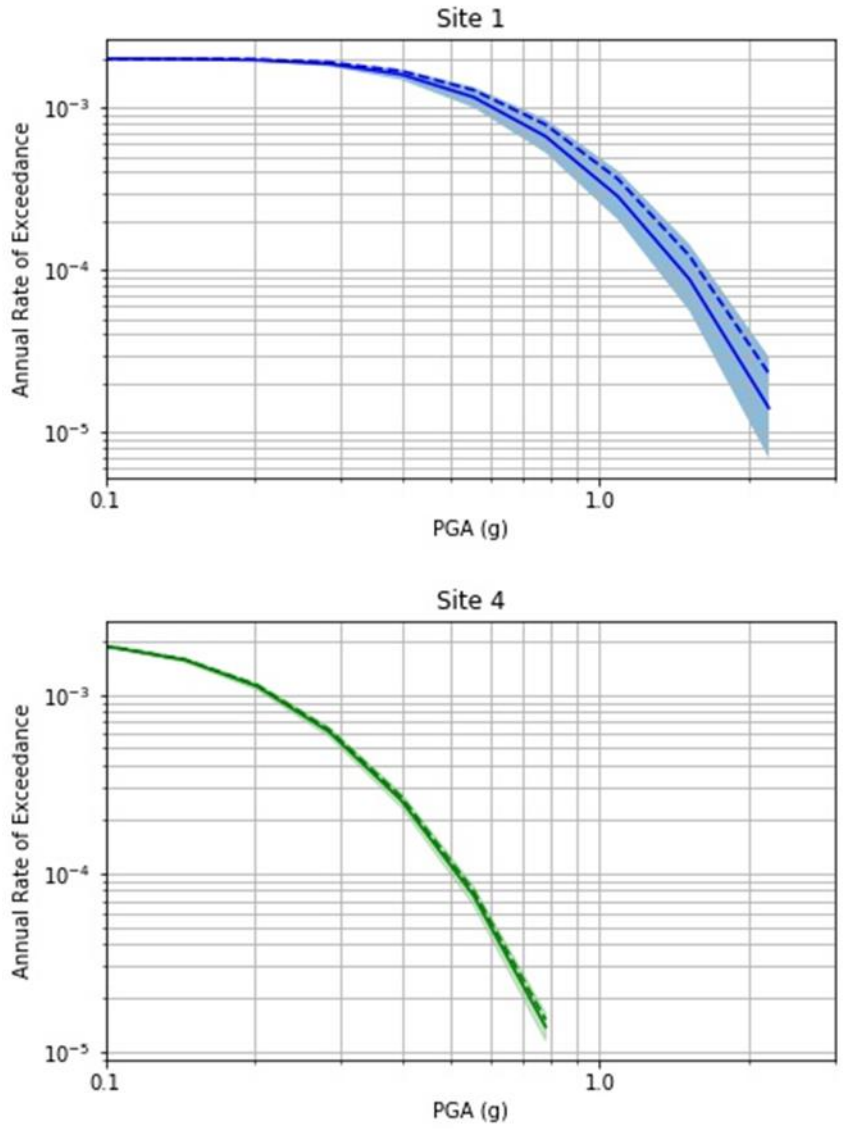

Figure 6.4 Hazard curves at Site 1 (top) and Site 4 (bottom) for Peak Ground Acceleration (PGA) and activity rate of 1 in 500 years for Vertical Strike-Slip fault. The solid line represents the hazard calculated using the mean distance obtained from the proposed empirical equations. The boundary represents the hazard calculated at mean $\pm$ 1 sd distance. The dashed line represents the hazard obtained from NSHMP-haz software.

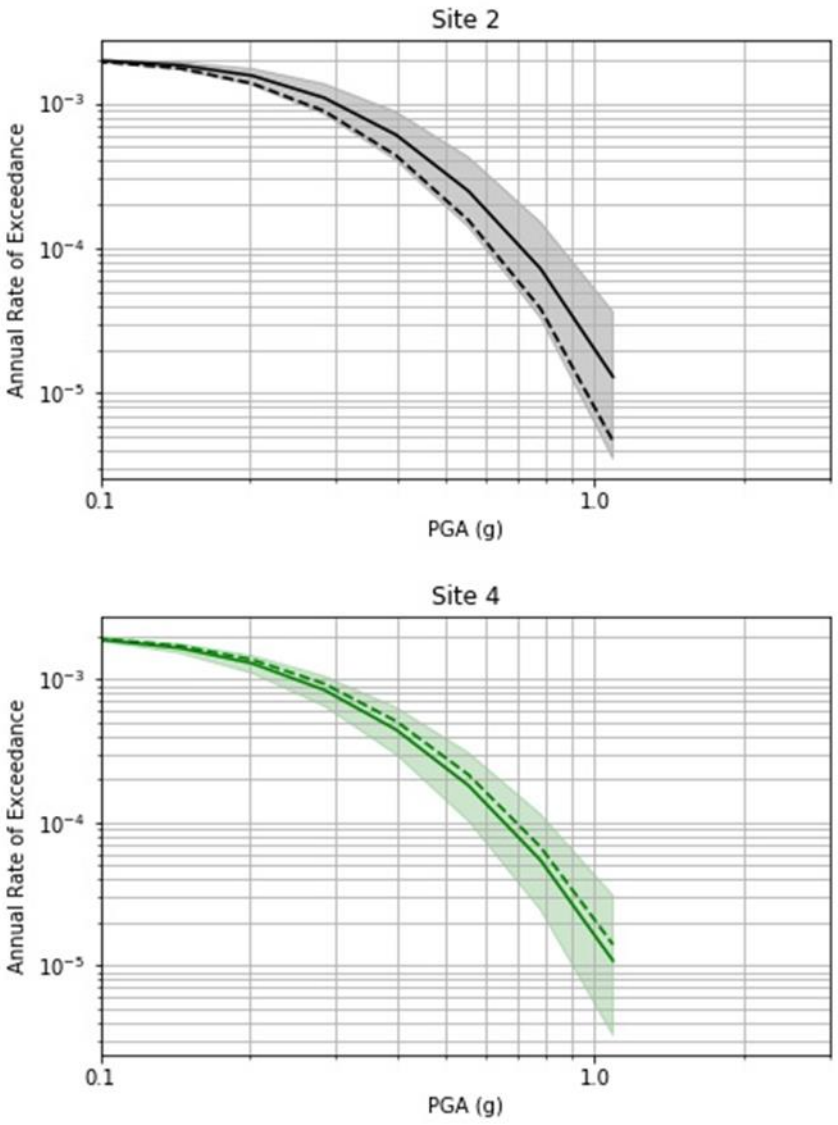

Figure 6.5 Hazard curves at Site 2 (top) and Site 4 (bottom) for Peak Ground Acceleration (PGA) and activity rate of 1 in 500 years for Dip-Slip fault with dip angle 50°. The solid line represents the hazard calculated using the mean distance obtained from the empirical equations. The boundary represents the hazard calculated at mean $\pm$ 1 sd distance. The dashed line represents the hazard obtained from NSHMP-haz software.

6.3 Application in PSHA

In PSHA, the integral over various seismic sources, such as faults and areal sources, is conducted for each site for different magnitudes and distances. Areal sources are assigned when we do not

have enough information about the fault, such as in some regions of CEUS. They are generally used for low and moderate seismicity. The areal source is subdivided into grids where each grid acts as a point source. The distance from each point source to the site can be described using point-based distances such as R_{EPI} or R_{HYP}. Since we do not have enough information about the fault in such cases, it is challenging to use fault-based distances such as R_{JB} and R_{RUP}.

The total variation in the calculated seismic hazard due to the conversion of distance and their associated uncertainties can be demonstrated by considering a simple seismic source. We have considered a circular seismic source with a radius of 100 km. The seismicity of the source follows a truncated exponential model with $\lambda(M \geq 5) = 0.0395$ and a b-value of 0.9. The magnitude is truncated from 5.0 to 7.5. The magnitude and distance are restricted to 7.5 and 100 km, respectively, to adhere to the limitation of Scherbaum et al. (2004). We have used two GMMs to conduct PSHA calculations: Pezeshk et al. (2011) based on R_{RUP} (referred to as PZT11) and Boore et al. (2014) (referred to as BSSA14) based on R_{JB}. The seismic source is divided into grids, each acting like a point source. A site is assumed at the center of the areal seismic source. We calculate the epicentral distance by measuring the distance from each point source to the site. However, the GMM is based on R_{RUP} or R_{JB}. Hence, we need to convert the distances for consistency between the PSHA and GMM.

At a sample R_{EPI} of 30 km for a vertical strike-slip fault of magnitude 7.0, we obtain a R_{JB} of 21.1 km and a R_{RUP} of 23.4 km. So, for a 30 km R_{EPI} used in the PSHA for an areal source, we need to use a R_{RUP} of 23.4 km in PZT11 and 21.1 km in BSSA14 for consistency. Since the equivalent R_{RUP} and R_{JB} are smaller than the R_{EPI} in this example, it increases the calculated seismic hazard. In this example, there is no direct way to convert from R_{EPI} to R_{JB} since the equations developed

in this study are based on R_{JB}. So, we determine R_{EPI} values for different R_{JB} values for a given magnitude using equations (4.4, 4.5) and populate a table. We can use this table to determine R_{JB} values for the required R_{EPI} values, which can be used in BSSA14. We can use the calculated R_{JB} values to determine R_{RUP} for a given magnitude and dip angle using equations (4.2, 4.3) in PZT11.

The additional sigma due to distance conversion must also be included in the PSHA to obtain accurate seismic hazard results. The equation for the derivative of the GMM, which is necessary to determine the total sigma, is discussed in the appendix. Based on the mean and the total sigma, we determine the mean exceedance at different magnitudes and distances to calculate the seismic hazard. Figure 6.6 shows the mean annual exceedance of hazard based on PZT11 and BSSA14. The solid red lines represent the hazard without any distance conversion. The black dashed lines represent the hazard calculated based on the proposed empirical equations (referred to as KPT23). We have also included comparisons for Thompson and Worden (2018) (referred to as TW18) and Scherbaum et al. (2004) (referred to as SSC04). For PZT11, based on R_{RUP}, we can observe a significant increase in the calculated mean annual frequency of exceedance as the spectral acceleration (SA) increases. The increase in the values is smaller for KPT23 compared to TW18 and SSC04. For a SA value of 2.0 g, the hazard increases by a factor of 1.4 for KPT23, 9.2 for SSC04, and 44 for TW18. The values for TW18 appear to saturate as the spectral values increase. The mean values for the distance conversions for different studies, as discussed in section 4.4, do not vary significantly. However, there is significant variation in sigma values for the different studies. The sigma value for R_{RUP} decreases as the distance increases for SSC04 and KPT23. However, the sigma value for R_{RUP} increases with the distance for TW18. SSC04 also has a higher

sigma variation compared to KPT23. As a result, other published studies report higher values for the same SA values.

Similarly, we can observe an increase in the mean annual exceedance rate for BSSA14, based on R_{JB}, for the distance conversion equations provided in all the published studies. Unlike the variation observed for PZT11, the hazard values are similar for KPT23 and TW18. SSC04 has higher values compared to others. For a SA value of 2.0 g, the hazard increases by a factor of 1.9 for KPT23, 2.1 for TW18, and 3.3 for SSC04. Hence, one must convert to appropriate distances and project their uncertainties in the PSHA calculations to obtain accurate seismic hazards.

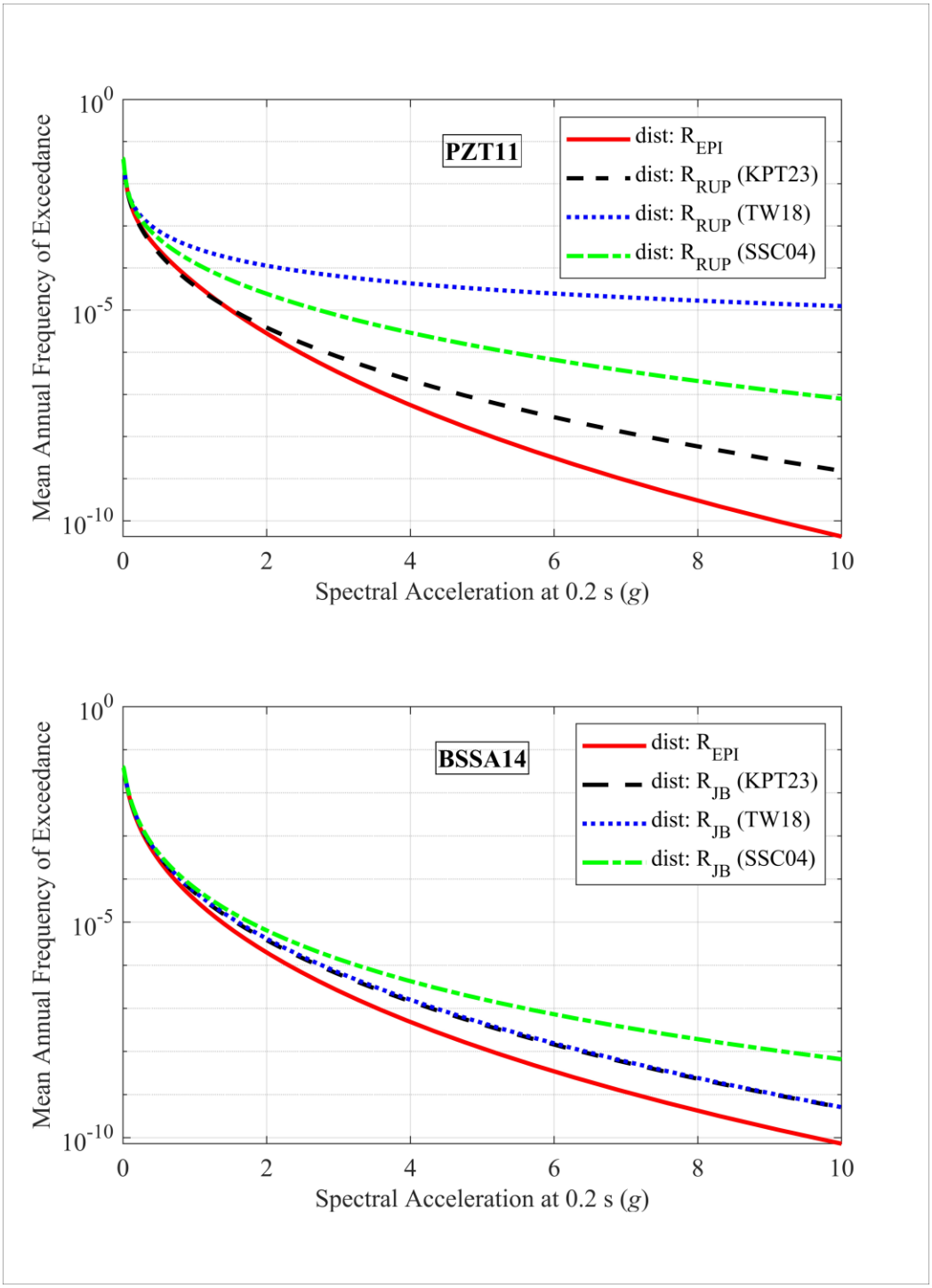

Figure 6.6 Annual hazard curves for a circular seismic source with a radius of 100 km based on R_{RUP}-based GMM (Pezeshk et al., 2011) (top) and R_{JB}-based GMM (Boore et al., 2014) (bottom) using distance conversion equations developed in this study (KPT23). Annual hazard curves without distance conversion and those based on Thomson and Worden (2018) (TW18) and Scherbaum et al. (2004) (SSC04) are also shown for reference.

Chapter 7 Conclusion, Contributions, and Future Work

7.1 Conclusion and Contributions

This study provides empirical relations among different distance metrics. The equations were developed with an emphasis on stable continental regions. As a result, we have used Somerville (2014) to describe the relationship between the rupture area and the magnitude of the earthquake. We have demonstrated that R_{JB} can be effectively used to determine other source-to-site distance metrics based on the properties of the fault. We determined the differences between the various distance metrics and R_{JB}. These differences can be described using a gamma distribution. The functional forms for R_{target} are based on the magnitude and the dip angle of the fault (also Z_{TOR} for R_{HYP}) for a random azimuth and hypocenter location. Since the empirical equations provide a mean estimate of the required distance measure for a given magnitude and the dip angle of the fault, these equations may not be effective when the location of the hypocenter or the azimuth of the fault is known. A method to determine the sigma of the obtained results has also been discussed. These equations are helpful in PSHA to reliably convert from R_{JB} to other rupture-based distances (R_{RUP}) and point-based distances (R_{EPI} and R_{HYP}). The equations for variability can be used to obtain the total sigma for use in PSHA. To use these equations, we only need basic information on the type of faulting, applicable source-scaling equations, and the dip angle of the fault based on available geologic and tectonic information. If the dip angle is unknown, we can assume a dip angle of 40° (Kaklamanos et al. 2011) and apply appropriate sigma values.

Though these distance metrics are closer to each other at large distances, there are significant differences between them at smaller distances. Ignoring these differences will result in inaccurate seismic hazard calculations closer to the fault. With interest high in developing accurate ground-

motion models (GMMs) for near-fault areas, we should also consider the effect of different distance metrics in PSHA to obtain accurate seismic hazards of the area. Unlike previous models developed by EPRI (2004) and Scherbaum et al. (2004), which are only dependent on magnitude, the proposed models also depend on the effect of the dip angle for estimating different distance measures. The Scherbaum et al. (2004) model is also highly unstable for larger magnitudes (greater than 7.5) and distances greater than 100 km. We also consider the effect of hanging wall and footwall for the conversion of R_{RUP}. The empirical equations developed in this study are purely based on the geometry of the fault and are not dependent on the GMMs. Hence, the equations can be applied directly in seismic hazard applications for any preferred GMMs, which avoids complex integrations involved in (Thompson and Worden, 2018) and (Tavakoli et al., 2018). We can better estimate the seismic hazard for the region of interest by using the distance conversion equations and their respective uncertainties.

7.2 Future Work

The researcher is interested in pursuing this research or recommends extending this research in the following directions:

- The current empirical models apply to GMMs that are based on only one distance metric. However, there are currently many GMMs that may be based on multiple distance metrics. An appropriate method should be developed to include uncertainty due to using multiple distance metrics in a single GMM for use in PSHA.
- The proposed empirical models cannot be used for faults with a particular azimuth. As discussed in section 3.4.2, variation in the azimuth angle can significantly impact the required distance adjustment. For cases when the exact azimuth angle is known, this

approach may not provide an accurate result for estimating the seismic hazard.

Bibliography

Abrahamson, N.A., and W.J. Silva. 2008. “Summary of the Abrahamson & Silva NGA Ground-Motion Relations.” *Earthquake Spectra* 24: 67–97.

Akkar, S., M. A. Sandıkkaya, and J. J. Bommer. 2014. “Empirical Ground-Motion Models for Point- and Extended-Source Crustal Earthquake Scenarios in Europe and the Middle East.” *Bulletin of Earthquake Engineering* 12 (1): 359–87. https://doi.org/10.1007/s10518-013-9461-4.

Atkinson, Gail M., and Walter Silva. 2000. “Stochastic Modeling of California Ground Motions.” *Bulletin of the Seismological Society of America* 90 (2): 255–74. https://doi.org/10.1785/0119990064.

Bommer, Julian J., and Sinan Akkar. 2012. “Consistent Source-to-Site Distance Metrics in Ground-Motion Prediction Equations and Seismic Source Models for PSHA.” *Earthquake Spectra* 28 (1): 1–15. https://doi.org/10.1193/1.3672994.

Bommer, Julian J., Bernard Dost, Benjamin Edwards, Peter J. Stafford, Jan van Elk, Dirk Doornhof, and Michail Ntinalexis. 2016. “Developing an Application-Specific Ground-Motion Model for Induced Seismicity.” *Bulletin of the Seismological Society of America* 106 (1): 158–73. https://doi.org/10.1785/0120150184.

Boore, David M. 2009. “Comparing Stochastic Point-Source and Finite-Source Ground-Motion Simulations: SMSIM and EXSIM.” *Bulletin of the Seismological Society of America* 99 (6): 3202–16. https://doi.org/10.1785/0120090056.

Boore, David M., Jonathan P. Stewart, Emel Seyhan, and Gail M. Atkinson. 2014. “NGA-West2 Equations for Predicting PGA, PGV, and 5% Damped PSA for Shallow Crustal Earthquakes.” *Earthquake Spectra* 30 (3): 1057–85. https://doi.org/10.1193/070113EQS184M.

Bray, Jonathan D, and Adrian Rodriguez-marek. 2004. “Characterization of Forward-Directivity Ground Motions in the near-Fault Region.” *Soil Dynamics and Earthquake Engineering* 24: 815–28. https://doi.org/10.1016/j.soildyn.2004.05.001.

Campbell, K. W., and Y. Bozorgnia. 2014. “Campbell-Bozorgnia NGA-West2 Horizontal Ground Motion Model for Active Tectonic Domains.” *NCEE 2014 - 10th U.S. National Conference on Earthquake Engineering: Frontiers of Earthquake Engineering*, no. January. https://doi.org/10.4231/D3MS3K235.

Campbell, Kenneth W., and Nitin Gupta. 2018. “Modeling Diffuse Seismicity in Probabilistic Seismic Hazard Analysis: Treatment of Virtual Faults.” *Earthquake Spectra* 34 (3): 1135–54. https://doi.org/10.1193/041117EQS070M.

Chiou, Brian S.J., and R.R. Youngs. 2008. “An NGA Model for the Average Horizontal Component of Peak Ground Motion and Response Spectra.” *Earthquake Spectra* 24: 173–215.

Cornell, C. A. 1968. “Engineering Seismic Risk Analysis.” *Bulletin of the Seismological Society*

of America 58 (5): 1589–1606.

Cornell, C., and H. Krawinkler. 2000. “Progress and Challenges in Seismic Performance Assessment.” *PEER Center News 3*.

Deierlein, G. 2004. “Overview of a Comprehensive Framework for Earthquake Performance Assessment.” *International Workshop on Performance-Based Seismic Design Concepts and Implementation* Bled,Slove: 15–26.

EPRI. 2004. “CEUS Ground Motion Project Final Report, EPRI Report.” *EPRI Report 1009684*, no. December.

Hanks, T. C.;, and W. H Bakun. 2008. “M-Log A Observations for Recent Large Earthquakes.” *Bulletin of the Seismological Society of America* 98: 490–494.

Kaklamanos, James, Laurie G. Baise, and David M. Boore. 2011. “Estimating Unknown Input Parameters When Implementing the NGA Ground-Motion Prediction Equations in Engineering Practice.” *Earthquake Spectra* 27 (4): 1219–35. https://doi.org/10.1193/1.3650372.

Kayastha, Melish, Shahram Pezeshk, and Behrooz Tavakoli. 2021. “Empirical Relationship between Different Source-to-Site Distances.” *93rd Annual Meeting of the Eastern Society of the Seismological Society of America*. https://doi.org/10.13140/RG.2.2.29811.71205.

Kayastha, Melish, Shahram Pezeshk, and Behrooz Tavakoli. 2022a. “Developing an Empirical Relationship between Different Distances Metrics for Seismic Hazard Assessment.” *Annual Meeting of the Seismological Society of America*. https://doi.org/10.13140/RG.2.2.26456.26889.

Kayastha, Melish, Shahram Pezeshk, and Behrooz Tavakoli. 2022b. “Effect of Sigma Variability Due to Distance Conversion in PSHA.” *94th Annual Meeting of the Eastern Society of the Seismological Society of America*. https://doi.org/10.13140/RG.2.2.36522.59842.

Kayastha, Melish, Shahram Pezeshk, and Behrooz Tavakoli. 2023a. “Implementation of Distance Conversion Equations in Seismic Hazard.” *SSA Annual Meeting*. https://doi.org/10.13140/RG.2.2.20066.20163.

Kayastha, Melish, Shahram Pezeshk, and Behrooz Tavakoli. 2023b. “Empirical Distance Metrics Relationships and Uncertainties in Seismic Hazard Assessment.” *Bulletin of the Seismological Society of America*, March. https://doi.org/10.1785/0120220193.

Kramer, S. L. 1996. “Geotechnical Earthquake Engineering.” *Upper Saddle River, N.J.: Prentice Hall*.

Mai, P. Martin, P. Spudich, and J. Boatwright. 2005. “Hypocenter Locations in Finite-Source Rupture Models.” *Bulletin of the Seismological Society of America* 95 (3): 965–80. https://doi.org/10.1785/0120040111.

McGuire, R. K. 2004. “Seismic Hazard and Risk Analysis.” *Berkeley: Earthquake Engineering Research Institute*.

Monelli, D., M. Pagani, G. Weatherill, L. Danciu, and J. Garcia. 2014. “Modeling Distributed Seismicity for Probabilistic Seismic-Hazard Analysis: Implementation and Insights with the OpenQuake Engine.” *Bulletin of the Seismological Society of America* 104: 1636–49.

Petersen, Mark D., Arthur D. Frankel, Stephen C. Harmsen, Charles S. Mueller, Kathleen M. Haller, Russell L. Wheeler, Robert L. Wesson, et al. 2010. “Documentation for the 2008 Update of the United States National Seismic Hazard Maps.” *Earthquake Research: Background and Select Reports*, 107–234.

Pezeshk, Shahram, Arash Zandieh, and Behrooz Tavakoli. 2011. “Hybrid Empirical Ground-Motion Prediction Equations for Eastern North America Using NGA Models and Updated Seismological Parameters.” *Bulletin of the Seismological Society of America* 101 (4): 1859–70. https://doi.org/10.1785/0120100144.

Powers, P.M., B.S. Clayton, and J.M. Altekruse. 2022. “Nshmp-Haz: National Seismic Hazard Model Project Hazard Applications and Web Services.” U.S. Geological Survey software release. https://doi.org/10.5066/P9STF5GK.

Scherbaum, Frank, Jan Schmedes, and Fabrice Cotton. 2004. “On the Conversion of Source-to-Site Distance Measures for Extended Earthquake Source Models.” *Bulletin of the Seismological Society of America* 94 (3): 1053–69. https://doi.org/10.1785/0120030055.

Shahi, Shrey Kumar, and Jack Baker. 2013. “A Probabalistic Framework to Include the Effects of Near-Fault Directivity in Seismic Hazard Assessment And,” no. October: 1–247.

Shaw, B. E., and S. G.Wesnousky. 2008. “Slip-Length Scaling in Large Earthquakes: The Role of Deep-Penetrating Slip below the Seismogenic Layer.” *Bulletin of the Seismological Society of America* 98 (4): 1633–1641.

Silva, W. J., N. Gregor, and R. Darragh. 2002. “Development of Regional Hard Rock Attenuation Relations for Central and Eastern North America.” *Pacific Engineering and Analysis, El Cerrito, CA*.

Somerville, P. G., N. Collins, N. A. Abrahamson, R. Graves, and C. K. Saikia. 2001. “Ground Motion Attenuation Relations for the Central and Eastern United States.” *Report to U.S. Geological Survey, NEHRP External Research Program, Award No. 99-HQ-GR-0098*.

Somerville, Paul. 2014. “Scaling Relations between Seismic Moment and Rupture Area of Earthquakes in Stable Continental Regions.” *PEER Report*, no. August. https://doi.org/10.1177/8755293020988024.

Somerville, Paul G., Nancy F. Smith, Robert W. Graves, and Norman A. Abrahamson. 1997. “Modification of Empirical Strong Ground Motion Attenuation Relations to Include the Amplitude and Duration Effects of Rupture Directivity.” *Seismological Research Letters* 68 (1): 199–222. https://doi.org/10.1785/gssrl.68.1.199.

Spudich, P., J.R. Bayless, J. Baker, Brian S J Chiou, B. Rowshandel, S. Shahi, and Paul Somerville. 2013. “Final Report of the NGA-West2 Directivity Working Group.” *Pacific Engineering Research Center Report*, no. May 2013: 162.

Tarbali, Karim, Brendon A. Bradley, and Jack W. Baker. 2019. “Ground Motion Selection in the Near-Fault Region Considering Directivity-Induced Pulse Effects.” *Earthquake Spectra* 35 (2): 759–86. https://doi.org/10.1193/102517EQS223M.

Tavakoli, Behrooz, Farhad Sedaghati, and Shahram Pezeshk. 2018. “An Analytical Effective Point-Source-Based Distance-Conversion Approach to Mimic the Effects of Extended Faults on Seismic Hazard Assessment.” *Bulletin of the Seismological Society of America* 108 (2): 742–60. https://doi.org/10.1785/0120170171.

Thompson, Eric M., and C. Bruce Worden. 2018. “Estimating Rupture Distances without a Rupture.” *Bulletin of the Seismological Society of America* 108 (1): 371–79. https://doi.org/10.1785/0120170174.

Toro, G. R., N. A. Abrahamson, and J. F. Schneider. 1997. “Model of Strong Ground Motions from Earthquakes in Central and Eastern North America: Best Estimated and Uncertainties.” *Seismological Research Letters* 68: 41–57.

Watson-lamprey, Jennie A. 2018. “PACIFIC EARTHQUAKE ENGINEERING Capturing Directivity Effects in the Mean and Aleatory Variability of the NGA-West2 Ground-Motion Prediction Equations.”

Wells, D. L., and K. J. Coppersmith. 1994. “New Empirical Relationships among Magnitude, Rupture Length, Rupture Width, Rupture Area, and Surface Displacement.” *Bulletin - Seismological Society of America* 84 (4): 974–1002.

Appendix: Calculation of derivative for the GMMs

The equation for Pezeshk et al. (2011) is

$$\begin{aligned}\log(Y) = {} & C_1 + C_2 M_w + C_3 M_w^2 + (C_4 + C_5 M_W)\min(\log(R), \log(70)) \\ & + (C_6 + C_7 M_w)\max\left(\min\left(\log\left(\frac{R}{70}\right), \log\left(\frac{140}{70}\right)\right), 0\right) \\ & + (C_8 + C_9 M_w)\max\left(\log\left(\frac{R}{140}\right), 0\right) + C_{10} R \end{aligned} \tag{A.1}$$

$$R = \sqrt{R_{RUP}^2 + C_{11}^2}$$

The derivative can be calculated as follows:

$$\begin{aligned}\frac{d\log(y)}{dR_{RUP}} = {} & (C_4 + C_5 M_w)\text{min1} + (C_6 + C_7 M_w)\text{maxmin2} + (C_8 + C_9 M_w)\text{max3} \\ & + C_{10}\frac{R_{RUP}}{R}\end{aligned} \tag{A.2}$$

$$\text{min1} = \begin{cases} \dfrac{R_{RUP}}{\ln(10)\, R} & R \le 70 \\ 0 & R \ge 70 \end{cases}$$

$$\text{maxmin2} = \begin{cases} 0 & R \le 70 \\ \dfrac{R_{RUP}}{\ln(10)\, R} & 70 \le R \le 140 \\ 0 & R \ge 140 \end{cases} \tag{A.3}$$

$$\text{max3} = \begin{cases} 0 & R \le 140 \\ \dfrac{R_{RUP}}{\ln(10)\, R} & R \ge 140 \end{cases}$$

The coefficients are provided in Pezeshk et al. (2011).

The derivative for Boore et al. (2014) can be calculated as:

$$\frac{\partial(\ln Y)}{\partial R_{JB}} = \frac{\partial F_p}{\partial R_{JB}}\left(1 + \frac{f_2 PGA_r}{f_3 + PGA_r}\right)$$

$$\frac{\partial F_p}{\partial R_{JB}} = R_{JB}\left(\frac{1}{R^2}[c_1 + c_2(M - M_{ref})] + \frac{1}{R}[c_3 + \Delta c_3]\right) \quad \text{(A.4)}$$

F_P (the path function), R (a function of R_{JB}), and f_2 are defined in Boore et al. (2014). PGA_r is the peak ground acceleration for a reference rock at a shear wave velocity of 760 m/s. c_1, c_2, c_3, Δc_3, and f_3 are constants.